

1. Report No. FHWA/TX-07/0-4509-1		2. Government Accession No.		3. Recipient's Catalog No.	
4. Title and Subtitle EVALUATING INNOVATIVE SENSORS AND TECHNIQUES FOR MEASURING TRAFFIC LOADS: FINAL REPORT				5. Report Date October 2005 Published: October 2006	
				6. Performing Organization Code	
7. Author(s) Richard Liu, Xuemin Chen, Jing Li, Lianhe Guo, and Jingyan Yu				8. Performing Organization Report No. Report 0-4509-1	
9. Performing Organization Name and Address Department of Electrical and Computer Engineering University of Houston 4800 Calhoun Rd. Houston, TX 77204-4005				10. Work Unit No.	
				11. Contract or Grant No. Project 0-4509	
12. Sponsoring Agency Name and Address Research and Technology Implementation Office Texas Department of Transportation P. O. Box 5080 Austin, TX 78763-5080				13. Type of Report and Period Covered Technical Report: September 2003 – August 2005	
				14. Sponsoring Agency Code	
15. Supplementary Notes Project performed in cooperation with the Texas Department of Transportation and the Federal Highway Administration. Project title: Evaluating Innovative Sensors and Techniques for Measuring Traffic Loads URL: http://subsurface.ee.uh.edu/documents/0-4509-1.pdf					
16. Abstract: To evaluate weigh-in-motion (WIM) sensors and techniques for measuring traffic loads, a WIM system standard is introduced. Available WIM sensors in the market such as load cell, bending plate, and piezoelectric sensor, etc. are reviewed. Then a remote WIM system is designed and installed to conduct the evaluation of sensors. The designed system can be accessed remotely and is capable of conducting data acquisition for multiple sensors. With the acquired field data, a pavement deflection load determination algorithm is developed, and the results are compared with the integration algorithm. The analysis shows that pavement deflection can be used for a vehicle's weight measurement. Furthermore, the result is helpful for the nondestructive WIM system design. The Fiber Bragg Grating (FBG) sensor is also evaluated in this research. Compared to piezoelectric sensors, FBG sensors offer a simpler and more explicit load determination algorithm, and the life span of the sensors is longer. However, it is necessary to build a sensor holder for the FBG sensor. In addition to the evaluation of regular WIM sensors, an innovative WIM sensor was developed in this project. It is an active sensor based on the perturbation theory of microwave resonant cavity. The microwave signal generated by a circuit is coupled into the sensor, and the returned signal is measured to determine the load applied to the sensor. The lab test results show the microwave WIM sensor can weigh the load to very high accuracy.					
17. Key Words Weigh-in-Motion, WIM Sensor, Piezoelectric Sensor, Fiber Optic Sensor, Fiber Bragg Grating (FBG) Sensor, Microwave WIM Sensor			18. Distribution Statement No restrictions. This document is available to the public through NTIS: National Technical Information Service Springfield, VA 22161 http://www.ntis.gov		
19. Security Classif. (of this report) Unclassified		20. Security Classif. (of this page) Unclassified		21. No. of Pages 158	22. Price

**Evaluating Innovative Sensors and Techniques for
Measuring Traffic Loads**

by

Richard Liu, Xuemin Chen, Jing Li, Lianhe Guo, and Jingyan Yu

Report 0-4509-1

Project Number: 0-4509

Project title: Evaluating Innovative Sensors and Techniques for Measuring Traffic Loads

Performed in Cooperation with the
Texas Department of Transportation
and the
Federal Highway Administration

by the

Subsurface Sensing Laboratory
Department of Electrical and Computer Engineering
University of Houston

October 2005

Published: October 2006

DISCLAIMER

The contents of this report reflect the views of the authors who are responsible for the facts and accuracy of the data presented herein. The contents do not necessarily reflect the official views or policies of the Texas Department of Transportation or the Federal Highway Administration. This report does not constitute a standard, specification, or regulation.

University of Houston
4800 Calhoun Rd.
Houston, TX 77204

ACKNOWLEDGMENTS

We greatly appreciate the financial support from the Texas Department of Transportation that made this project possible. The support of the project director, Joe Leidy; program coordinator, Ed Oshinski; and project manager, Brian Michalk is also very much appreciated. We also thank the Project Monitoring Committee member Dr. German Claros.

TABLE OF CONTENTS

CHAPTER 1: INTRODUCTION.....	1
1.1 Background.....	1
1.2 WIM System Classification.....	4
CHAPTER 2: WIM SYSTEM STANDARD AND WIM SENSORS	5
2.1 WIM System Accuracy.....	5
2.2 ASTM WIM System Classification.....	7
2.3 WIM System Performance Requirements	8
2.4 Sources of Error	9
2.4.1 Vehicle Dynamics.....	10
2.5 Considerations for Selecting an Installation Site.....	12
2.6 WIM Sensors	13
2.6.1 Bending Plate.....	14
2.6.2 Load Cell.....	15
2.6.3 Piezoelectric Sensor.....	16
2.6.4 Capacitance Mat.....	19
2.6.5 Fiber Optic Sensor	20
2.6.6 Microwave WIM Sensor.....	23
2.6.7 Commercial WIM Sensors Comparison	26
CHAPTER 3: REMOTE WIM SYSTEM DESIGN AND INSTALLATION	29
3.1 Test Site Description.....	29
3.2 Remote WIM System Design	31
3.2.1 Hardware Configuration	32
3.2.2 Software Configuration.....	34
3.3 Sensor Installation.....	36
CHAPTER 4: PIEZOELECTRIC SENSOR CONFORMITY AND UNIFORMITY TEST	41
4.1 Lab Test of Conformity and Uniformity.....	41
CHAPTER 5: INTEGRATION LOAD DETERMINATION ALGORITHM FOR PIEZOELECTRIC SENSOR AND FIELD TEST	49
5.1 Weight Determination and Data Processing.....	49
5.1.1 Integration Load Determination Algorithm for Piezoelectric Sensor.....	49
5.1.2 Data Processing.....	51
5.2 Field Test Data and Results	55
5.2.1 Test Results of BLS.1 Sensor	58
5.2.2 Test Results of BLS.2 Sensor	63
5.2.3 Test Results of BLL.1 Sensor	68
5.2.4 Test Results of BLL.2 Sensor	72
5.2.5 Test Results of TC-B.1 Sensor.....	77
5.2.6 Test Results of TC-B.2 Sensor.....	81
5.3 Summary	85

CHAPTER 6: PAVEMENT DEFLECTION LOAD DETERMINATION ALGORITHM FOR PIEZOELECTRIC SENSOR AND FIELD TEST.....	87
6.1 Sensor Responses to Pavement Deflection.....	87
6.2 Signal Recovery Processing.....	89
6.3 Pavement Deflection Load Determination Algorithm for Piezoelectric Sensor.....	90
6.3.1 Results of Field Test Data.....	93
6.4 Summary.....	100
CHAPTER 7: FIBER OPTIC SENSOR FIELD TEST DATA.....	103
7.1 Equipment Setup.....	103
7.2 Data Records.....	104
7.3 Data Analysis.....	121
7.3.1 Center Wavelength Shift.....	121
7.3.2 Noise Floor.....	123
7.3.3 Measurement Error.....	124
7.4 Summary.....	127
CHAPTER 8: LAB TEST RESULTS OF MICROWAVE WIM SENSOR	129
8.1 Test Setup.....	129
8.2 Uniformity and Linearity Test.....	132
8.3 Measurement Error.....	136
CHAPTER 9: CONCLUSION	139
REFERENCES	141

LIST OF FIGURES

Figure 1-1: WIM Stations in the U.S.	3
Figure 1-2: Budget of WIM in WAVE Project.....	3
Figure 2-1: Normal Distribution (0, 1) Having 95% of Area Covered with Variable Value within ± 1.96	7
Figure 2-2: Typical Dynamic Forces Measured on Truck Axle for Medium Road Roughness.....	11
Figure 2-3: Possible Range of WIM Readings.	12
Figure 2-4: Definition of Stress and Strain.....	14
Figure 2-5: Bending Plate.....	15
Figure 2-6: Load Cell-Based WIM Sensor.....	16
Figure 2-7: Load Cell and Measurement Circuit.....	16
Figure 2-8: Piezoelectric Sensor.....	17
Figure 2-9: Use of Piezoelectric Materials.....	17
Figure 2-10: A Typical Piezoelectric Cable Configuration.....	18
Figure 2-11: Kistler LINEAS Quartz Sensor.....	18
Figure 2-12: Comparison between Ordinary Piezoelectric Cables and LINEAS Quartz Sensors.....	19
Figure 2-13: Capacitance Mat.....	20
Figure 2-14: A Schematic of an Intro-core Bragg Grating Sensor.....	21
Figure 3-1: Weigh Station Layout.....	29
Figure 3-2: WIM Zone and Entering Ramp.....	30
Figure 3-3: Bypass lane and static scale lane.....	30
Figure 3-4: Structure of Remote WIM System.....	32
Figure 3-5: Structure of Software on Server Host.....	34
Figure 3-6: Picture of Sensor Installation.....	37
Figure 3-7: Roadtrax BL Sensor.....	38
Figure 3-8: Vibracoax Sensor.....	38
Figure 3-9: Thermocoax's Embedded.....	38
Figure 3-10: ECM's Embedded.....	38
Figure 3-11: Layout of Sensor Installation.....	39
Figure 5-1: Integration Algorithm for Load Determination.....	50
Figure 5-2: An Example of Field Data.....	52
Figure 5-3: Method of Pulse Range Detection.....	53
Figure 5-4: Flowchart of Integration Load Determination Algorithm.....	54
Figure 5-5: Load Calibration Function ($y = 131.3x + 3351.1$) for BLS.1 on Drive Axle.....	58
Figure 5-6: Static Load vs. WIM Load of BLS.1 on Drive Axle.....	59
Figure 5-7: Error of Axle Load Measurement for BLS.1 on Drive Axle.....	60
Figure 5-8: Probability Density Function ($\mu=1.94\%$, $\sigma=13.25\%$) for BLS.1.....	60
Figure 5-9: Load Calibration Function ($y = 145.5x + 1232$) for BLS.1 on Trailer Axle.....	61
Figure 5-10: Error of Axle Load Measurement for BLS.1 on Trailer Axle.....	61
Figure 5-11: Probability Density Function ($\mu=2.25\%$, $\sigma=14.58\%$) for BLS.1 on Trailer Axle.....	62

Figure 5-12: Load Calibration Function ($y = 143.2x + 10963.3$) for BLS.2 on Drive Axle.....	63
Figure 5-13: Error of Axle Load Measurement for BLS.2 on Drive Axle.	63
Figure 5-14: Probability Density Function ($\mu=5.19\%$, $\sigma=22.9\%$) for BLS.2.....	64
Figure 5-15: Probability Density Function ($\mu=3.56\%$, $\sigma=15.52\%$) for Average of BLS.1 and BLS.2 on Drive Axle.	64
Figure 5-16: Load Calibration Function ($y = 186.7x + 6523.4$) for BLS.2 on Trailer Axle.....	65
Figure 5-17: Error of Axle Load Measurement for BLS.2 on Trailer Axle.	65
Figure 5-18: Probability Density Function ($\mu=5.33\%$, $\sigma=22.3\%$) for BLS.2.....	66
Figure 5-19: Probability Density Function ($\mu=3.79\%$, $\sigma=16.33\%$) for Average of BLS.1 and BLS.2 on Trailer Axle.	67
Figure 5-20: Load Calibration Function ($y = 144x + 5765$) for BLL.1 on Drive Axle.	68
Figure 5-21: Error of Axle Load Measurement for BLL.1 on Drive Axle.	68
Figure 5-22: Probability Density Function ($\mu=2.85\%$, $\sigma=15.8\%$) for BLL.1	69
Figure 5-23: Load Calibration Function ($y = 177.15x + 3542.31$) for BLL.1 on Trailer Axle.....	70
Figure 5-24: Error of Axle Load Measurement for BLL.1 on Trailer Axle.	70
Figure 5-25: Probability Density Function ($\mu=6.31\%$, $\sigma=23.46\%$) for BLL.1 on Trailer Axle.....	71
Figure 5-26: Load Calibration Function ($y = 158.2x + 8020.5$) for BLL.2 on Drive Axle.....	72
Figure 5-27: Error of Axle Load Measurement for BLL.2 on Drive Axle.....	72
Figure 5-28: Probability Density Function ($\mu=.4\%$, $\sigma=14.25\%$) for BLL.2 on Drive Axle.....	73
Figure 5-29: Probability Density Function ($\mu=2.62\%$, $\sigma=12.65\%$) for Average of BLL.1 and BLL.2 on Drive Axle.	73
Figure 5-30: Load Calibration Function ($y = 196.56x + 4845.83$) for BLL.2 on Trailer Axle.....	74
Figure 5-31: Error of Axle Load Measurement for BLL.2 on Trailer Axle.	74
Figure 5-32: Probability Density Function ($\mu=2.57\%$, $\sigma=15.23\%$) for BLL.2 on Trailer Axle.....	75
Figure 5-33: Probability Density Function ($\mu=4.44\%$, $\sigma=16.29\%$) for Average of BLL.1 and BLL.2 on Trailer Axle.....	76
Figure 5-34: Load Calibration Function ($y = 172.1x - 522.9$) for TC-B.1 on Drive Axle.....	77
Figure 5-35: Error of Axle Load Measurement for TC-B.1 on Drive Axle.	77
Figure 5-36: Probability Density Function ($\mu=0.38\%$, $\sigma=6.43\%$) for TC-B.1	78
Figure 5-37: Load Calibration Function ($y = 183.1x - 1039.8$) for TC-B.1 on Trailer Axle.....	79
Figure 5-38: Error of Axle Load Measurement for TC-B.1 on Trailer Axle.....	79
Figure 5-39: Probability Density Function ($\mu=0.43\%$, $\sigma=6.58\%$) for TC-B.1 on Trailer Axle.....	80
Figure 5-40: Load Calibration Function ($y = 176.9x - 541.7$) for TC-B.2 on Drive Axle.....	81
Figure 5-41: Error of Axle Load Measurement for TC-B.2 on Drive Axle.	81

Figure 5-42: Probability Density Function ($\mu=0.45\%$, $\sigma=6.03\%$) for TC-B.2	82
Figure 5-43: Probability Density Function ($\mu=0.42\%$, $\sigma=5.55\%$) for Average of TC-B.1 and TC-B.2 on Drive Axle.	82
Figure 5-44: Load Calibration Function ($y = 183.2x - 1186.2$) for TC-B.2 on Trailer Axle.	83
Figure 5-45: Error of Axle Load Measurement for TC-B.2 on Trailer Axle.....	83
Figure 5-46: Probability Density function ($\mu=0.45\%$, $\sigma=7.11\%$) for TC-B.2 on Trailer Axle.....	84
Figure 5-47: Probability Density Function ($\mu=0.44\%$, $\sigma=5.6\%$) for Average of TC-B.1 and TC-B.2 on Trailer Axle.....	85
Figure 6-1: An Example of Pavement Deflection.....	88
Figure 6-2: An Example of Signal Recovery.....	90
Figure 6-3: Deflection Curve Fitted to Remove Pavement Vibration (Dynamic Load)..	91
Figure 6-4: Flowchart of Pavement Deflection Weighing Method for.....	92
Figure 6-5: Load Calibration Function ($y = 63698.1x - 1116.4$) for TC-B.1	93
Figure 6-6: Error of Axle Load Measurement for TC-B.1 on Drive Axle.	93
Figure 6-7: Probability Density Function ($\mu=0.14\%$, $\sigma=6.86\%$) for TC-B.1	94
Figure 6-8: Load Calibration Function ($y = 70570.4x - 2111.6$) for TC-B.1 on Trailer Axle.....	95
Figure 6-9: Error of Axle Load Measurement for TC-B.1 on Trailer Axle.....	95
Figure 6-10: Probability Density Function ($\mu=0.36\%$, $\sigma=9.54\%$) for TC-B.1 on Trailer Axle.....	96
Figure 6-11: Load Calibration Function ($y = 57070.8x - 1054.0$) for TC-B.2 on Drive Axle.	97
Figure 6-12: Error of Axle Load Measurement for TC-B.2 on Drive Axle.	97
Figure 6-13: Probability Density Function ($\mu=0.1\%$, $\sigma=6.30\%$) for TC-B.2.....	98
Figure 6-14: Load Calibration Function ($y = 62906.7x - 2526.7$) for TC-B.2 on Trailer Axle.....	99
Figure 6-15: Error of Axle Load Measurement for TC-B.2 on Trailer Axle.....	99
Figure 6-16: Probability Density Function ($\mu=0.65\%$, $\sigma=9.48\%$) for TC-B.2 on Trailer Axle.....	100
Figure 7-1: (a) Inside View of Developed Signal Detector; (b) Front of Detector; (c) Back of Detector.....	103
Figure 7-2: (a) Front of I-sense-14000; (b) Back of I-sense-14000.....	104
Figure 7-3: The Selected Vehicle and the Axle Group.....	105
Figure 7-4: Plot of Measured Data for Field Test Group 1. The test was performed on August 11, 2004.....	107
Figure 7-5: Plot of Measured Data for Field Test Group 2. The test was performed on August 11, 2004.....	107
Figure 7-6: Plot of Measured Data for Field Test Group 3. The test was performed on August 11, 2004.....	108
Figure 7-7: Plot of Measured Data for Field Test Group 4. The test was performed on August 11, 2004.....	108
Figure 7-8: Plot of Measured Data for Field Test Group 5. The test was performed on August 11, 2004.....	109

Figure 7-9: Plot of Measured Data for Field Test Group 6. The test was performed on August 11, 2004.	109
Figure 7-10: Plot of Measured Data for Field Test Group 7. The test was performed on August 11, 2004.	110
Figure 7-11: Plot of Measured Data for Field Test Group 8. The test was performed on August 11, 2004.	110
Figure 7-12: Plot of Measured Data for Field Test Group 9. The test was performed on August 11, 2004.	111
Figure 7-13: Plot of Measured Data for Field Test Group 10. The test was performed on August 11, 2004.	111
Figure 7-14: Plot of the Measured Data for Field Test Group 1. The test was performed on August 31, 2004.	112
Figure 7-15: Plot of Measured Data for Field Test Group 2. The test was performed on August 31, 2004.	112
Figure 7-16: Plot of Measured Data for Field Test Group 3. The test was performed on August 31, 2004.	113
Figure 7-17: Plot of Measured Data for Field Test Group 4. The test was performed on August 31, 2004.	113
Figure 7-18: Plot of Measured Data for Field Test Group 5. The test was performed on August 31, 2004.	114
Figure 7-19: Plot of Measured Data for Field Test Group 6. The test was performed on August 31, 2004.	114
Figure 7-20: Plot of Measured Data for Field Test Group 7. The test was performed on August 31, 2004.	115
Figure 7-21: Plot of Measured Data for Field Test Group 8. The test was performed on August 31, 2004.	115
Figure 7-22: Plot of Measured Data for Field Test Group 9. The test was performed on August 31, 2004.	116
Figure 7-23: Plot of Measured Data for Field Test Group 10. The test was performed on August 31, 2004.	116
Figure 7-24: Plot of Measured Data for Field Test Group 11. The test was performed on August 31, 2004.	117
Figure 7-25: Plot of Measured Data for Field Test Group 12. The test was performed on August 31, 2004.	117
Figure 7-26: Plot of Measured Data for Field Test Group 13. The test was performed on August 31, 2004.	118
Figure 7-27: Plot of Measured Data for Field Test Group 14. The test was performed on August 31, 2004.	118
Figure 7-28: Plot of Measured Data for Field Test Group 15. The test was performed on August 31, 2004.	119
Figure 7-29: Plot of Measured Data for Field Test Group 16. The test was performed on August 31, 2004.	119
Figure 7-30: Plot of Measured Data for Field Test Group 17. The test was performed on August 31, 2004.	120
Figure 7-31: Plot of Measured Data Generated by the Designed Detector. The test was performed on August 11, 2004.	120

Figure 7-32: Peaks and Center Wavelength Shift.....	121
Figure 7-34: Noise Floor.....	123
Figure 7-35: Maximum Noise Level of Field Test Data Obtained on August 11, 2004.....	124
Figure 7-36: Maximum Noise Level of Field Test Data Obtained on August 31, 2004.....	124
Figure 7-37: Plot of Error for Field Test Data Obtained on August 11, 2004.....	126
Figure 7-38: Plot of Error for Field Test Data Obtained on August 31, 2004.....	126
Figure 8-1: Data Acquired during One Sweep by DAQ Card.....	129
Figure 8-2: (a) Signal of Power Detector's Output Before Interpolation and LPF Processing; (b) Signal of Power Detector's Output after Interpolation and LPF Processing.....	130
Figure 8-3: Test Setup.....	132
Figure 8-4: Measured Data at Position 1.....	133
Figure 8-5: Linearity of Sensor's Output at Position 1.....	134
Figure 8-6: Linear Fitting Curves of Sensor's Output for All 11 Positions and the Average of All Curves.....	135
Figure 8-7: Linearity of Sensor's Output at 11 Positions Separately.....	135
Figure 8-8: Measurement Errors.....	136
Figure 8-9: Measurement Errors Excluding Positions 4 and 7.....	137
Figure 8-10: Resonant Frequency Shift Measured by Network Analyzer.....	138
Figure 8-11: Measurement Error Based on Test Data.....	138

LIST OF TABLES

Table 2-1: ASTM WIM Classification.....	8
Table 2-2: ASTM E 1318-02 Performance Requirements for WIM Systems.....	9
Table 2-3: California Department of Transportation Performance Requirements for WIM Systems.....	9
Table 5-1: Static Load in Field Test.....	56
Table 5-2: Results of Test on BLS Sensors.....	66
Table 5-3: Results of Test on BLL Sensors.....	75
Table 5-4: Results of Test on TC-B Sensors.....	84
Table 6-1: Result of Test on TC-B Sensor with Pavement Deflection Weighing Method.....	100
Table 7-1: Axle Static Loads Recorded by the DPS Weigh Station on August 11, 2004.....	105
Table 7-2: Vehicle Static Load Recorded by the DPS Weigh Station on August 31, 2004.....	106
Table 7-3: Center Wavelength Shifts Calculated from Field Test Data Obtained on August 11, 2004.....	122
Table 7-4: Center wavelength shift calculated from field test data obtained on August 31, 2004.....	122
Table 7-5: Measurement Error of Field Test Data Obtained on August 11, 2004.....	125
Table 7-6: Measurement Error of Field Test Data Obtained on August 31, 2004.....	125
Table 8-1: Load Applied on Sensor.....	131

CHAPTER 1:INTRODUCTION

1.1 Background

A nation's transportation infrastructure is its lifeline. An efficient and safe road network allows goods to reach the markets quickly, thus stimulating economic activity and ensuring trade competitiveness. According to the Highway Statistics of the United States, over 46,000 miles of interstate, combined with a network of almost 4 million miles of other roads, make up the nation's lifeline. Each year, nearly five trillion dollars' worth of goods is transported via the nation's lifeline by commercial trucks. Unfortunately, commercial truck traffic also contributes greatly to the cost of deteriorating highways across the nation. The increased costs of maintenance with the diminished highway funds available have meant that many roads are now in or rapidly approaching a critical condition. Industry experts estimate that there is currently a \$300+ billion shortfall to repair roads and bridges to an acceptable standard. For many years, states have been looking at developing a system that can be beneficial to the trucking industry, the taxpayers and the states, while helping to protect the infrastructure. It is the Weigh-In-Motion (WIM) technology which provides benefits to all parties involved.

WIM is described as "the process of measuring the dynamic tire forces of a moving vehicle and estimating the corresponding tire loads of the static vehicle" in the American Society for Testing and Materials (ASTM) Standard E 1318 [1]. The WIM systems mainly serve two very important functions:

1. Screening illegally overloaded trucks to prevent premature deterioration of the infrastructure, and
2. Data collection for planning and management purposes.

The WIM system can overcome the limitations of static weighing scales. The high-speed WIM system can even be used under highway speeds, making it possible to weigh vehicles without interrupting the traffic flow. It is normal for a static weigh station to have a long waiting line for trucks that even results in the closure of the weigh station. Compared with the static weigh station, a WIM station is an efficient and cost-effective choice that will minimize unnecessary stops and delays for truckers [2].

The importance of WIM technology is recognized worldwide for its application to traffic stream characterization and law (load limit) enforcement. In fact, the concept of WIM is not new. As early as the 1950's, research on measuring the mechanical strain was induced in load cells and highway bridges. By measuring the mechanical strain in load cells or bridges, the vehicle's weight can be estimated. This is the strain-gauge based WIM system. In the 1970's and 1980's, sensors embedded in or placed on the road became commercially available. Later, the on-board WIM system was developed, which was installed on the truck to monitor the weight continuously and accurately. A new fiber optic sensor that will be immune to the interference of an electromagnetic signal, such as sparks from engines, lightening, etc., and a much higher sensitivity than traditional sensors is currently being researched. Due to the low loss feature, it could also be used for long distance transmission. But there is no commercially available fiber optic-based product at this time.

Because of the many advantages that a WIM system has to offer, there are many demands all over the world, and research is widely conducted on WIM systems. Currently, there are more than 1000 operational WIM stations on the US highway system. The distribution is shown in [Figure 1-1](#). In Europe, France and the United Kingdom (UK) initiated the development of the WIM system as early as the 1970's. In 1992, the Forum of European Highway Research Laboratories (FEHRL) underlined WIM as a priority topic for cooperative actions to be supported by the DG VII of the European Commission. As a result, COST323 (WIM-LOAD) (1993-1998), part of the Cooperation in Science and Technology (COST) Transport program, was initiated as the first European cooperative action on WIM of road vehicles. Its objective was to promote the development and implementation of WIM techniques and systems throughout Europe. Another objective of COST323 was to provide a significant step forward in the understanding of WIM performance and applications with respect to highway network manager's and transportation planner's requirements. In addition, another project, Weight in Motion of Axles and Vehicles for Europe (WAVE) (1996-1998) also studied in Europe [\[3\]](#). The budget is presented in [Figure 1-2](#).

In the United States, the famous Long-Term Pavement Performance (LTPP) (1987-2007) by the Federal Highway Administration (FHWA) is a 20-year-long program that has WIM system research as an important part of highway performance data collection. In August 2003, the contract was awarded for WIM Phase 1 of the SPS Traffic Pooled Fund Study. This phase of the study will focus on assessment, calibration, and performance evaluations of LTPP WIM sites.

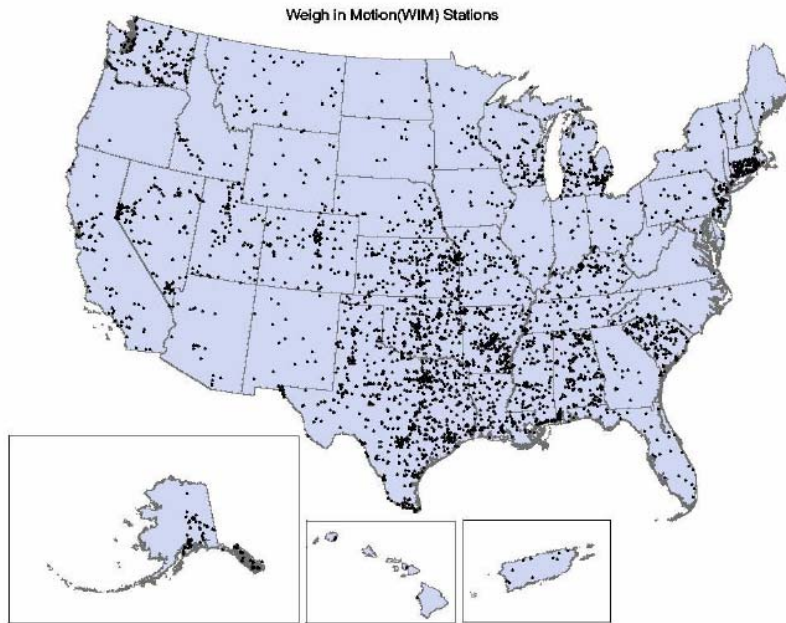


Figure 1-1: WIM Stations in the U.S.

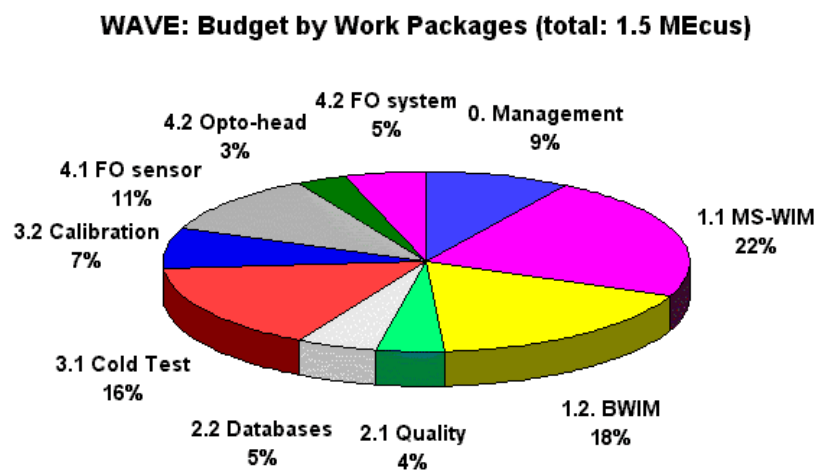


Figure 1-2: Budget of WIM in WAVE Project [3]

1.2 WIM System Classification

There are many ways to characterize WIM systems, but the following categories are most common:

- according to the application, the WIM system can be classified as weight enforcement, data collection, etc.;
- according to the type of sensors used in the system: bending plate, load cell, piezoelectric, fiber optic, etc.;
- according to portability: permanent, portable and on-board, etc.; and
- according to traffic speed: high speed (>20 MPH) and low speed (<20 MPH) system.

CHAPTER 2: WIM SYSTEM STANDARD AND WIM SENSORS

In order to evaluate WIM sensors, the accuracy, error sources and other standards of a WIM system are discussed in this chapter. In addition, WIM sensors are introduced and compared.

2.1 WIM System Accuracy

Usually, WIM systems are used to estimate vehicles' static weights from the measurement of dynamic loads. The difference between static and dynamic loads is considered to be a WIM error if precautions have been taken to ensure the pavement surface in the proximity of the WIM sensor meets recommended smoothness criteria (ASTM E 1318). To set up a criterion to describe the WIM system's performance, precision errors and accuracy errors are discussed below.

The WIM accuracy is represented as follows:

$$A = \frac{W_d - W_s}{W_s} \times 100\% \quad (2-1)$$

where A : WIM measurement accuracy;

W_d : Axle weight or gross weight measured by WIM system;

W_s : Axle weight or gross weight measured by static scale.

A WIM system is defined to be accurate if the mean value of the [equation \(2-1\)](#) for a sample of weight observations does not differ significantly from zero [4]. The bias from that mean value is considered to be a systematic error existing in the WIM measurement. Proper calibration of a WIM system can minimize systematic error by choosing a sample of vehicles from the traffic stream that is representative of the spectrum of vehicles intended to be weighed. Considering the “accuracy” in the [equation \(2-1\)](#) as a statistic variable, the systematic error can be defined as:

$$\mu_A = E[A_n] \quad (2-2)$$

where μ_A : Systematic error

A_n : Variable defined in equation (2-1), the n subscript means the number of samples.

Based on the systematic error's definition, the precision of the statistic given in (2-2) can be defined as the range within which a specific percentage of all observations can be expected to fall. This is represented as follows:

$$\mu_A \pm X_{\alpha/2} * \sigma_A \quad (2-3)$$

where μ_A : Defined in (2-2),

$X_{\alpha/2}$: Critical value from the standard normal distribution associated with the level of confidence α ;

σ_A : The standard deviation of A .

Generally, the level of confidence employed is 95%, as stated in the ASTM standard. With α equal to 95% for standard normal distribution, the corresponding $X_{\alpha/2}$ is equal to 1.96. As shown in Figure 2-1, the normal distribution, with zero as a mean and one as the standard deviation, will have its 95% area covered with variable values between -1.96 and 1.96. The ASTM standard uses 95% as a confidence level to estimate the precision of WIM scale measurement, but not all the vendors and manufacturers follow this standard for WIM system measurement evaluation. Some use $\pm \sigma_A$ as the criterion, which means that 68% of the normal distribution area is within one standard deviation of the mean. In order to compare the precisions of different sensors, the ASTM standard has been chosen for this study. Although the accuracy and precision are different, according to the definition, it is common to use the word 'accuracy' to describe the precision of WIM measurement.

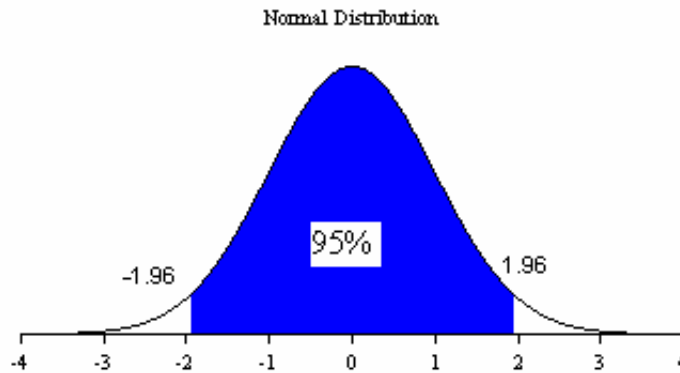


Figure 2-1: Normal Distribution (0, 1) Having 95% of Area Covered with Variable Value within ± 1.96 .

2.2 ASTM WIM System Classification

The commonly cited standard for WIM devices is ASTM standard E 1318, Specification for Highway Weigh-In-Motion Systems with User Requirements and Test Methods. According to the standard, WIM systems can be classified into four types by speed range, application, and other characteristics. [Table 2-1](#) illustrates the classification in detail. The four types of WIM systems defined in this specification are:

- Type I, which represents a high-accuracy data collection system,
- Type II, which represents a low-cost data collection system,
- Type III, which represents a WIM system for use in a sorting application at a weigh station on an entrance ramp (either bending plate WIM or deep pit load cell WIM) – Note that this classification is for speeds in the range of 15 to 50 MPH (24 to 80 km/h), which is below typical interstate or expressway speeds; and
- Type IV, which represents a low-speed, weigh-in-motion scale system.

It is obvious that there are no applications of piezoelectric sensors at weight enforcement stations due to their limited accuracy.

Table 2-1: ASTM WIM Classification.

	CLASSIFICATION			
	Type I	Type II	Type III	Type IV
Speed Range	10-70 mph (16-113 km/h)	10-70 mph (16-113 km/h)	15-50 mph (24-80 km/h)	0-10 mph (0-16 km/h)
Application	traffic data collection	traffic data collection	Weight enforcement station	weight enforcement station
Number of Lanes	up to four	up to four	up to two	up to two
Bending Plate	X	X	X	X
Piezoelectric Sensor	X	X		
Load Cell	X	X	X	X
Wheel Load	X		X	X
Axle Load	X	X	X	X
Axle-Group Load	X	X	X	X
Gross Vehicle Weight	X	X	X	X
Speed	X	X	X	X
Center-to-Center Axle Spacing	X	X	X	X
Vehicle Class	X	X		
Site Identification Code	X	X	X	X
Lane and Direction of Travel	X	X	X	
Date and Time of Passage	X	X	X	X
Sequential Vehicle Record Number	X	X	X	X
Wheelbase	X	X		
Equivalent Single-Axle Load	X	X		
Violation Code	X	X	X	X

Source: FHWA "States' Successful Practices Weigh-in-Motion Handbook" and ASTM E 1318

2.3 WIM System Performance Requirements

In the ASTM standard E 1318-02, accuracy and other requirements for each type of WIM system are given. In [Table 2-2](#), the minimum accuracy (maximum error) of each type of WIM system is defined in the statistical sense. Maximum gross vehicle weight error is less than the axle load and wheel load error. Measurements of speed and axle spacing are also required.

Table 2-2: ASTM E 1318-02 Performance Requirements for WIM Systems.

Functional Performance Requirements for WIM Systems (Tolerance for 95% Probability of Conformity)			
Function	Type I	Type II	Type III
Wheel Load	+/- 25%		+/- 20%
Axle Load	+/- 20%	+/- 30%	+/- 15%
Axle-Group Load	+/- 15%	+/- 20%	+/- 10%
Gross Vehicle Weight	+/- 10%	+/- 15%	+/- 6%
Speed	+/- 2 km/h (1 mph)		
Axle-Spacing	+/- 0.15 m (0.5 ft)		

In addition to the ASTM standard, there are some other standards and requirements for WIM systems used by different transportation departments or organizations. Table 2-3 shows the requirement of the California Department of Transportation.

Table 2-3: California Department of Transportation Performance Requirements for WIM Systems.

Parameter	Mean	Standard Deviation
Vehicle weight		
Single axle	$\pm 5\%$	8%
Tandem axle	$\pm 5\%$	6%
Gross weight	$\pm 5\%$	5%
Axle spacing	± 150 mm (6 in)	300 mm (12 in)
Vehicle length	± 300 mm (12 in)	460 mm (18 in)
Vehicle speed	± 1.6 km/h (1 mi/h)	3.2 km/h (2 mi/h)

^a Source: McCall, W. and W.C. Vodrazka Jr., *States' Successful Practices Weigh-In-Motion Handbook*, Center for Transportation Research and Education (CTRE), Iowa State University, Dec. 15, 1997, http://www.ctre.iastate.edu/research/wim_pdf/index.htm.

2.4 Sources of Error

The WIM system is used to measure the actual loads or force applied to a pavement by a moving truck. However, the static weight estimation is used in the WIM system because in some applications, such as law enforcement of overloading, the only criterion is to use the static weight. As stated, the difference between static and dynamic weight is considered to be the error of WIM measurement. The actual load on the pavement applied by a vehicle is more than just the weight of the vehicle itself.

According to the Oak Ridge National Laboratory's (ORNL) research, the sources of error can be classified into four basic categories: vehicle-dependent error, environment-dependent error, system-dependent error, and road-dependent error. Vehicle-dependent error includes characteristics of the vehicle itself, such as the suspension system, tire characteristics, aerodynamic lift and acceleration, etc. The environment-dependent error is going to change the performance of the pavement, e.g., temperature variation, wind, rain, snow and moisture, etc. Since WIM data are acquired by the WIM system, the system-dependent error has to be considered. Generally, the system error comes from noise, non-uniformity, aging, etc. It is very hard to eliminate all these sources of error, but the proper selection or build of the installation site can prevent some errors effectively, especially for the road-dependent error. The criteria of site selection include horizontal curvature, roadway grade, cross slope, lane width, pavement structure, and road roughness. Please refer to [5] for more detailed information.

2.4.1 Vehicle Dynamics

Among those sources of error, vehicle dynamics have a great contribution. According to F. Scheuter, it is the largest possible error for WIM systems [6]. As a vehicle travels, the dynamic load applied to the road varies significantly due to the vehicle bouncing, acceleration or deceleration, and shifting of the load, either physically or just in its distribution through the suspension system [7]. A sample of field data of dynamic wheel forces is shown in Figure 2-2. The vehicle dynamics are not only sources of error in WIM measurement but also the sources of accelerated pavement damage and vibrations. According to research conducted at ORNL, the vehicle's dynamic weight can vary over time by as much as $\pm 20\%$ to $\pm 50\%$ as it travels down the highway [8], and there are two frequency ranges (1-5 Hz and 9-14 Hz) typically excited in pavement vibration. The lower frequency range (1-5 Hz) is typically associated with rigid body motion combined with suspension performance (body mode). The other frequency range (9-14 Hz) is associated with tire characteristics, such as balance quality, circumference and speed (tire mode).

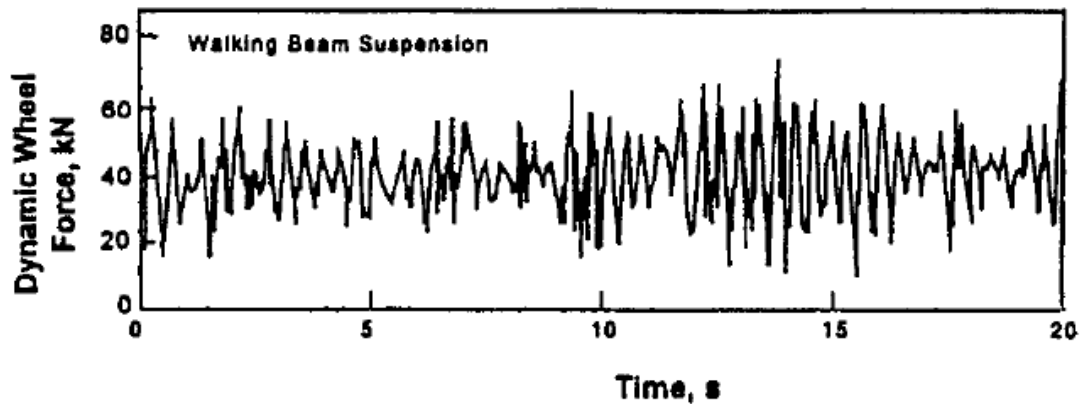


Figure 2-2: Typical Dynamic Forces Measured on Truck Axle for Medium Road Roughness.

Source: [9]

According to Michael S. Mamlouk [9], the total load imparted to the pavement by a moving vehicle is the sum of the static load or weight of the vehicle and the forces generated by the dynamic movements of the truck. Because of the existence of vehicle dynamic, the WIM sensor in fact just records a “snap-shot” load, which rarely represents the actual static weight shown in Figure 2-3. In order to reduce the effects of vehicle dynamics, multiple sensors can be used to cover a longer distance of measurement. Furthermore, the research on pavement characteristics, such as vibration, deflection and elasticity, etc., will be helpful to explain the WIM error from vehicle dynamics.

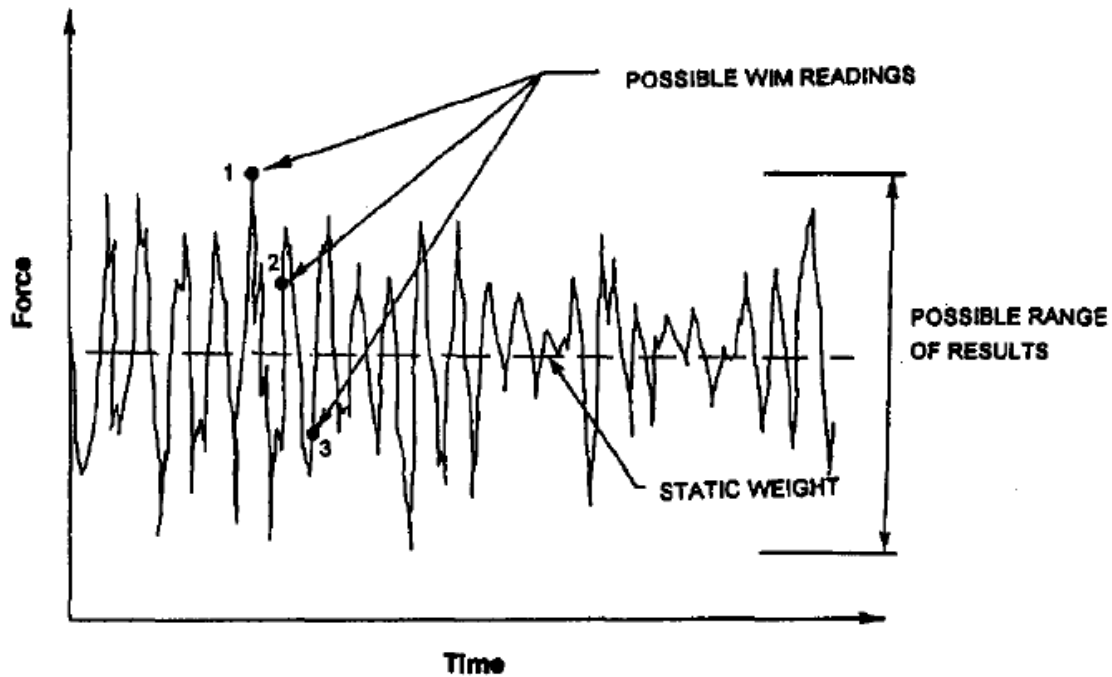


Figure 2-3: Possible Range of WIM Readings.

Source: [9]

2.5 Considerations for Selecting an Installation Site

As vehicle dynamics is the most significant factor affecting WIM measurement, efforts are made to reduce the vehicle dynamics and improve the measurement accuracy. Research on pavement and vehicle interaction has focused on improvements to suspension systems, reducing vibration, and improving driving quality [10]. However, the most effective way to reduce the vehicle dynamics applied to the pavement is to build a better pavement. Considering the cost, selecting a better site for WIM installation is more economical than building a new section of pavement. To select a suitable section, the ASTM standard for WIM devices sets up some useful guidelines including the geometric design, pavement condition, and general characteristics of the potential site [11]. Also, there is very little difference found for the requirements among Types I, II, III, and IV, as shown in Table 2-4.

Table 2-4: ASTM Standard (E 1318) Geometric Design Requirements.

Characteristic	Type I	Type II	Type III	Type IV
Horizontal Curvature	radius \geq 1740m 46m before/after			
Roadway Grade	\leq 2% 46m before/after	\leq 2% 46m before/after	\leq 2% 46m before/after	\leq 1% 91m before/after
Cross Slope (lateral)	\leq 2% 46m before/after	\leq 2% 46m before/after	\leq 2% 46m before/after	\leq 1% 46m before/after
Lane Width	3 to 4.5m 46m before/after			

Vehicle bounce is the result of variations in the vertical load imposed by a moving axle, which increases with road roughness and leads to greater variations in the instantaneous axle loads [12]. Therefore, the condition of the pavement will have a significant effect on the measurement accuracy of the WIM system. The guideline in the ASTM Standard E 1318-94 states that for a distance of 46 m (150 feet) before and after the sensor, the pavement surface “shall be maintained in a condition such that a 150 mm (6 inches) diameter circular plate 3 mm (0.125 inches) thick cannot be passed beneath a 6 m (20 feet) long straight edge.”

In addition to the requirements above, the installation site should meet some general requirements such as availability of power supply and communication utilities, control cabinet, site drainage, etc.

2.6 WIM Sensors

As an important part of the WIM system, WIM sensors directly affect the accuracy of the whole WIM system. There are many choices for WIM sensors. In the commercial market, we can find sensors such as bending plate, load cell, and piezoelectric sensors, etc. Although WIM sensors are different, they have a similar working principle. They can detect the pressure or force from the vehicle’s tires. Usually, the indirect measurement parameters are stress or strain. The definition of these two parameters is shown in Figure 2-4. In addition to the sensor itself, some useful load

transfer mechanisms are necessary in the load measurement. In this study, an introduction will be given for all these sensors. Some experiments were conducted in lab and test sites.

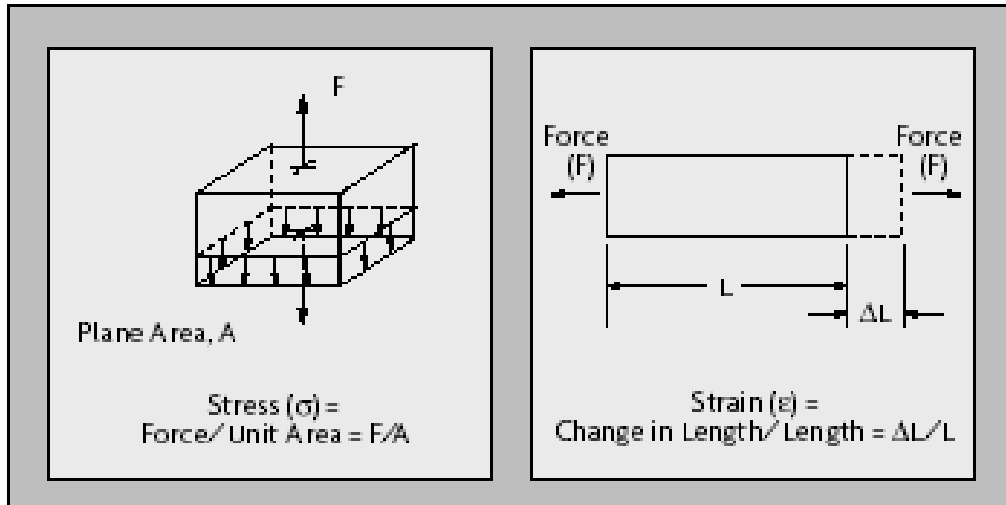


Figure 2-4: Definition of Stress and Strain.

2.6.1 Bending Plate

A bending plate is in fact is a steel plate with strain gauges attached to its bottom. According to specifications published by Fairbank Scale, Inc., there are six strain gauges along the steel plate, allowing the scale to be linearized across the entire weighing width. When the vehicle passes over, the strain introduced by the loading can be measured and converted to dynamic weight. This kind of sensor can be used for either high-speed or low-speed measurement, and the accuracy is very high, usually to within 10% of the static load. However, it is hard to do the maintenance, and the installation is difficult and expensive. The commercial bending plate sensor is shown in [Figure 2-5](#).



Figure 2-5: Bending Plate.

Source: DP 121 Weigh-in-Motion Technology

2.6.2 Load Cell

In a load cell-based WIM sensor, there is a load cell mounted centrally in each scale mechanism, as shown in [Figure 2-6](#). All loading on the weighing surface sensor will be transferred to the load cell through load transfer tubes. Normally there are two 6-foot long scales covering one lane width, which will weigh wheels at both ends of an axle simultaneously. The scale is mounted in a frame and installed in a vault which is flush with the road surface.

This kind of sensor is sensitive and is the most accurate one among the commercially available WIM sensors. The accuracy can reach as good as within 6% or better. However, it is also expensive and hard to install. The sensor part of the load cell and the measurement circuit are shown in [Figure 2-7](#).

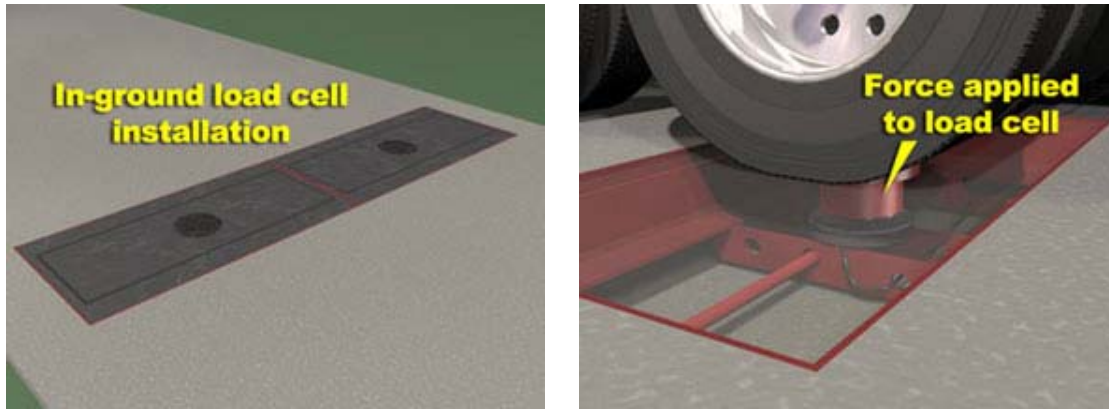


Figure 2-6: Load Cell-Based WIM Sensor.

Source: DP 121 Weigh-in-Motion Technology

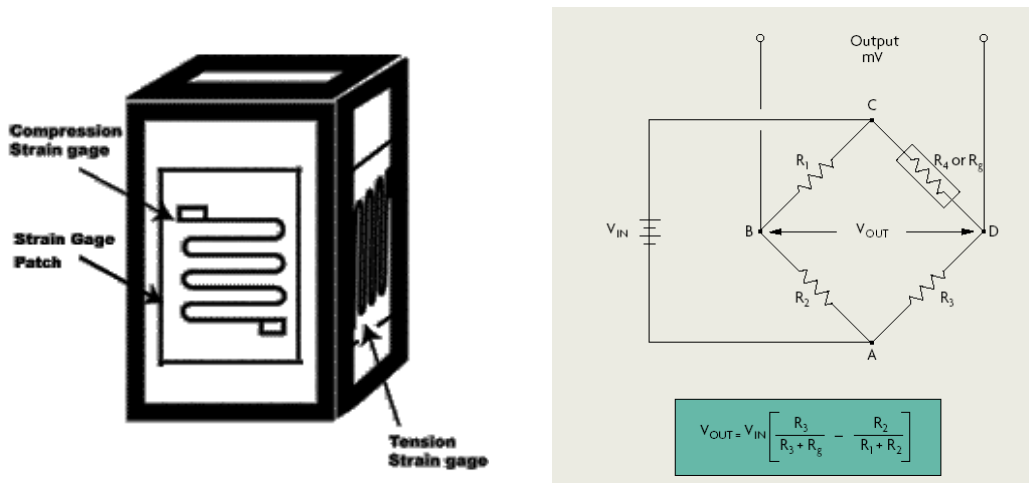


Figure 2-7: Load Cell and Measurement Circuit.

2.6.3 Piezoelectric Sensor

The piezoelectric WIM sensor is a piezoelectric material-based sensor. If there is pressure exerted on this material, a charge will be produced on both sides of the piezoelectric material. This sensor can measure dynamic pressure that is good for the high-speed WIM system, but it is not good for static weighing. The advantages of the piezoelectric sensor are that it is easy to use and very inexpensive.

The inevitable disadvantage is that the limited width of the piezoelectric sensor makes the single sensor measurement accuracy not as good as we need, normally only to within about 15 % of the static load. The sensor is shown in [Figure 2-8](#).

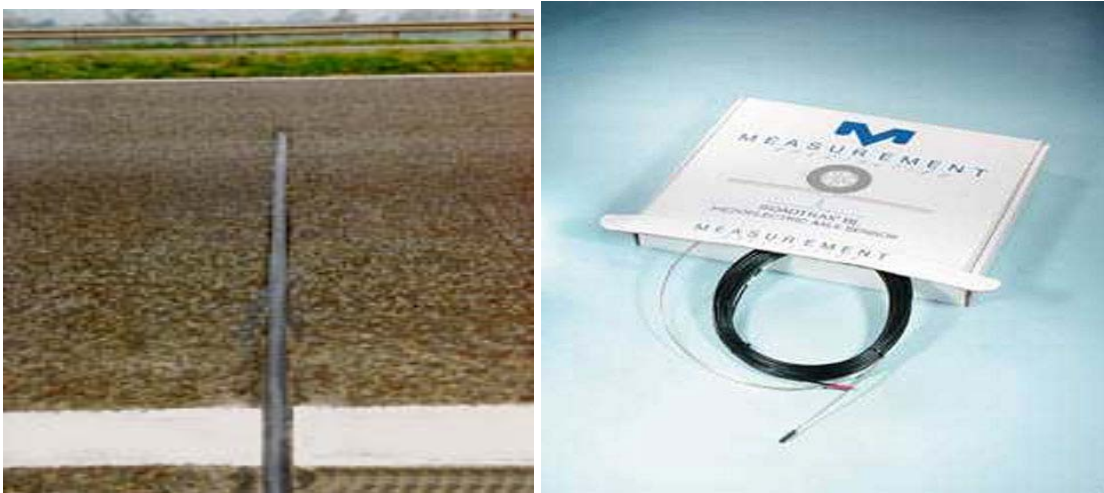


Figure 2-8: Piezoelectric Sensor.

Source: DP 121 Weigh-in-Motion Technology

The principle of the piezoelectric sensor is shown vividly in [Figure 2-9](#), where different designs are used to produce a charge and estimate the corresponding stress and strain, etc. Normally, piezoelectric materials are composed of polymer molecular chains (e.g., polyvinylidene fluoride), ceramics (e.g., lead zirconate titanate), or crystals (e.g., quartz). Piezoelectric sensors are commonly coaxial with a metal core, piezoelectric material, and a metal outer layer [\[13\]](#). A typical structure of piezoelectric sensor is shown in [Figure 2-10](#).

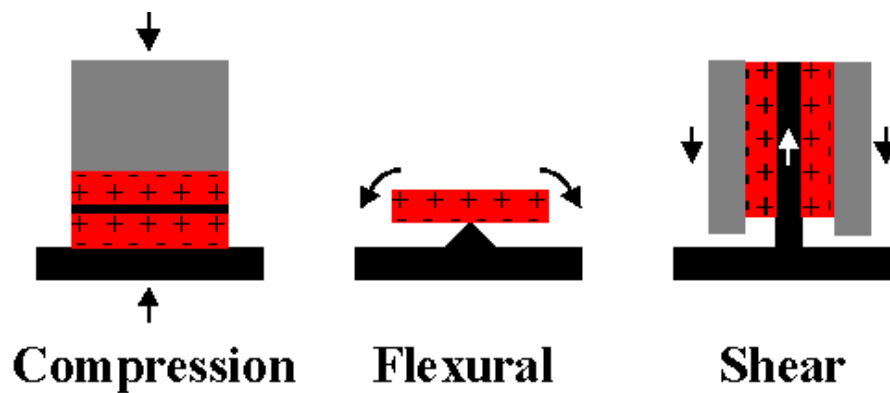


Figure 2-9: Use of Piezoelectric Materials.

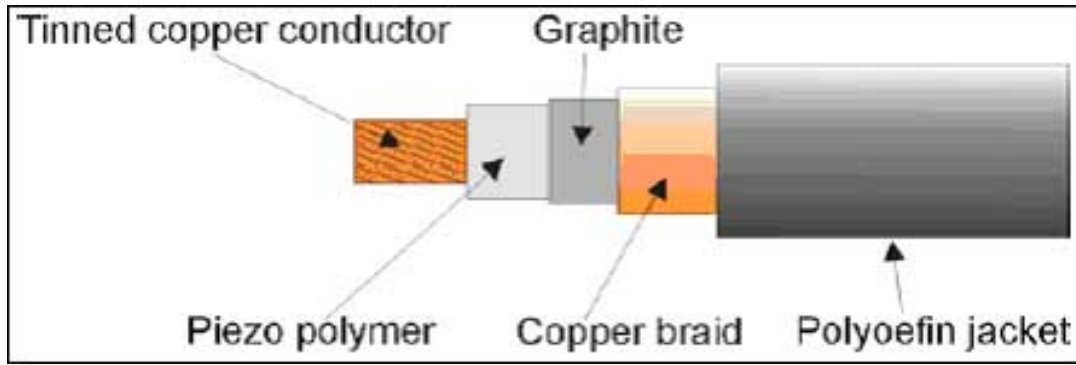


Figure 2-10: A Typical Piezoelectric Cable Configuration.

There are some other piezo sensor configurations. For example, Kistler Instruments Corporation developed a quartz-based LINEAS sensor for traffic monitoring. It is shown in Figure 2-11. It uses foam to reduce the horizontal force and an aluminum tube to protect sensor materials. A narrow metal plate is used as the platform for registering wheel load contact.

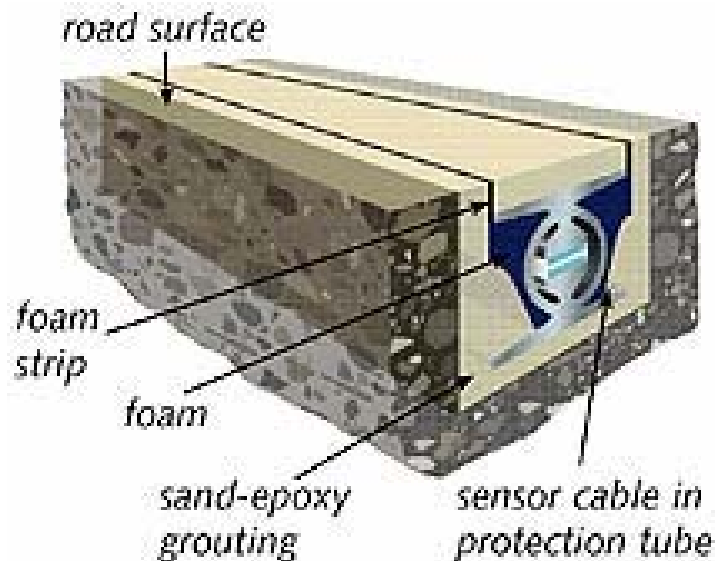
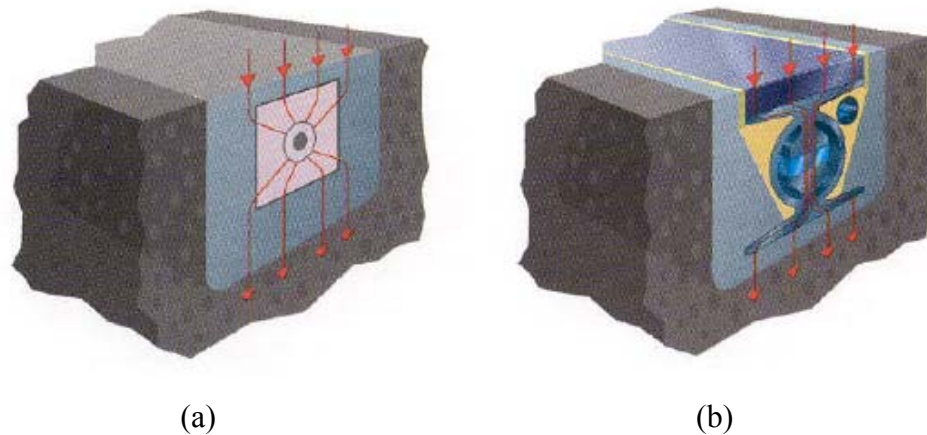


Figure 2-11: Kistler LINEAS Quartz Sensor.

Source: Kistler Instruments Corporation

The quartz sensor's output has a good linearity and remains stable under changing temperature. Although piezoelectric material cannot perform real static measurements, quartz, on the other hand, has an ultra-high insulation resistance, which is good for static

measurements [14]. Comparing the structure of the LINEAS sensor with a traditional piezoelectric cable sensor (shown in Figure 2-12), the LINEAS sensor shows sensitivity only to the vertical force, instead of all directions as do the traditional piezoelectric cable sensors. The mechanism used in the structural design of the sensor can absorb forces imposed in the horizontal direction and only allow vertical force to be applied to the quartz materials inside the metal tube.



(a) Ordinary piezo cable sensors are sensitive to pressure from any direction.
(b) LINEAS quartz sensors are sensitive to vertical force only.

Figure 2-12: Comparison between Ordinary Piezoelectric Cables and LINEAS Quartz Sensors.

Source: Kistler Instruments Corporation

2.6.4 Capacitance Mat

A capacitance mat WIM sensor has two or more metal plates placed parallel to each other to form a capacitor. Therefore, the conductors will carry equal but opposite charges on both plates, respectively. While a vehicle passes over the mat, the distance between the plates will decrease, and the capacitance increases. Recording and analyzing the change proportional to the axle load allows estimation of the axle load. Usually, the capacitance mats are manufactured using stainless steel, brass, aluminum, polyurethane, rubber, etc. A picture of the capacitance mat is shown in Figure 2-13.



Figure 2-13: Capacitance Mat.

Source: DP 121 Weigh-in-Motion Technology

2.6.5 Fiber Optic Sensor

A fiber optic sensor is an excellent candidate for WIM devices and has been proven in measuring bridge load in civil engineering and in gauging surface strain in aerospace engineering. The optic fiber's immunity to electromagnetic interference makes it suitable for installation in places where other WIM technologies might be adversely affected (such as close to rail tracks and power stations) [15]. Successful tests and deployments of fiber optic sensors have occurred in research sponsored by the Federal Highway Administration (FHWA) and the Florida DOT. Their initial results indicate accurate axle counts and vehicle classifications when compared to data from piezoelectric devices [16]. The Los Alamos National Laboratory and the U.S. Department of Energy have also teamed up to develop second-generation weigh-in-motion sensors based on fiber optics interferometry. The state of New Mexico also has studied the possibilities of using fiber optic sensors for WIM purposes. The Naval Research Laboratory (NRL) and the Vehicle Detection Clearinghouse located at New Mexico State University are both carrying out a study on a Fiber Bragg Grating (FBG) sensor [17].

Nowadays, Fiber Bragg Grating sensors, shown in [Figure 2-14](#), are playing a significant role in many fields (e.g., petroleum, civil, and aeronautical engineering) due to their durability, multiplexing capability, light weight, and electromagnetic immunity.

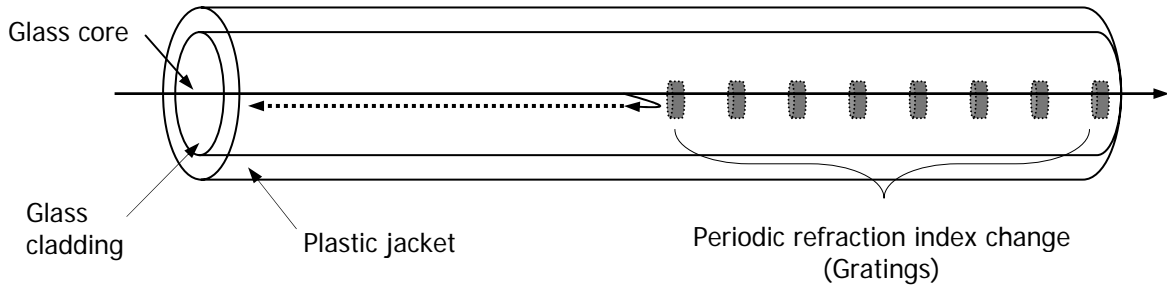


Figure 2-14: A Schematic of an Intro-core Bragg Grating Sensor.

The Fiber Bragg grating sensor's functionality is based on the Bragg optic fiber grating's (BOFG) sensitivity to temperature, strain, and pressure. When an FBG is expanded or compressed, the grating spectral response changes. As the grating period is half of the input light wavelength, the wavelength signal will be reflected coherently to make a large reflection. The operating wavelength is reflected instead of transmitted.

A simple Fiber Bragg grating is composed of a longitudinal periodic modulation of the refractive index in the core of a single-mode optic fiber. It is a reflective type filter, and the operating wavelength is reflected instead of transmitted ([Figure 2-15](#)). Light propagates along the core of an optic fiber and is scattered by each grating plane. If the Bragg condition is not satisfied, the reflected light from each of the subsequent planes becomes progressively out of phase and will eventually cancel out [18]. The wavelength of the light to be reflected will decide the grating spacing.

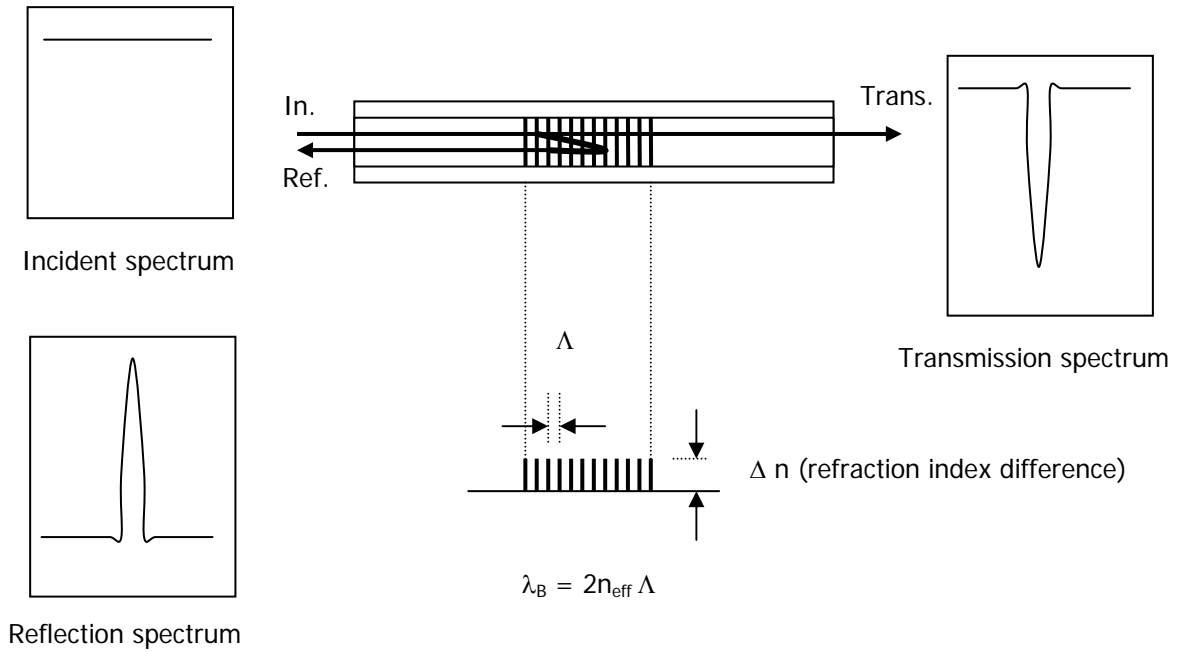


Figure 2-15: Typical Spectral Response from a Bragg Grating.

Figure 2-16 illustrates the basic approach with two initially matched gratings: sensing grating (SG) and reference grating (RG). In this scheme, light from a broadband source is reflected to the reference grating by the sensing grating. The reference acts as a rejection filter that transmits minimal light to the photo detector, PD 1. When a load is applied to the sensing grating, its refractive index is linearly changed, resulting in some parts of the light reflected from the sensing grating falling outside of the rejection band of the RG and being transmitted to PD 1. It is the quasi-square reflection profiles that permit a linear relationship between the change in strain or temperature encoded in the Bragg wavelength and the intensity of the light transmitted by the reference grating [18].

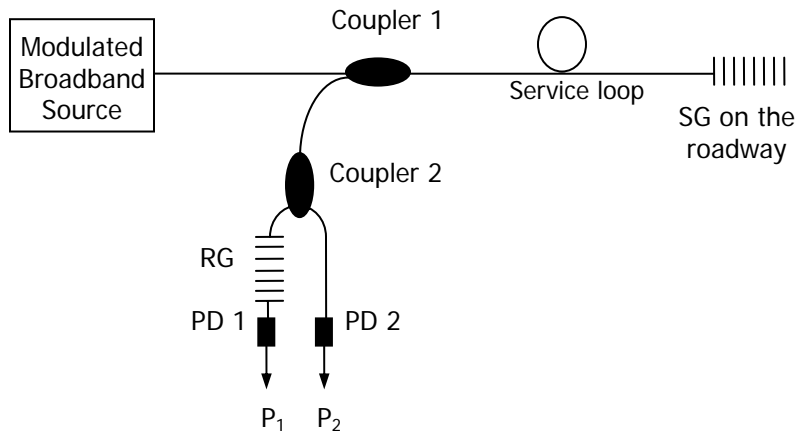


Figure 2-16: Schematic Diagram of the Interrogation Scheme.

2.6.6 Microwave WIM Sensor

Although sensors like the bending plate and load cell can be used for static or very low speed WIM application, they are still very expensive and hard to install. The piezoelectric sensor is relatively inexpensive, but it is not capable of static weight measurement and has many disadvantages such as the capability to be easily broken, electromagnetic interference, inaccuracy, etc. Considering the advantages of strip WIM sensors, a new sensor based on microwave cavity theory was developed by the researchers.

The structure of such a sensor is a cylindrical metal cavity shown in [Figure 2-17](#), which is easy to manufacture and install. Furthermore, the metal body (such as steel) of the sensor is strong enough for the WIM application without being broken under a tough environment. Thanks to the properties of the electromagnetic field and performance of the cavity, the uniformity of the sensor can be estimated accurately. In addition to these advantages, the sensor is also immune to electromagnetic interference.

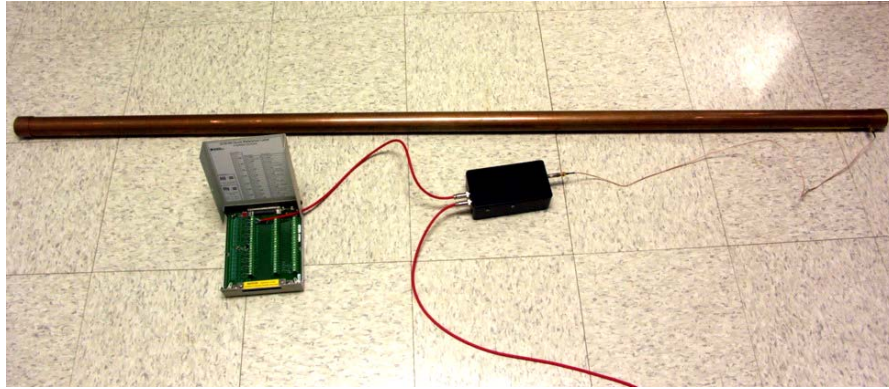


Figure 2-17: **Innovative Microwave WIM Sensor.**

Since this sensor is an active sensor, the microwave signal should be generated and coupled into the cavity, and the parameter used for measuring loads is the shift of the resonant frequency. When pressure is applied to the sensor, the resonant frequency will shift. A fast frequency sweeping system was designed in this study to monitor the shift of the resonant frequency.

After considering all these requirements, a fast frequency sweeping circuit was designed, as shown in Figure 2-18.

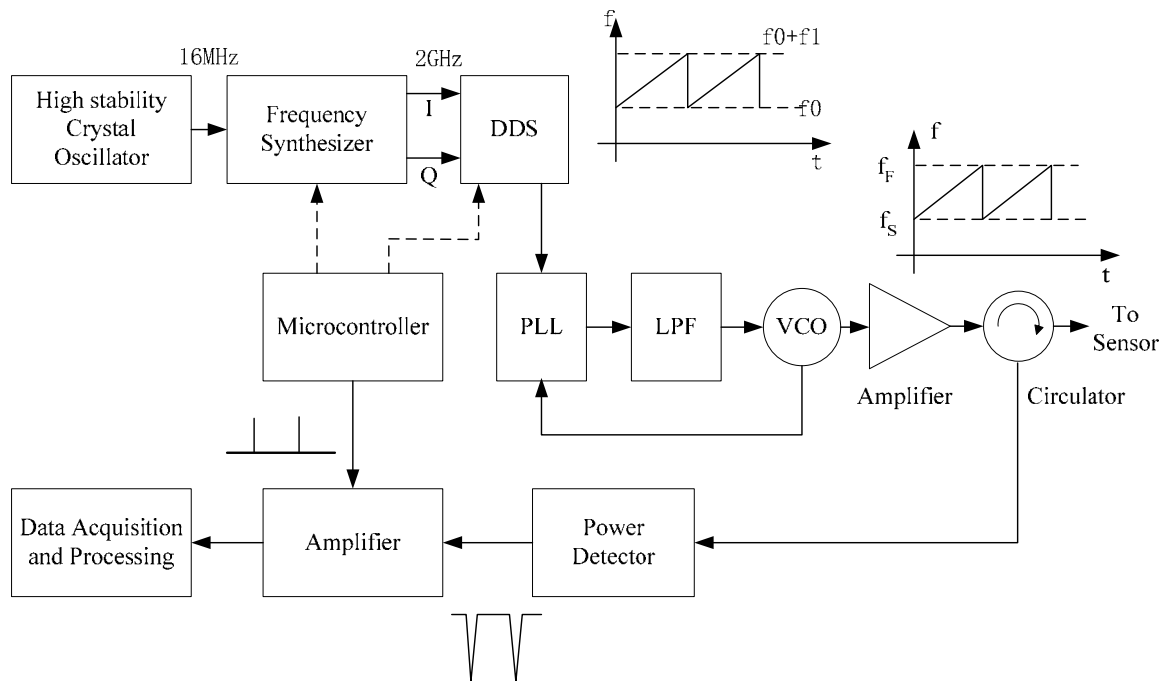


Figure 2-18: Fast Frequency Sweeping System.

After a sweeping signal is generated, an amplifier is used to strengthen the signal and then feed it into the sensor through a circulator with enough isolation to isolate the output signal and the returned signal from the sensor. The reflected signal from the sensor is received through the circulator and detected by a power detector. If the output signal has flat amplitude, the power of the received signal can be used to detect the resonant frequency directly. The relationship between the synchronize signal, sweeping signal, and output of the power detector is shown in [Figure 2-19](#).

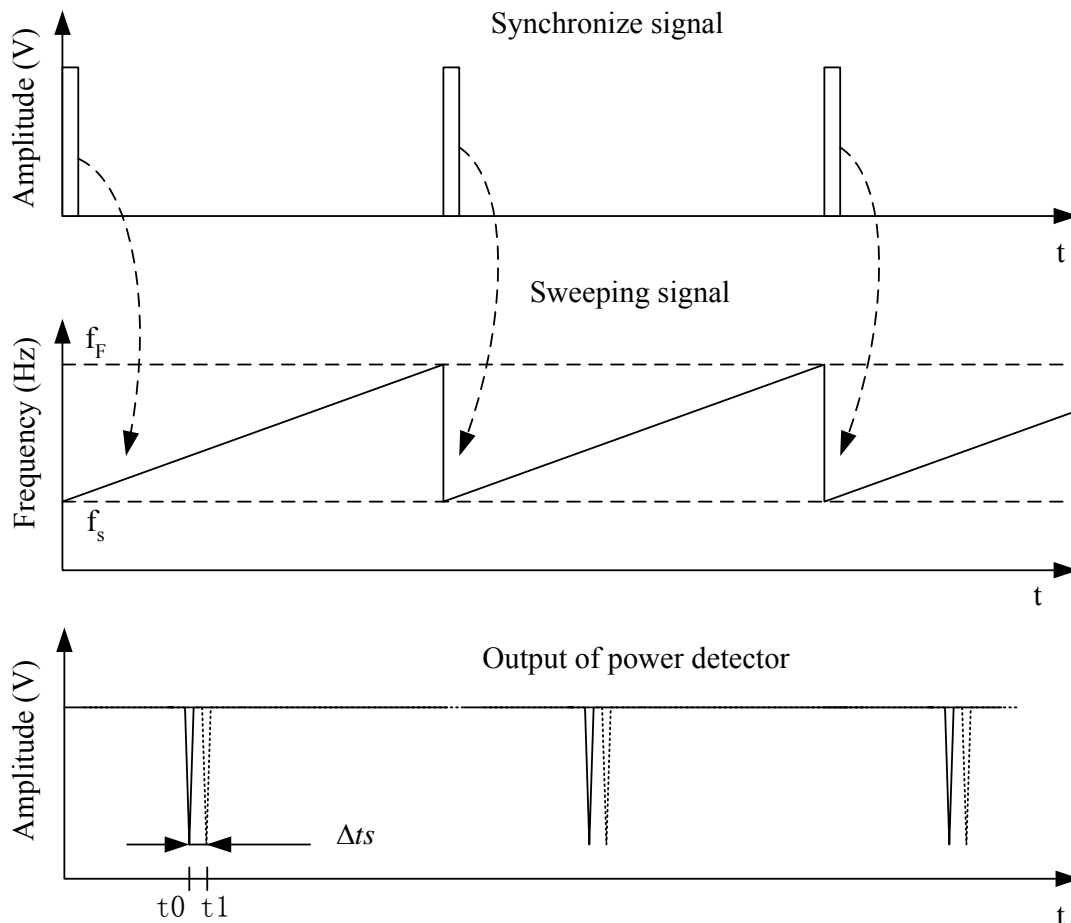


Figure 2-19: Relationship between Signals.

According to the design proposed above, a four-layer printed circuit board (PCB) board was made, and the whole system as implemented is shown in [Figure 2-20](#).

In the circuit, both the direct digital synthesizer (DDS) and synthesizer can be programmed through a Serial Peripheral Interface (SPI) port by the microcontroller. The

synchronize signal is also generated by the same microcontroller. According to different requirements, the program can be modified to control the frequency sweeping speed and sweeping range through the control of the output of DDS.

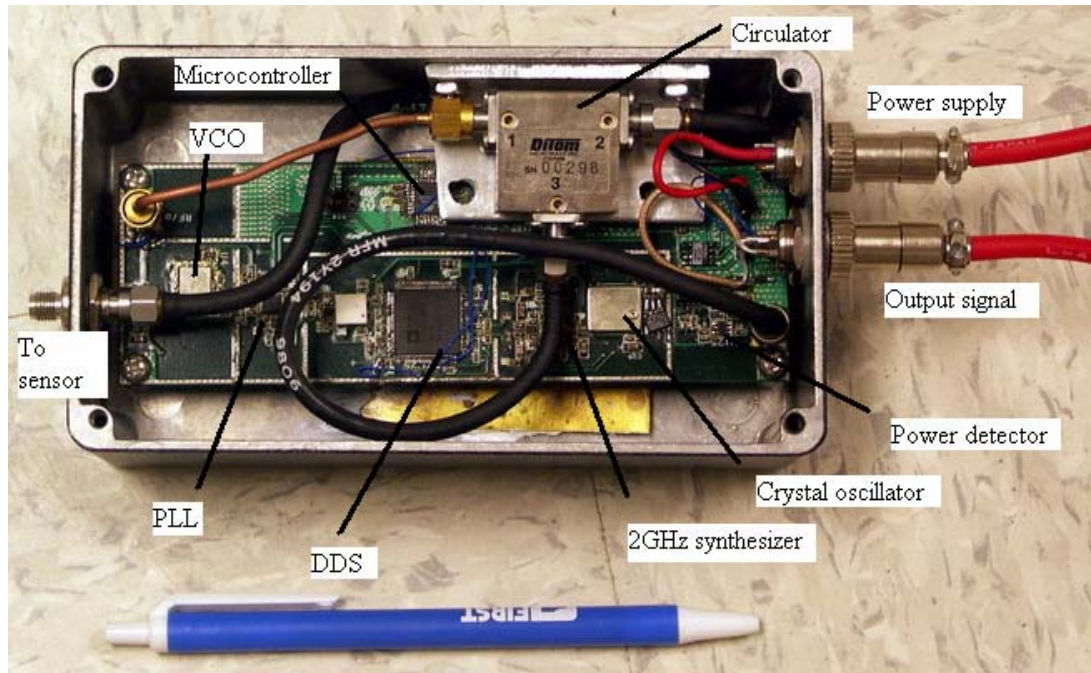


Figure 2-20: Photo of the Circuit.

2.6.7 Commercial WIM Sensors Comparison

Different WIM sensor formats will result in different measurement results. In order to choose the best sensors for this study, we reviewed a selection of sensors, focusing on published accuracy, installation requirements, durability, cost, etc. The summary is shown in [Table 2-5](#), where we find the piezoelectric sensor is the most inexpensive one, but has limited accuracy. The load cell is the most accurate one, and it is the most expensive one. As for the fiber optic sensor, it is not practical for application right now.

Table 2-5: Considerations in Selecting WIM Sensors.

	Kistler	Single Load Cell	Bending Plate	Piezoelectric
Accuracy (GVW) (95% confidence level)	2 σ =10%	2 σ =6%	2 σ =10%	2 σ =15%
Service Life	6 years	20 years	6 years	4 years
Initial Budgetary Equipment Cost	\$ 20,500 /lane	\$39,000 /lane	\$8,000 /lane	\$2,500 /lane
Initial Budgetary Installation Cost	\$12,000 /lane	\$20,800 /lane	\$13,500 /lane	\$6,500 /lane
Life Cycle Cost (over 12 year period)	\$7,500 /year/lane	\$6,200 /year/lane	\$6,400 /year/lane	\$4,750 /year/lane

CHAPTER 3: REMOTE WIM SYSTEM DESIGN AND INSTALLATION

3.1 Test Site Description

The test site selected for this study is located at an existing weigh station operated by the Department of Public Safety (DPS) in the northbound direction of interstate highway (IH) 45, about 60 miles north of Houston, Texas. The layout of the weigh station is shown in Figure 3-1. When a truck enters the WIM zone, shown in Figure 3-2, the static weight of the truck is estimated and compared with a preset value to detect if it has an overloaded or unbalanced load. If it is an overloaded or unbalanced load, the traffic light at the end of WIM zone will lead the truck to a static scale operated by DPS personnel who will make a further inspection. Otherwise, the truck will re-enter the highway through a bypass lane. There is a parking lot in the weigh station used for further investigation of trucks that have to enter the static scale again in order to return to the highway. A picture of the bypass lane and static scale lanes is shown in Figure 3-1.

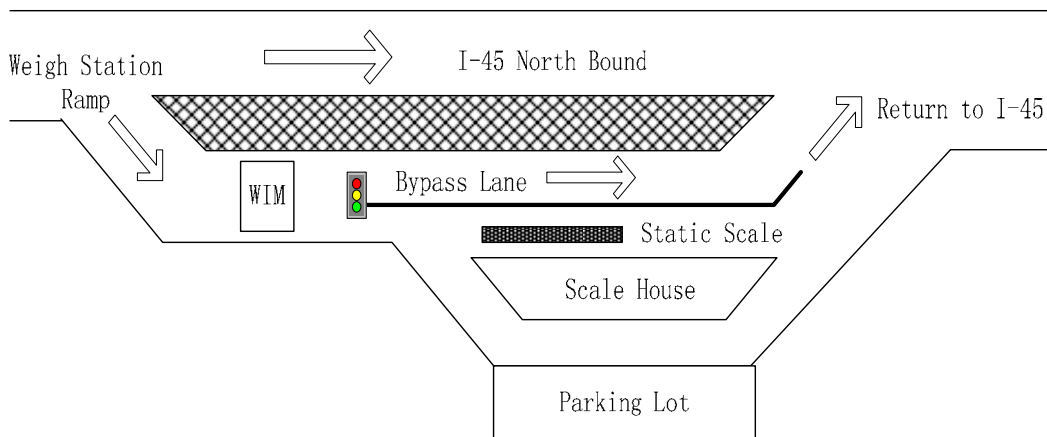


Figure 3-1: Weigh Station Layout.



Figure 3-2: WIM Zone and Entering Ramp



Figure 3-3: Bypass lane and static scale lane

The sensors under evaluation were embedded in the WIM zone pavement, a very smooth concrete pavement section upstream from the static scale of the weigh station and the bypass lane. The speed limit in the WIM zone is 15 MPH. When trucks enter the weigh station from the ramp, they usually need to reduce the speed rapidly which affects the WIM system's measurement accuracy, especially for the piezoelectric sensor. During this deceleration period, the wheel loads will change significantly due to load transfer between axles. However, since this location is within the weigh station, traffic can be controlled and static axle loads are easily obtained. Therefore, this site was good for our study of low-speed WIM application. The WIM section's pavement has a three-layer structure. The first layer is a concrete pavement about 12 inches thick. The second layer is a 4 inches thick hot-mix subbase and the third layer, lime treated subgrade, has a nominal thickness of 10 inches.

3.2 Remote WIM System Design

To evaluate various WIM sensors, including piezoelectric sensors, fiber optic sensors and microwave sensors, a remote accessible WIM system was designed. The remote functions of the system such as telnet, ftp, http, and Point-to-Point Protocol (PPP) services make it possible to do the real time system monitoring, software upgrade, and data logging. The structure of the system is shown in [Figure 3-4](#).

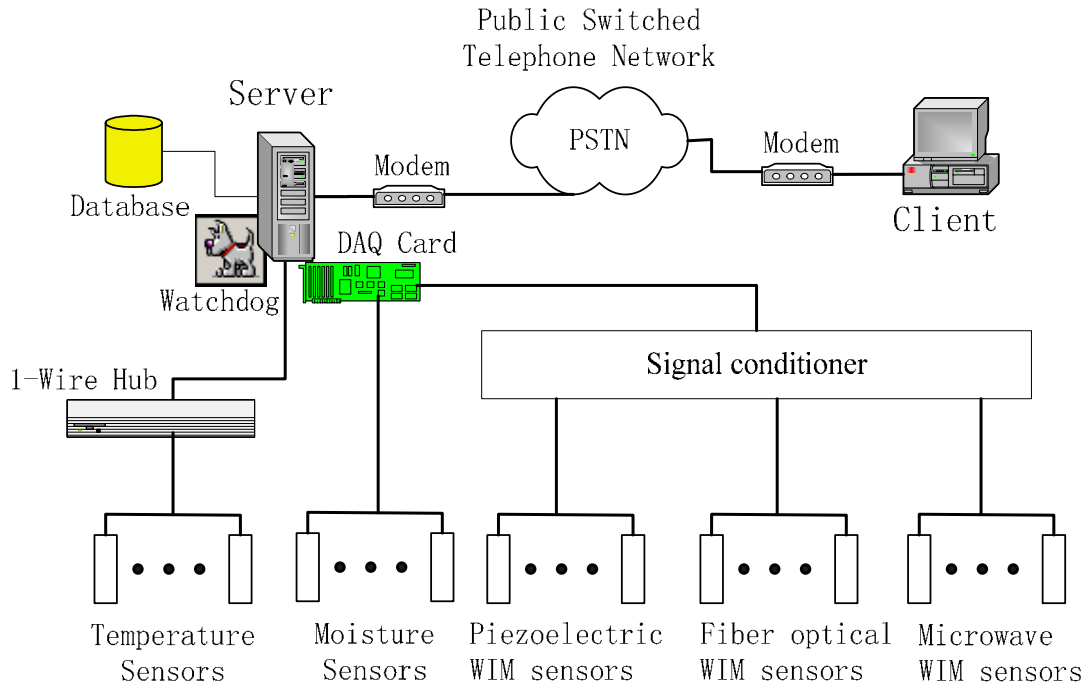


Figure 3-4: Structure of Remote WIM System.

3.2.1 Hardware Configuration

There are three kinds of WIM sensors included in the remote WIM system. They are piezoelectric sensors, fiber optic sensors, and microwave WIM sensors. In addition to these WIM sensors, other sensors such as one-wire temperature sensors and moisture sensors are also installed for monitoring the effects of temperature and moisture. The one-wire temperature sensors, DS1920 from Dallas Semiconductor, are connected by the one-wire network, and data is fed to the host computer through a one-wire hub. The data from the moisture sensors are obtained by the data acquisition card periodically. The signal conditioner is used to convert the signals of the sensors to the voltage acceptable by the data acquisition (DAQ) card. As for the piezoelectric sensors, the signal conditioners are no more than an amplifier. However, for the fiber optic sensor and microwave WIM sensors, the signal conditioners are circuits used to transmit, receive, and process the optic or microwave signal for acquiring corresponding voltage signals. The fiber optic WIM sensor is an active sensor which has a measurement channel and a reference channel, and the signal conditioner receives not only the measured signal, but also the reference signal. Necessary processing must be conducted in the signal

conditioner. The phase shift, frequency shift, or other parameters' variations are measured and used for weight determination. Normally, the signal conditioner will function as both an amplifier and signal translator. Further study on fiber optic WIM sensors can be found in the corresponding research [19]. The circuit of the microwave WIM sensor is discussed later.

Once the signal is converted by the signal conditioner, we can use a DAQ card to acquire the signal. The data acquisition can be accomplished by using the universal data acquisition equipment or by designing a specific data acquisition circuit. Today's general computer speeds are fully capable of handling the volume of data generated by the WIM station. Universal data acquisition equipment is used with the WIM system for its flexible and multi-functional advantages. The performance of the data acquisition is very important to the weight determination. Data acquisition equipment with sampling rates high enough to ensure the accuracy of the measurement is required. An external trigger function with the proper driver for the data acquisition equipment is expected.

Since the host server of the WIM system is usually installed in the field under a harsher outdoor environment, a watchdog is very important for computer reset in some conditions like power failure and program malfunctions. In our system, one PCI version watchdog is installed in the server to monitor the system status, and a corresponding code is written to refresh the timer in the watchdog to keep it from overflowing. Once the timer inside the watchdog overflows for any reason, the server will be rebooted automatically. The value written into the timer can be set with dip switches on the watchdog card or controlled by a program.

To access the remote functions, a broadband internet connection or phone line is necessary. Considering that the field installation of a WIM system is usually near a highway, a phone line is often available. Therefore, the Point-to-Point Protocol service is a good way to make a connection between the server host and client host. When the client host needs to connect with the server host, it dials the phone number assigned to the server host. Then, the server host will initialize a PPP service to setup the connection between the computers. Once the connection is established, other internet services can be initiated. The services provided include telnet, ftp, http, etc.

3.2.2 Software Configuration

Once the hardware was set up, the software is installed and configured on the server host to make the load measurements and provide remote internet functions. The software installed on the server host can be divided into two categories: one is the support software, and the other is the WIM software. The structure of software on the server is shown in [Figure 3-5](#).

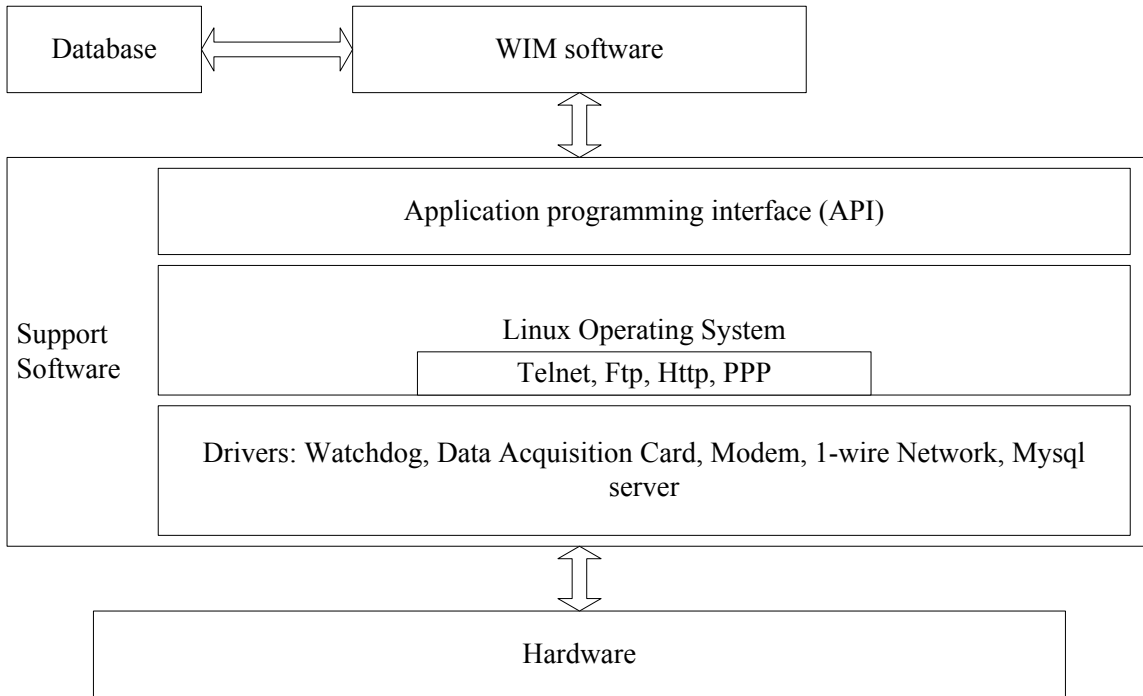


Figure 3-5: Structure of Software on Server Host.

Support Software

The support software is used to support and configure the server host with all kinds of services. Without these support software, the server cannot work properly. First of all, an operating system has to be installed before other software. Considering the services provided by the remote server, the Linux operating system was chosen for its reliability, open sources, powerful networking, and easy configuration. In our system, Redhat Linux 9.0 was installed on a Pentium 4 PC. Provided services include telnet, ftp,

http, PPP, etc. With these services, the client PC can log into the server to make a program or manage the server remotely.

Drivers for the data acquisition card, watchdog, one-wire network, and modem are all necessary to operate the devices. Without these drivers installed, further programming of the device is impossible. Some functions can be embedded into the WIM software for enabling the control of these devices.

The database is the software required on the server host for the purpose of data archiving and query since much data are collected for both passing vehicles and the environment (e.g., axle loads, vehicle speed, axle spacing, temperatures and in-pavement moisture, etc.). Saving WIM data in a database is better than saving separate data files because it facilitates data management and data queries. In order to support the remote functions, a MySQL database was installed and configured on the server host. The MySQL database is a free relational database, compatible with the standard SQL functions, and has a lot of client application software available for client host installation. The server software of MySQL is the engine of the whole MySQL database, which supports multiple user applications and can be combined with the PHP, short for Hypertext Preprocessor, and program to realize the web database applications.

In addition to the above software, the application programming interface (API) provided by the vendors of one-wire devices and the data acquisition card were also installed on the server host. The API offers many functions which can be called by the WIM software to accomplish certain tasks. It is very useful for handling the corresponding hardware.

WIM Software

After the installation and configuration of the support software, the WIM software is programmed and installed. The main functions of the WIM software are:

- Refresh the timer of the watchdog;
- Start the data acquisition process;
- Implement axle load determination algorithm;

- Save measurement results and environment information; and
- Allow web query of WIM data.

The refreshment of the watchdog's timer is necessary to keep the PC from being rebooted under normal conditions. Rebooting occurs when the program gets bogged down due to erroneous calculations. When a coming vehicle triggers the data acquisition card by the activation of the trigger sensor, the data acquisition process starts to conduct the data acquisition at a certain sampling frequency. After acquiring the data, the axle load, axle spacing, and vehicle speed are calculated by the axle load determination algorithm, and the results are saved in the database on server. Furthermore, the information of the environment is also saved in the database for further query. According to the application, the web query is implemented by the joint program of PHP and MySQL database. Then the saved data in the database is available for remote access from platform-independent software on the client host, such as IE.

3.3 Sensor Installation

In order to evaluate piezoelectric sensors, products from three major vendors were installed in the WIM zone. The picture of the WIM zone after the piezo installation is shown in [Figure 3-6](#), and the layout schematic of sensor installation is shown in [Figure 3-11](#).



Figure 3-6: Picture of Sensor Installation.

To enhance the vertical pressure measurement and reduce side-stress effects, different techniques are used by different vendors for designing sensors. For the sensor named “Roadtrax BL,” manufactured by Measurement Specialties Inc., it is bare, and the shape of the sensor’s transverse section is designed to be flat, with narrow side edges to reduce side (horizontal) stresses (Figure 3-7). For the “Vibracoax” sensor, manufactured by Thermocoax Inc., the shape of the sensor’s transverse section is circular, having uniform sensitivity in the radial direction. It is shown in Figure 3-8. To minimize the force transferred from the horizontal direction, an aluminum channel, in which the sensor is encapsulated (shown in Figure 3-9), is used by Thermocoax. Furthermore, the sensor encapsulated by ECM has two additional foam rubber buffers placed along the vertical sides of the aluminum channel to reduce the sensor’s response to horizontal stresses [20]. The ECM encapsulated sensor is shown in Figure 3-10.

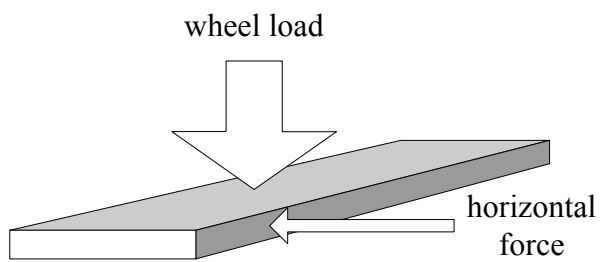


Figure 3-7: Roadtrax BL Sensor.

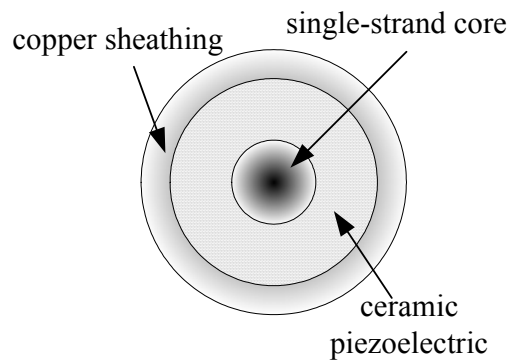


Figure 3-8: Vibracoax Sensor.

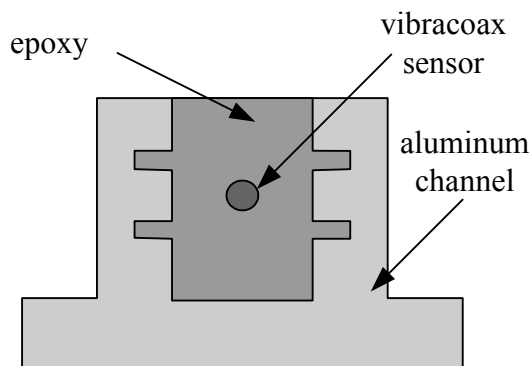


Figure 3-9: Thermocoax's Embedded Sensor.

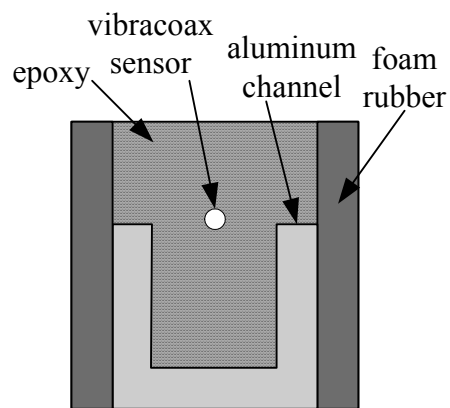


Figure 3-10: ECM's Embedded Sensor.

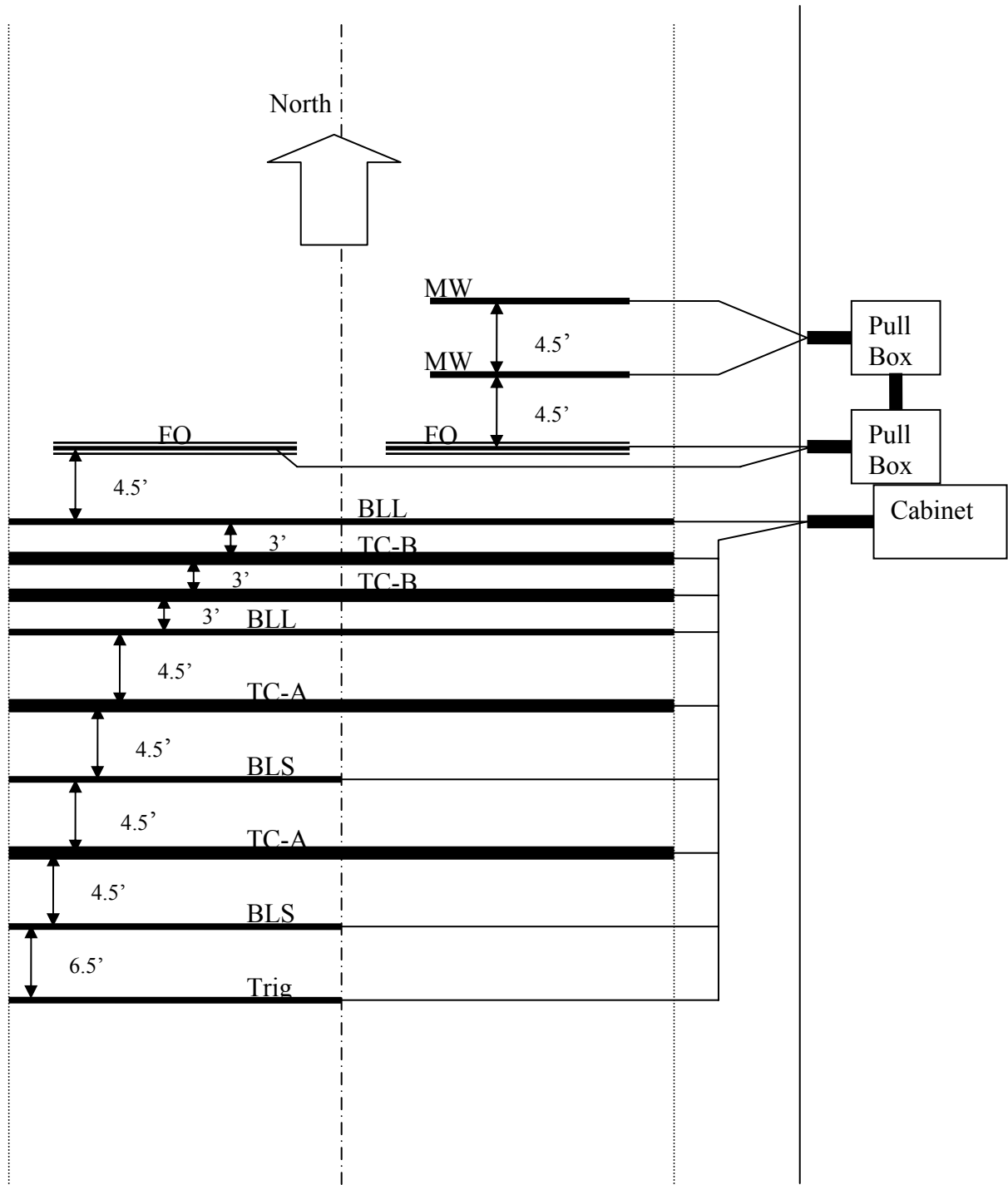


Figure 3-11: Layout of Sensor Installation.

The sensor installation layout is shown in [Figure 3-11](#). The meanings of the installed sensor abbreviated names are as follow:

- Trig: Trigger sensor using the same sensor as BLS;
- BLS: 6' bare piezoelectric sensor manufactured by Measurement Specialties, Inc.;
- BLL: 12' bare piezoelectric sensor manufactured by Measurement Specialties, Inc.;
- TC-A: 12' encapsulated piezoelectric sensor manufactured by Thermocoax, Inc.;
- TC-B: 12' encapsulated piezoelectric sensor manufactured by ECM, Inc.;
- FO: Fiber optic sensor developed by the University of Houston (UH) and IFOS;
and
- MW: Microwave sensor developed by UH.

CHAPTER 4: PIEZOELECTRIC SENSOR CONFORMITY AND UNIFORMITY TEST

4.1 Lab Test of Conformity and Uniformity

In load measurement systems, there are two important considerations for selecting the type of sensor. Not only the performance of these WIM sensors but also the costs have to be considered when designing a WIM system. The parameters associated with the performance of a sensor usually include conformity, uniformity, linearity and sensitivity, etc. All of them can affect the measurement results. Usually, specifications for sensors have enough published information to allow an informed selection. However, some manufacturers do not address difficulties or expense in replacing sensors in a permanent installation. Therefore, some measurements are required to insure proper functionality of the sensor before installation.

Since wheel tracking of vehicles on the WIM sensor varies with each pass, getting the same response from axles of the same load requires good uniformity along the sensor. Otherwise, a calibration coefficient (a function of the wheel position on the sensor) is needed. This requires an extra sensor for position measurement. Furthermore, the conformity, another important parameter of the sensor, has to be evaluated before the test of uniformity. Conformity is used to evaluate the stability or repeatability of a sensor's response. The same response is expected when the same load is applied on the same position along the sensor. To evaluate conformity and uniformity, an experiment was designed, using a piezoelectric sensor in a lab setting. Since piezoelectric sensors are only sensitive to dynamic load, the falling weight method was developed to conduct the test; the test equipment is shown in [Figure 4-1](#). The distance from the falling weight to the sensor under test is about 5 ft. In order to mount the sensor and protect it from damage, the sensor is covered with asphalt tape, and the falling weight used was limited to not more than 10 pounds.

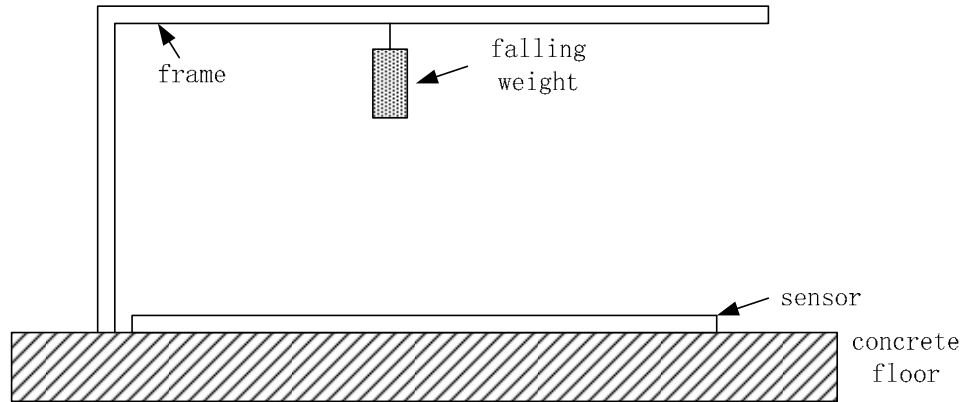


Figure 4-1: Falling Weight Test.

The sensor evaluated was one non-encapsulated 12-ft long piezoelectric sensor manufactured by Measurement Specialties, Inc. Along the sensor are six test points distributed evenly, and there are ten falling weight tests conducted at each point. The test began at the sensor's end furthest from the end of the connection cable. Test data are recorded by a data acquisition card with a 4-kHz sampling rate. The peak value of the response signal is used for conformity and uniformity analysis.

Obviously, there are two peaks in the test, as shown in [Figure 4-2](#): one has large amplitude and the other is much smaller. The large one is recorded for analysis, and the small one is discarded, since it is the result of the bounce of the falling weight.

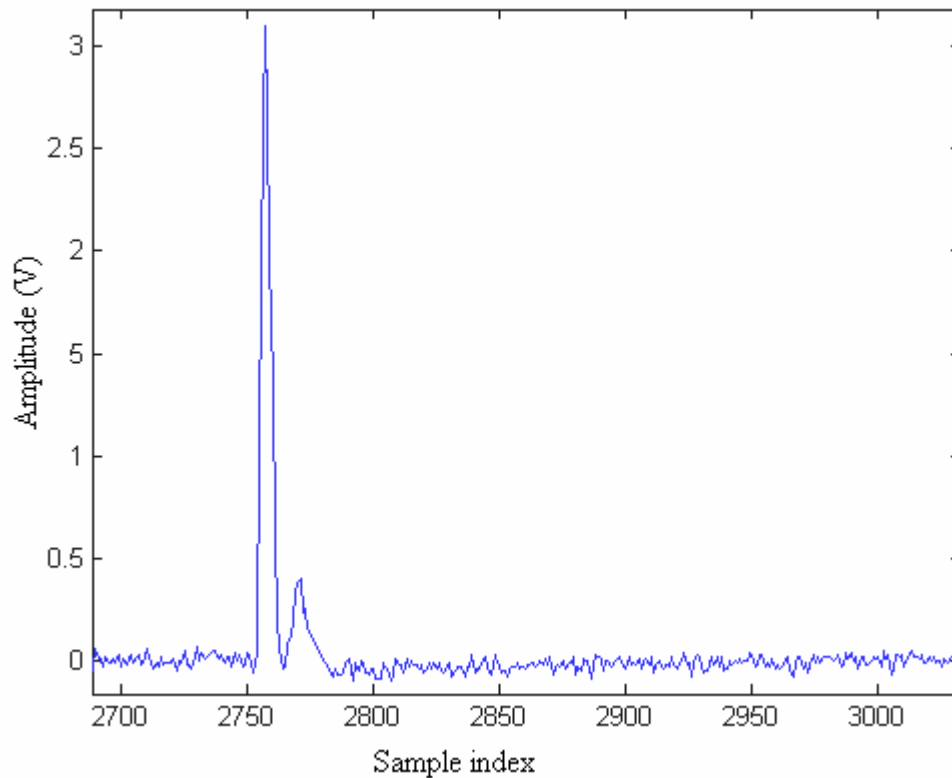


Figure 4-2: An Example of One Falling Weight Test Data.

In [Figure 4-3](#), the first test has the largest peak value. However, at the end of the test, it becomes much more stable with a smaller value. This is because the sensor is mounted with a piece of asphalt tape, which has room left for the sensor to move at the beginning of the test. After a few drops of the falling weight, the sensor will stay at a relatively stable position, which results in a stable amplitude. Test results at the six test points are shown in [Figures 4-3 to 4-9](#). The sensor shows good conformity at each test location. Although such a test cannot have an accurate result, it can be helpful to understand the sensor's characteristics.

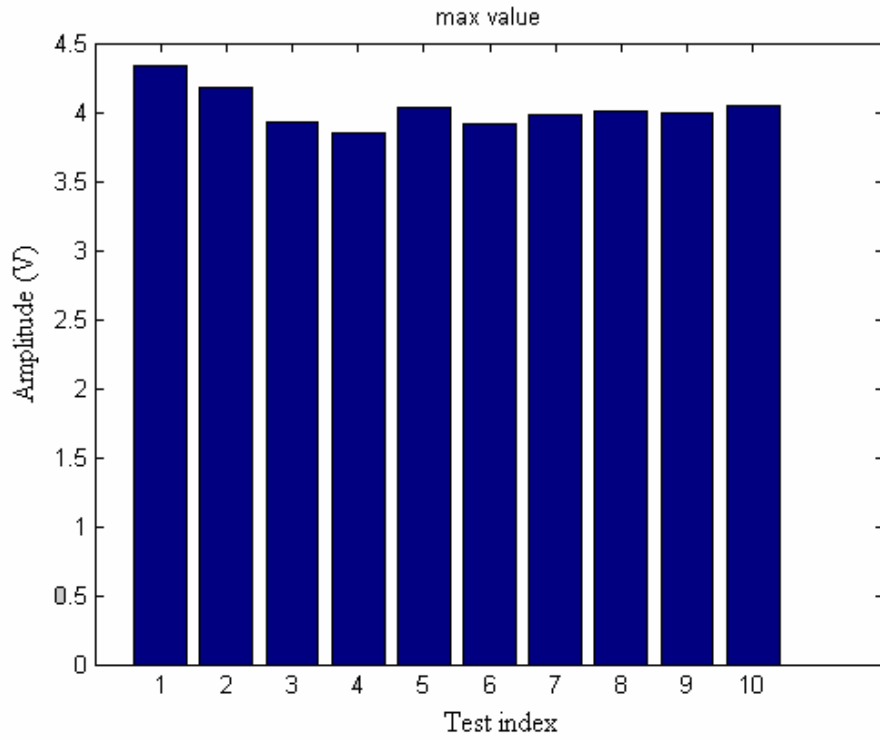


Figure 4-3: Conformity Test at Point 1.

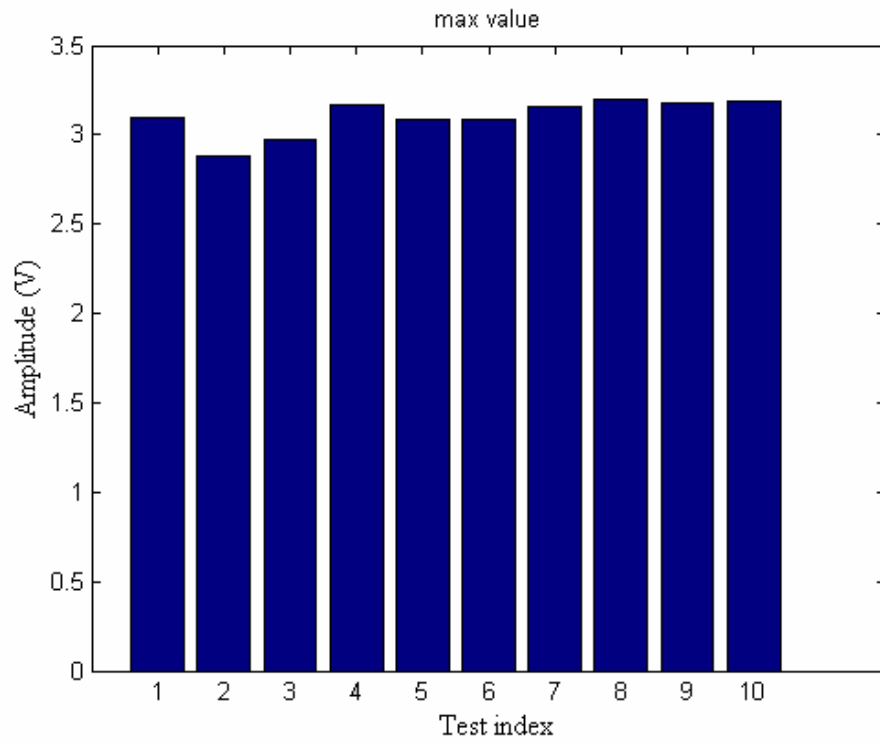


Figure 4-4: Conformity Test at Point 2.

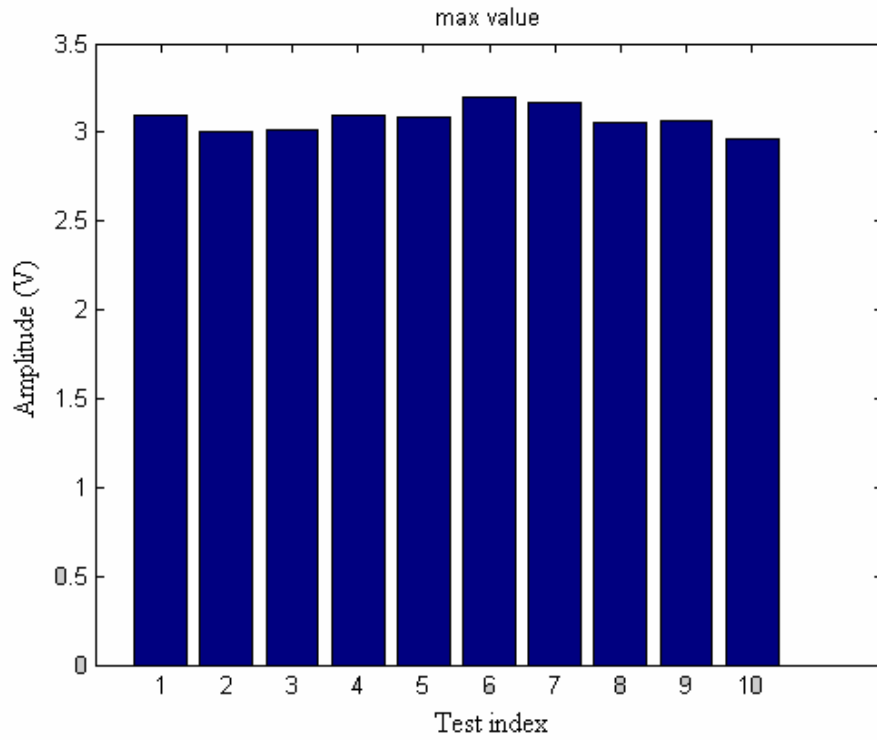


Figure 4-5: Conformity Test at Point 3.

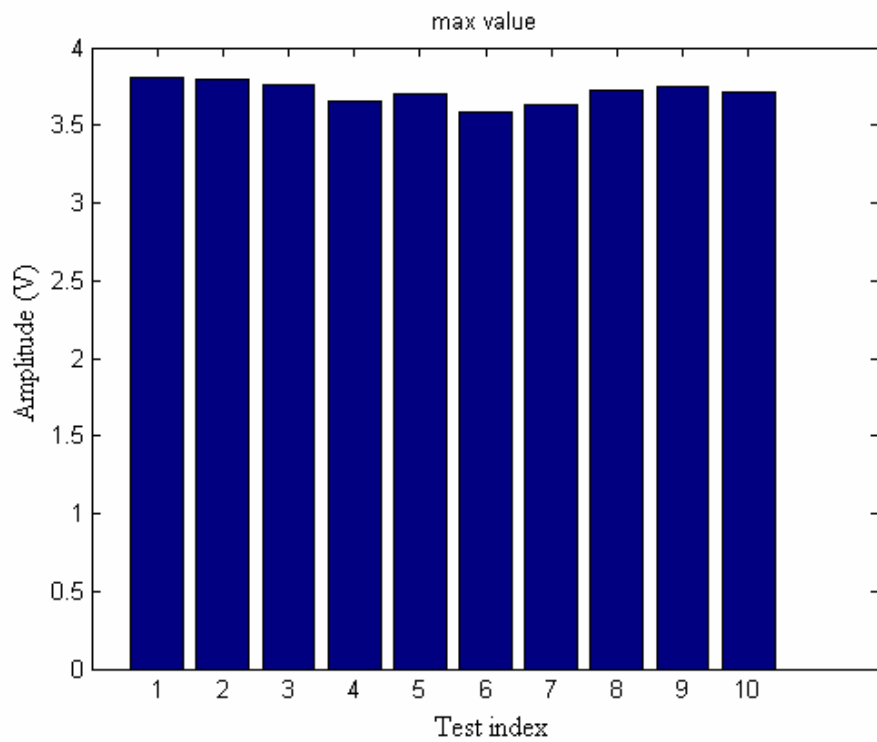


Figure 4-6: Conformity Test at Point 4.

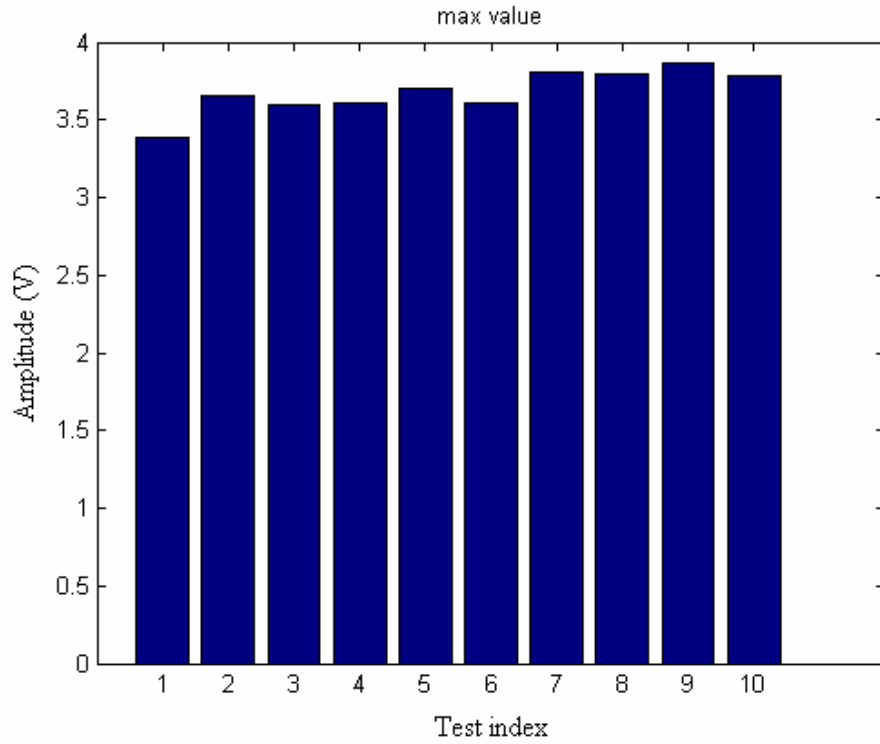


Figure 4-7: Conformity Test at Point 5.

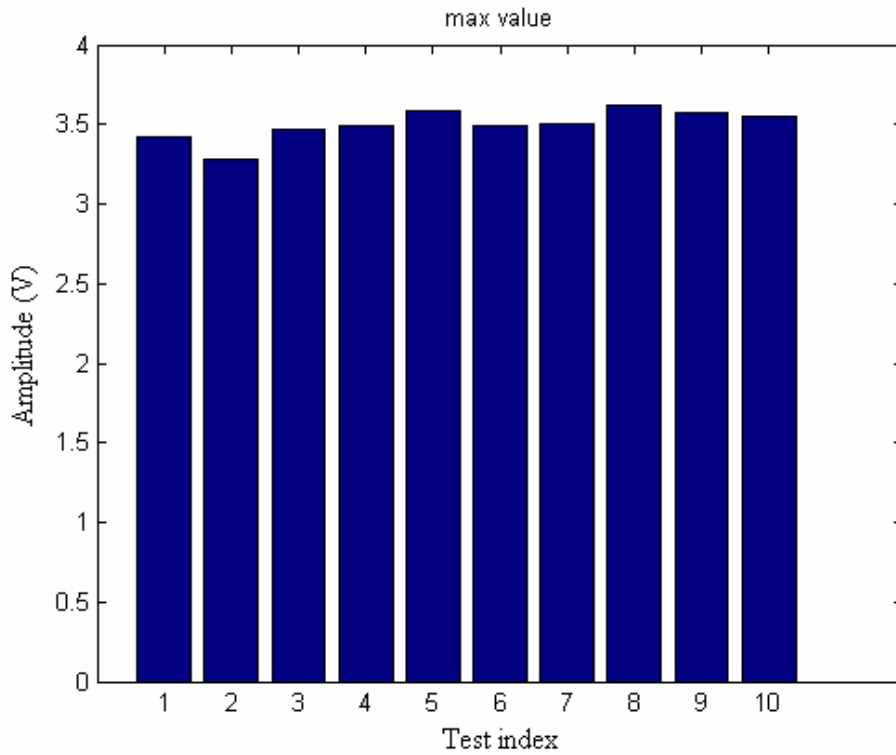


Figure 4-8: Conformity Test at Point 6.

Using the data from the conformity test, the uniformity can be estimated from these six test points. Assuming that the average amplitudes of 10 tests at one test point is the actual accurate response of this point, the result of uniformity is shown in [Figure 4-9](#). From the data of the sensor being evaluated, the uniformity is about 7% [21]. According to our test, the uniformity is a little larger than 7%, with test point 1 excluded from the data. Due to limitations of the test equipment used, it is a reasonable test result. Furthermore, after investigating the sensor's structure, it is clear that the one end of the sensor with a section sealed with thicker plastic resulted in bad mounting. This is the reason that error is introduced in test point 1. According to the installation manual, bending at the end of the sensor is required to improve the measurement uniformity.

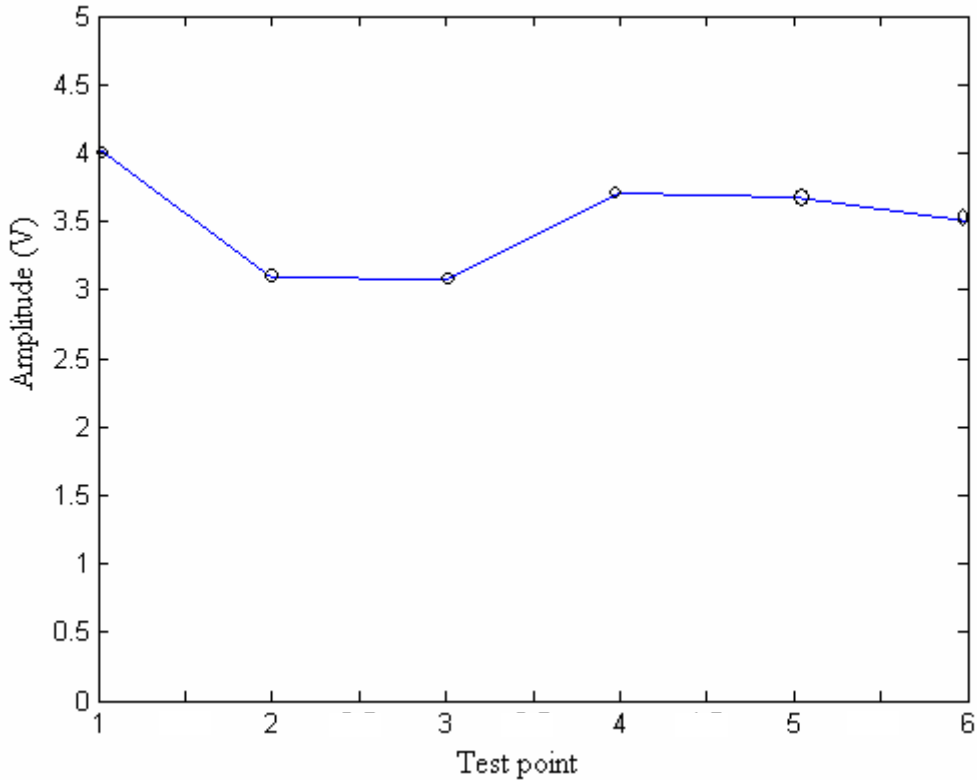


Figure 4-9: Result of Uniformity Test.

CHAPTER 5: INTEGRATION LOAD DETERMINATION ALGORITHM FOR PIEZOELECTRIC SENSOR AND FIELD TEST

5.1 Weight Determination and Data Processing

After the sensor installation, the amplifier and data acquisition system are connected to the sensors to enable data acquisition. To evaluate the installed piezoelectric sensors, typical five-axle trucks are chosen for their high density in the traffic stream. During the field test, the truck selected for monitoring passes through the WIM zone and then goes directly to the static scale. The data from the WIM sensors and the corresponding static load are recorded for data processing. The data acquisition has a sampling rate of about 18.1 ksps. This sampling rate is high enough to meet the recommended 100 samples for the period of the vehicle's crossing over the WIM sensor. Because of limited access to the facilities in this DPS site, limited data were acquired for the study.

5.1.1 Integration Load Determination Algorithm for Piezoelectric Sensor

After acquiring the data from the piezoelectric sensor, an algorithm for load determination is needed to make an estimation of static load. According to the sensor's specification by Measurement Specialties, Inc., it is best to make an integration of the axle-crossing waveform. The integral must be scaled to the vehicle's speed, as discussed in the piezoelectric sensor user's manual. The value is going to be proportional to the total load applied during the axle crossing [23]. Furthermore, to get a reasonable estimation of the vehicle's weight, 100 sample points during the crossing time are recommended. For the Kistler Instrument Inc. sensor, there is a more detailed algorithm for load determination. As shown in [Figure 5-1](#), a threshold level is used to define the integration range (from t_1 to t_2) [24].

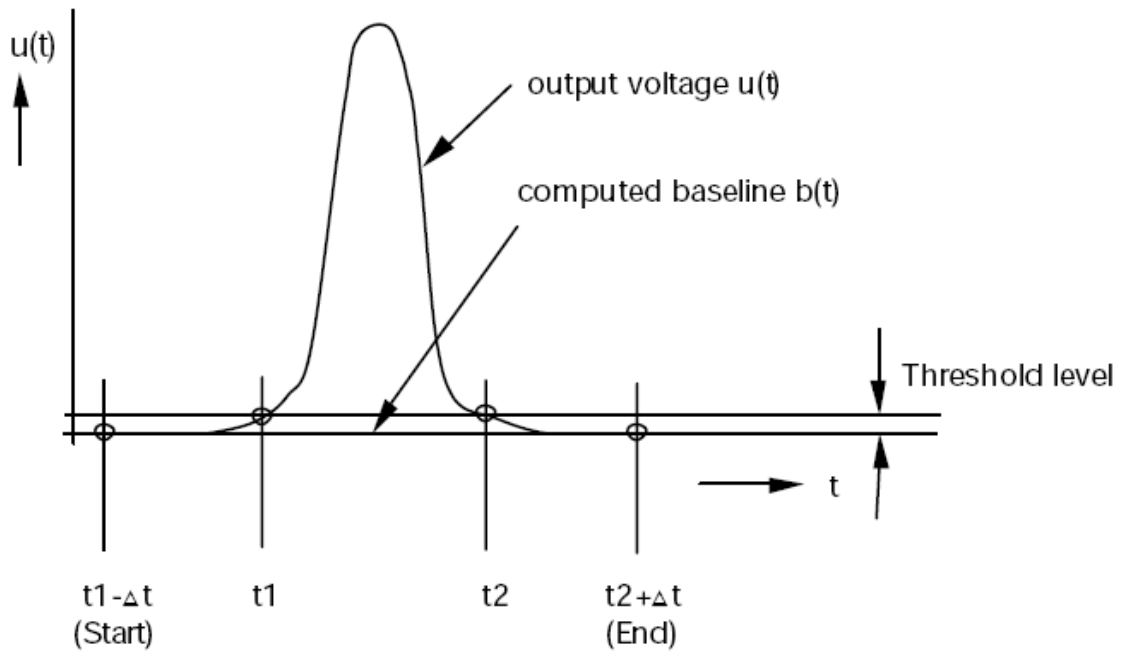


Figure 5-1: Integration Algorithm for Load Determination.

Source: Kistler Instrument Inc.

The corresponding wheel load is related to the area between the output voltage curve, $u(t)$, and the threshold level in addition to speed, as shown in [equation \(5-1\)](#).

$$W = \left(\frac{v}{L} \right) \times A \times C, \quad (5-1)$$

where W : Wheel load;

v : Vehicle speed;

A : Area between the output voltage curve $u(t)$ and the threshold level;

L : Sensor's width;

C : Calibration constant.

After sensor installation, the sensor's width, L , which is fixed, can be accounted into the calibration constant. The calibration constant is also fixed after conducting an initial calibration. Therefore, the parameters required in measuring axle load are vehicle speed, v , and area, A . Usually, from the output of two sensors installed with a known

distance between them, the vehicle speed can be calculated easily. The integration of the curve can be conducted as shown in [equation \(5-2\)](#).

$$A = \int [u(t) - b(t)], \text{ or } A = \sum [u_i - b_i] \text{ (in digital form),} \quad (5-2)$$

where $u(t)$ and $b(t)$ are shown in [Figure 5-1](#).

5.1.2 Data Processing

Although the theory behind the algorithm used for load determination is presented by WIM application companies in their product documentation, no further detail is given. According to the data acquired from several piezoelectric sensors, some facts are found to be very important when considering the algorithm for load determination. A detailed algorithm is developed in this discussion and proven to be effective.

From the field data of a piezoelectric sensor of a typical five-axle truck, as shown in [Figure 5-2](#), a dropdown of the signal's amplitude prior to the axle's arrival at the sensor is found to be significant. The algorithm using a threshold will exclude a large area of pulse (corresponding to the axle's load) beneath the threshold. The excluded part, in fact, is also part of the axle's response. The dropdown is induced by the pavement's deflection which starts being detected before the axle's arrival at the sensor. Therefore, if the pulse range for integration can be decided correctly, the corresponding integration can be conducted easily. A derivative method is introduced to define the range of the pulse. Comparing the curves of the signal and its derivative, as shown in [Figure 5-3](#), there is one positive peak and one negative peak in the derivative curve corresponding to each pulse in the signal induced by one axle load. The starting and ending point for one pulse are defined as the points nearest to the pulse where the derivative equals to zero. The corresponding amplitude value at the starting point is used as the baseline for the pulse. The result of the integration (the area between the pulse and baseline) is the value used for load determination.

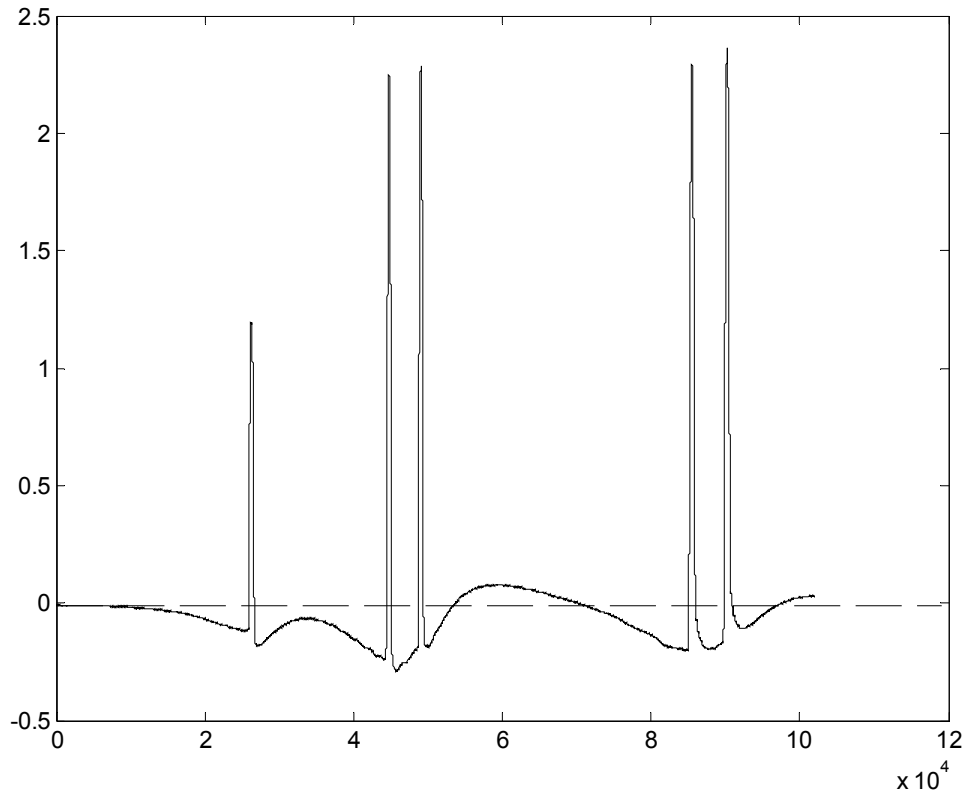


Figure 5-2: An Example of Field Data.

Because of the relationship between speed and pulse area, the speed factor should be considered in the load determination algorithm. When the speed limit inside the WIM zone is 15 MPH, the speed factor is normalized to 15 MPH. The equation can be simplified as

$$W = f\left(\left(\frac{v}{15}\right) \times A\right), \quad (5-3)$$

where W : Wheel load;

v : Vehicle speed (unit in MPH);

A : Area between the output voltage curve $u(t)$ and the threshold level;

$f(*)$: Calibration function of v and A .

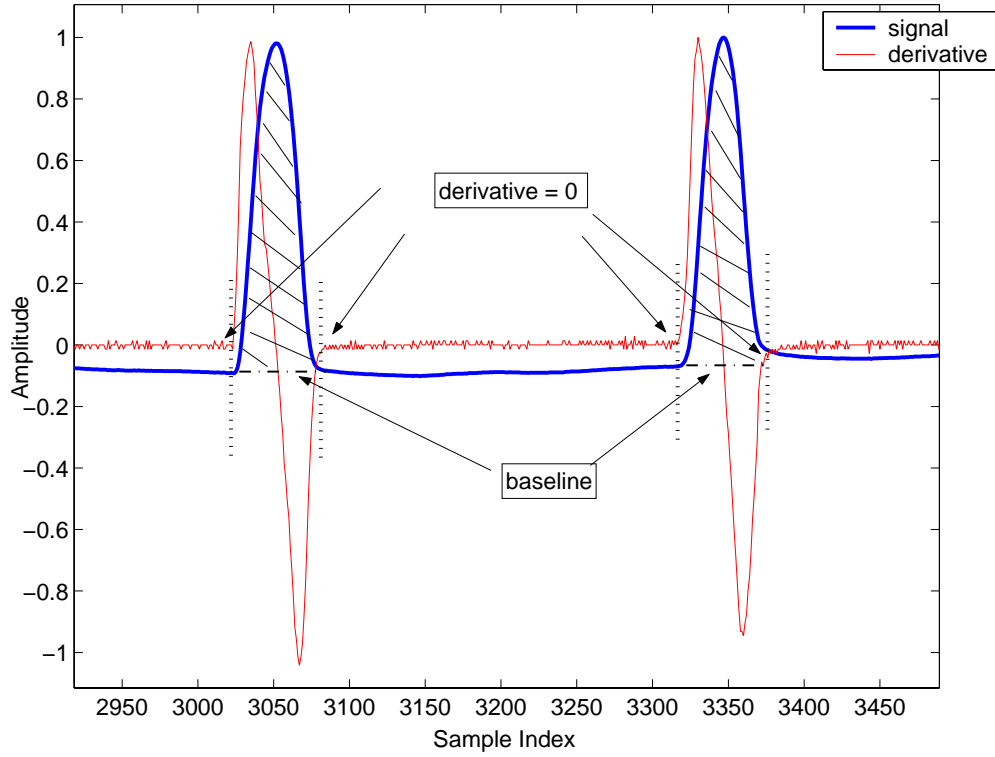


Figure 5-3: Method of Pulse Range Detection.

With the equations set up, an algorithm is implemented in the WIM software by a program. The corresponding flowchart is shown in [Figure 5-4](#).

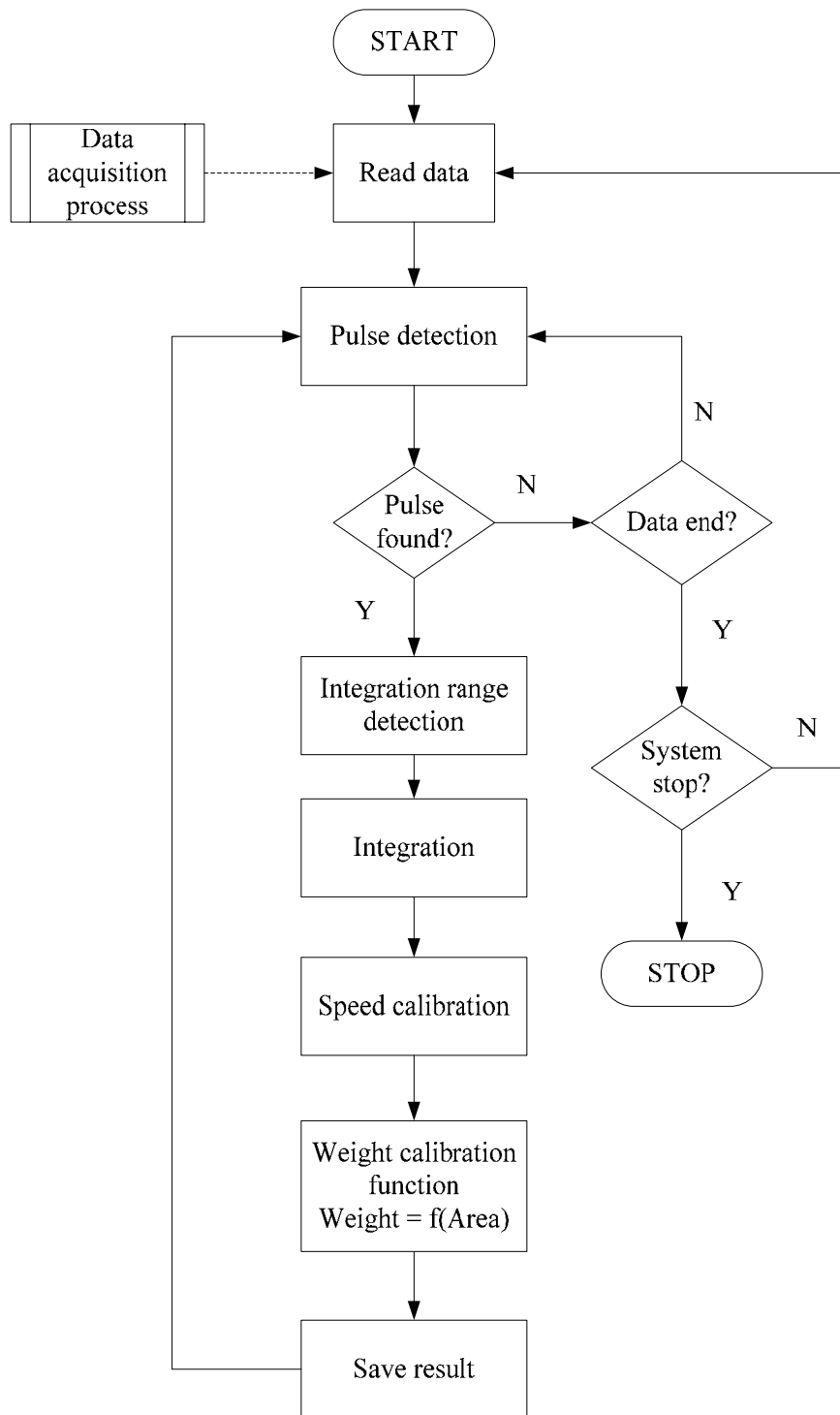


Figure 5-4: Flowchart of Integration Load Determination Algorithm.

5.2 Field Test Data and Results

After sensor installation, the field test was conducted to evaluate the piezoelectric sensors. As shown in [Table 5-1](#), there are 50 groups of test data acquired; one group's data was unusable with load data entered as -1. According to the data, it is easy to see that the trucks have steering axle loads so stable that it can even be used as the calibration load for the WIM system's self calibration [\[25\]](#). Therefore, to simplify data analysis, only the drive axle and trailer axle are considered in our discussion. When investigating the acquired data from different sensors, the TC-A.1 and TC-A.2 sensor's output are found to be distorted. The positive pulse is affected too much by the pavement deflection (longitude wave in horizontal direction). So, in our discussion, the TC-A.1 and TC-A.2 sensor outputs are not included.

In our discussion, drive axle load and trailer axle load are used for comparison of sensor results. Then the average of the two sensors is also tested to improve the measurement accuracy. In the data analysis, the x axis label, "area", means the value of pulse integration with speed calibration. A curve fitted to the speed calibrated data results in a load calibration function. The corresponding error is calculated based on this calibration function.

Table 5-1: Static load in field test

Test Index	Steering Axle Static load (lb.)	Drive Axle Group Static load(LB.)	Trailer Axle Group Static load (lb.)
1	10,600	29,300	20,480
2	10,980	31,920	26,480
3	11,620	22,780	21,100
4	10,800	13,960	10,340
5	9,500	13,220	11,920
6	10,660	27,240	11,960
7	11,300	34,040	34,120
8	10,980	14,300	12,300
9	11,920	30,740	33,260
10	10,600	33,020	34,020
11	11,420	15,040	15,240
12	10,480	33,620	33,500
13	10,120	33,140	29,860
14	10,160	29,260	24,260
15	10,740	11,840	10,260
16	10,900	33,200	32,300
17	9,680	24,440	28,140
18	11,540	33,420	33,820
19	9,920	15,000	11,520
20	11,080	18,640	17,340
21	10,340	32,180	33,740
22	9,540	20,600	17,440
23	10,380	12,400	8,740
24	10,240	26,320	23,300
25	11,280	30,420	33,720
26	9,820	11,860	10,320
27	11,400	34,500	34,700
28	11,800	33,380	28,600

Test Index	Steering Axle Static load (lb.)	Drive Axle Group Static load(LB.)	Trailer Axle Group Static load (lb.)
29	11,200	29,660	20,880
30	12,000	31,700	33,040
31	11,140	17,060	14,400
32	11,100	19,240	15,440
33	10,800	31,520	32,700
34	11,060	32,340	32,780
35	9,840	22,400	17,040
36	10,580	15,740	16,160
37	10,660	21,960	19,960
38	11,220	13,620	10,260
39	11,720	33,420	33,260
40	9,680	15,620	11,140
41	11,180	22,100	30,760
42	11,380	30,840	34,160
43	9,820	13,260	9,940
44	10,460	32,260	33,060
45	11,060	31,960	30,860
46	9,540	16,800	18,940
47	10,260	18,120	13,040
48	-1	-1	-1
49	11,300	33,600	32,440
50	10,700	13,040	12,000

5.2.1 Test Results of BLS.1 Sensor

Test Result of BLS.1 Sensor on Drive Axle

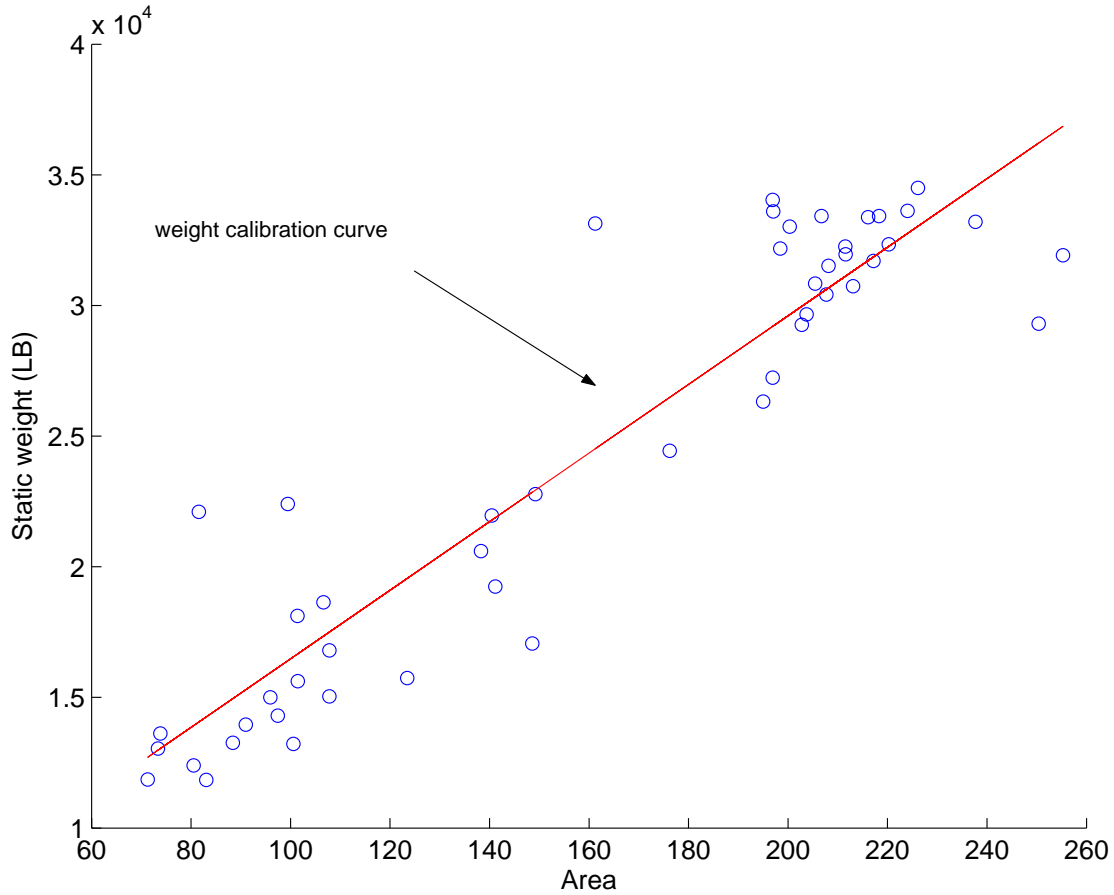


Figure 5-5: Load Calibration Function ($y = 131.3x + 3351.1$) for BLS.1 on Drive Axle.

According to the distribution of area value versus static load, a function, $y = 131.3x + 3351.1$, is found by linear curve fitting to be the calibration function for the BLS.1 sensor in Figure 5-5. The measured loads (WIM loads) versus static loads by using this calibration function are shown in Figure 5-6. The accuracy of this measurement is shown in Figure 5-7 for different loads. Furthermore, based on the accuracy and precision definition of WIM measurement previously discussed, the probability density function, a normal distribution function, can be derived and is plotted in Figure 5-8. The mean value is the description for accuracy and the variance for precision. The nearer to zero the mean

value approaches, the more accurate the system becomes. Therefore, this probability density function will be used for the performance comparison of sensors.

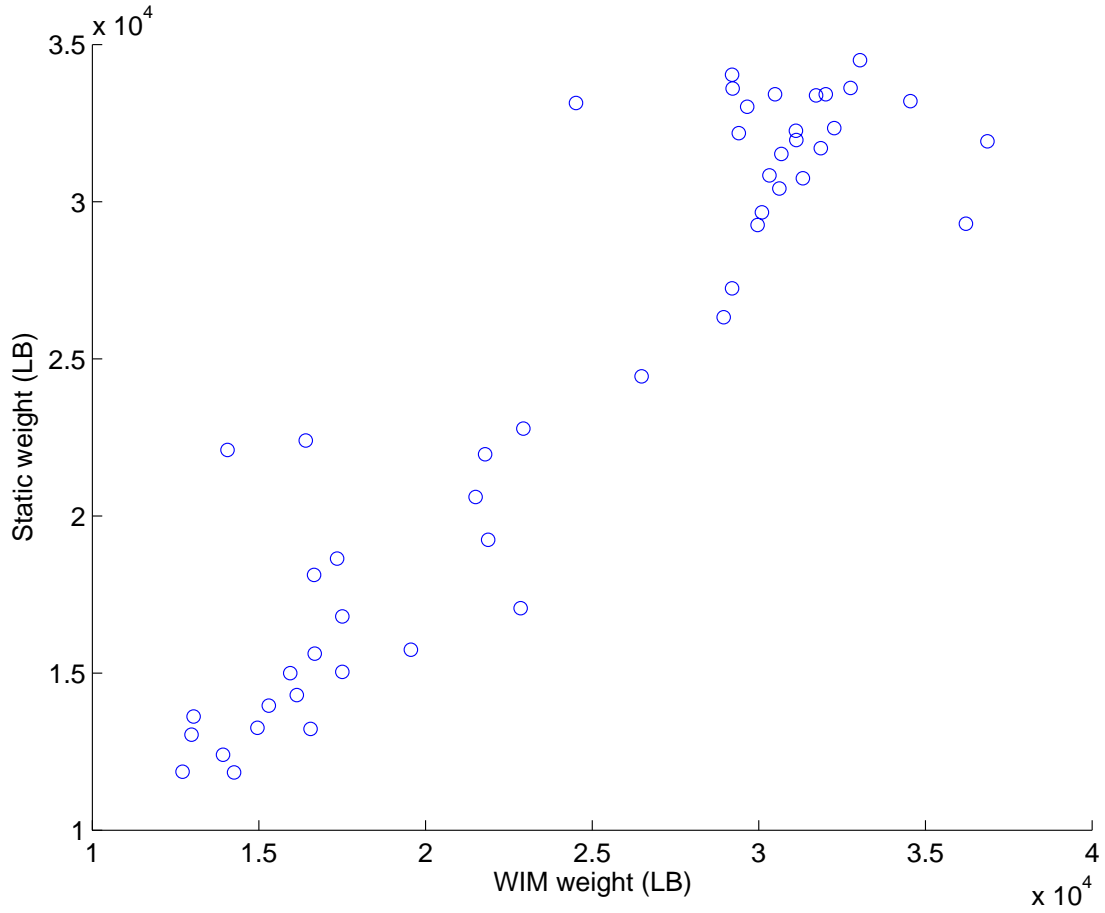


Figure 5-6: Static Load vs. WIM Load of BLS.1 on Drive Axle.

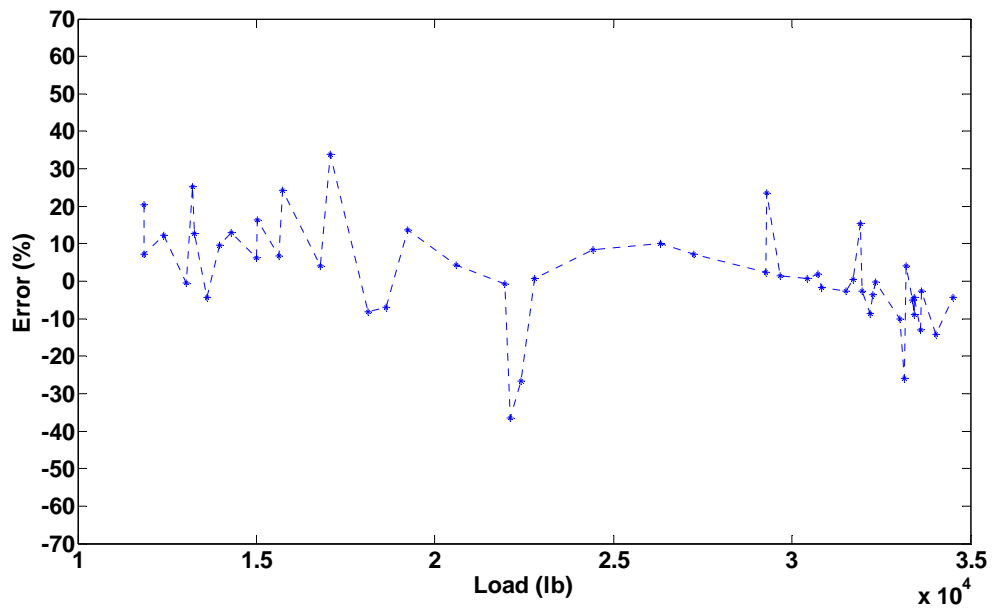


Figure 5-7: Error of Axle Load Measurement for BLS.1 on Drive Axle.

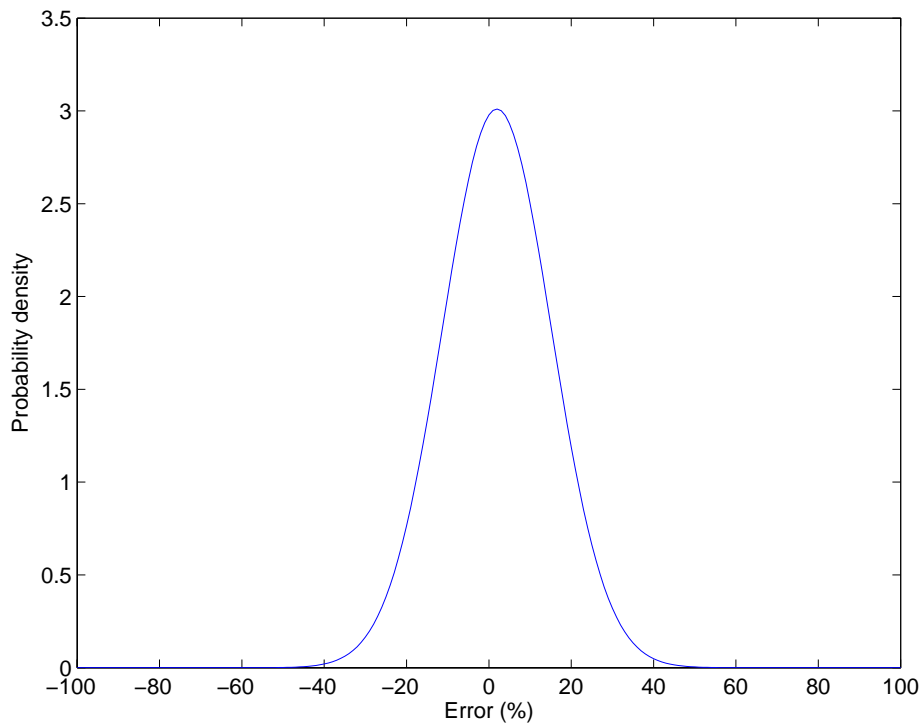


Figure 5-8: Probability Density Function ($\mu=1.94\%$, $\sigma=13.25\%$) for BLS.1 on Drive Axle.

Test Result of BLS.1 Sensor on Trailer Axle

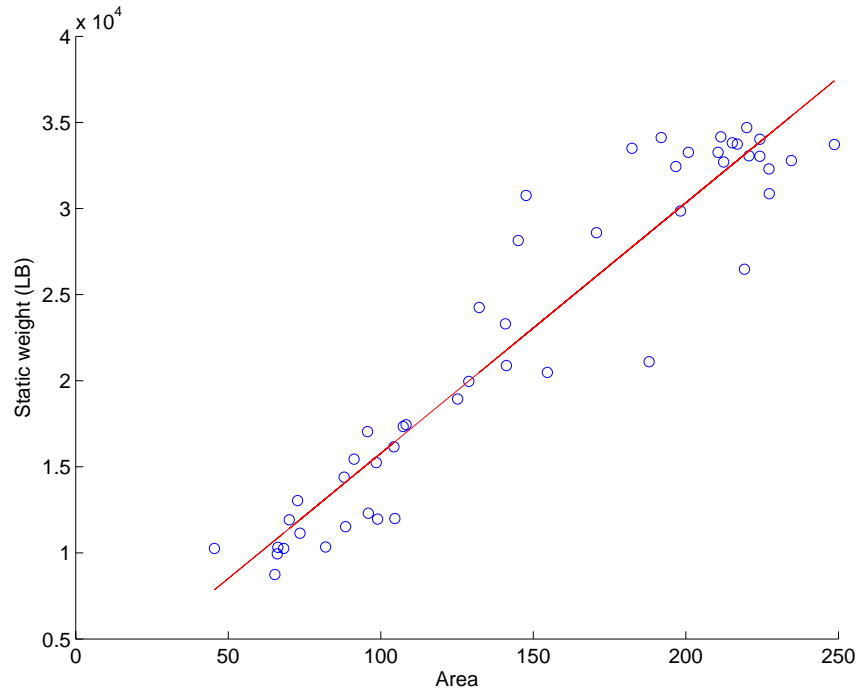


Figure 5-9: Load Calibration Function ($y = 145.5x + 1232$) for BLS.1 on Trailer Axle.

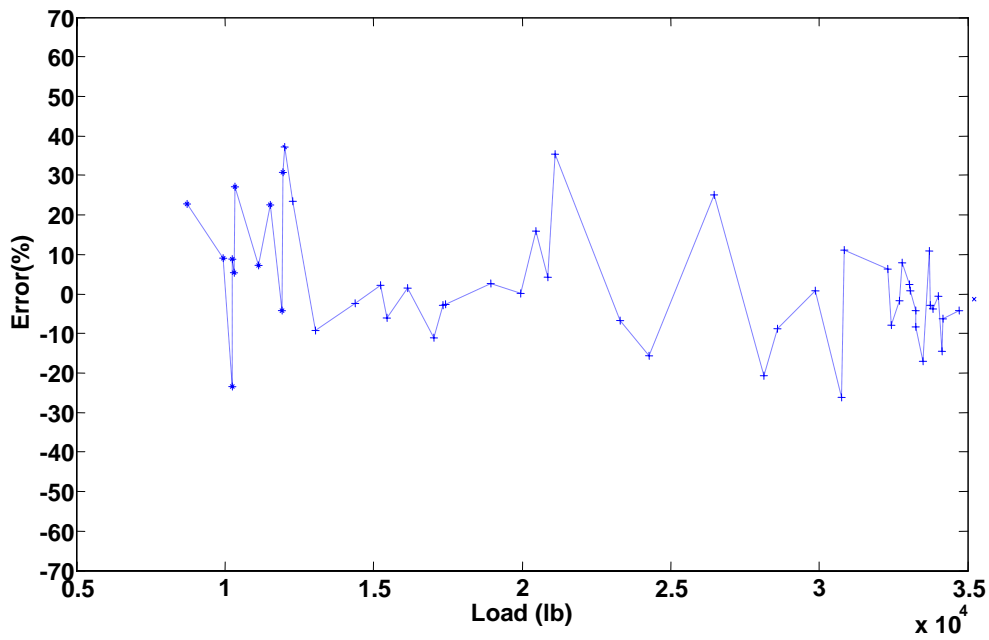


Figure 5-10: Error of Axle Load Measurement for BLS.1 on Trailer Axle.

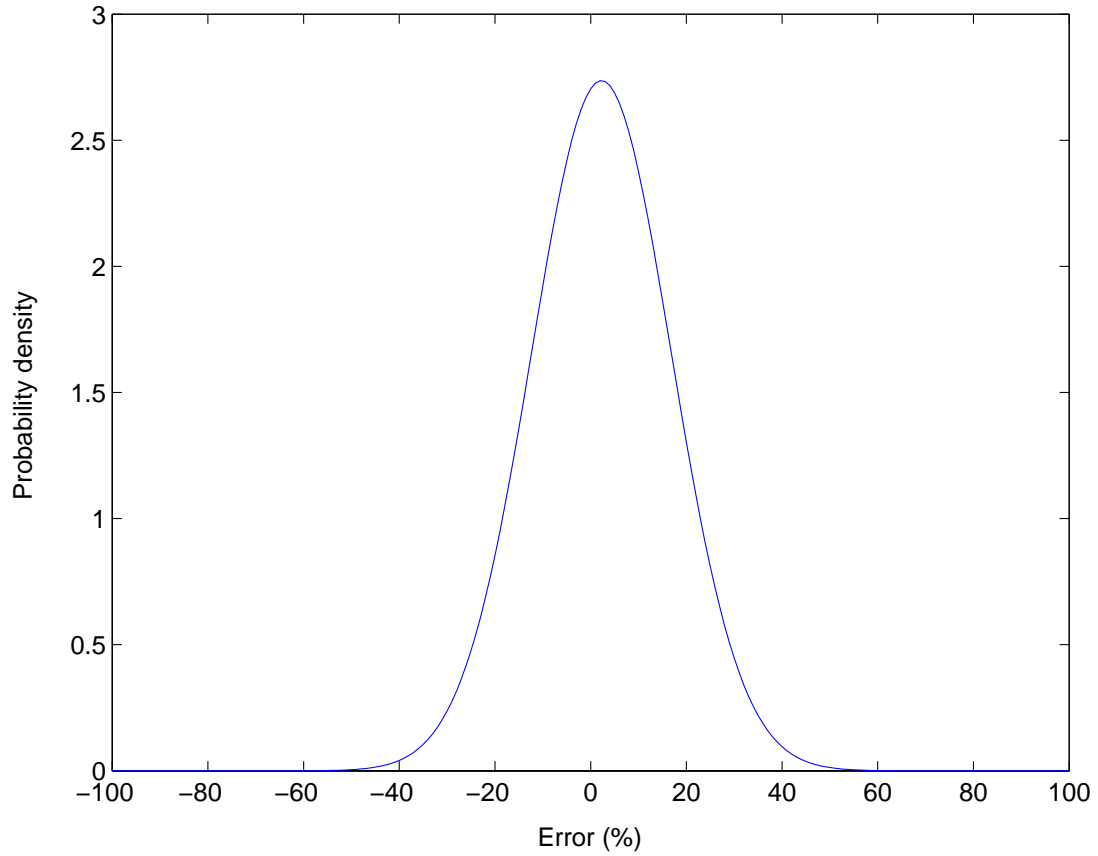


Figure 5-11: Probability Density Function ($\mu=2.25\%$, $\sigma=14.58\%$) for BLS.1 on Trailer Axle.

5.2.2 Test Results of BLS.2 Sensor

Test Result of BLS.2 Sensor on Drive Axle

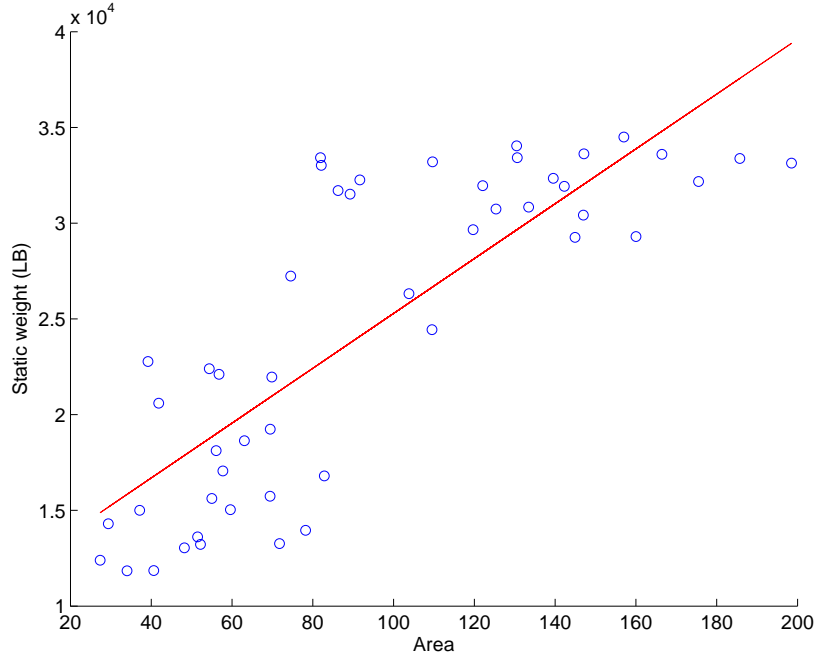


Figure 5-12: Load Calibration Function ($y = 143.2x + 10963.3$) for BLS.2 on Drive Axle.

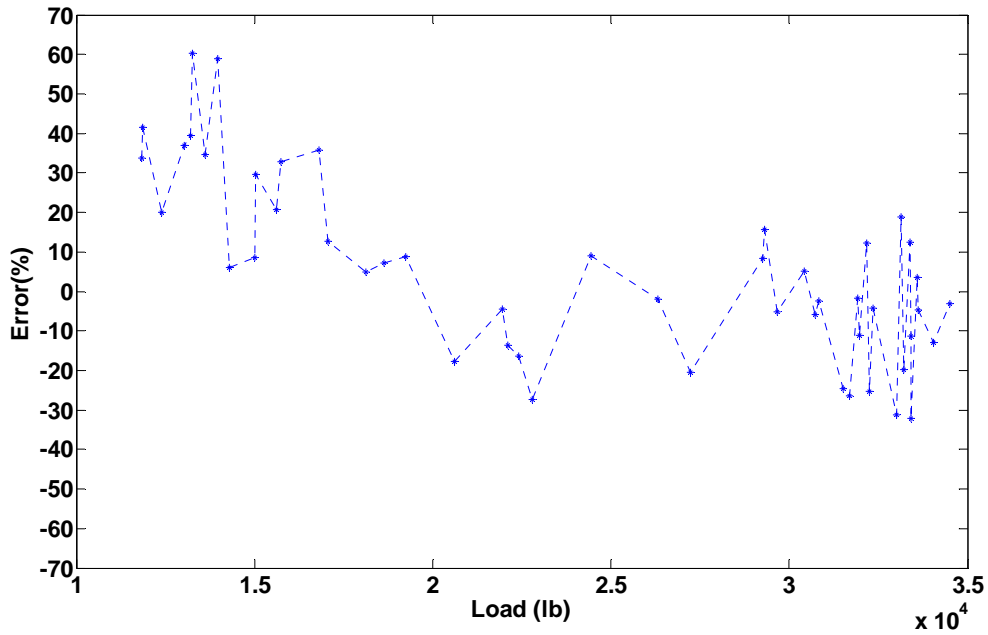


Figure 5-13: Error of Axle Load Measurement for BLS.2 on Drive Axle.

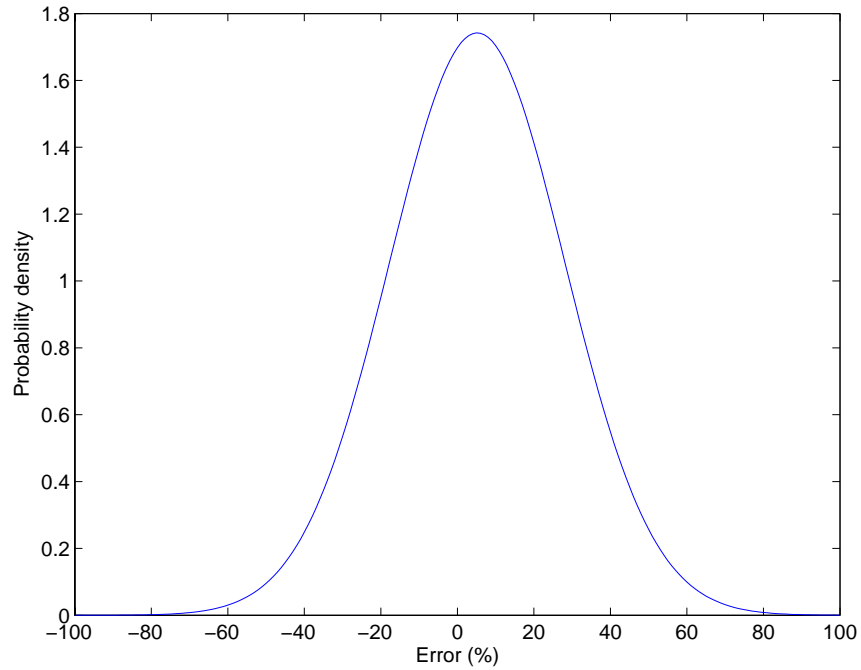


Figure 5-14: Probability Density Function ($\mu=5.19\%$, $\sigma=22.9\%$) for BLS.2 on Drive Axle.

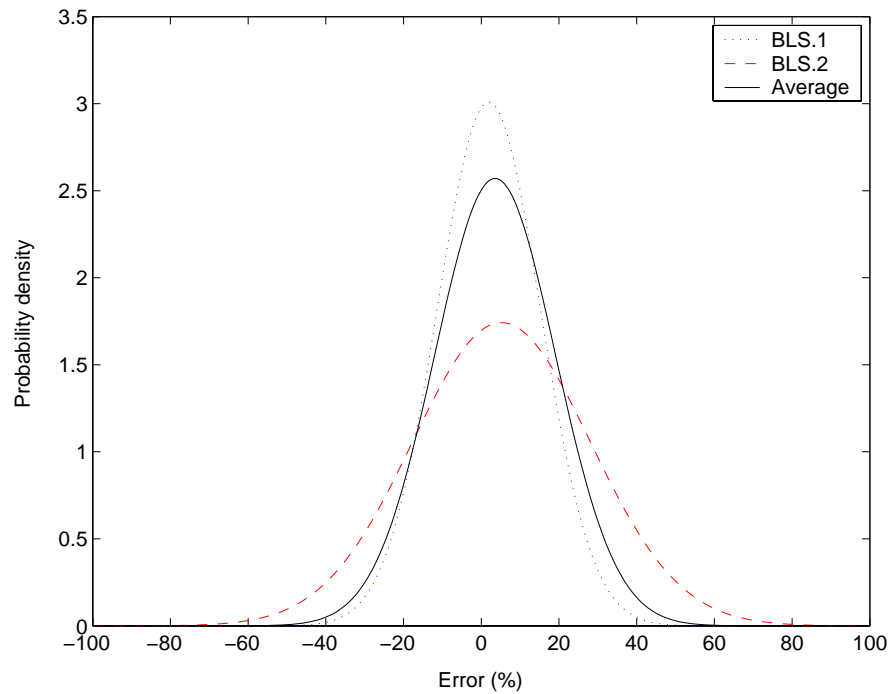


Figure 5-15: Probability Density Function ($\mu=3.56\%$, $\sigma=15.52\%$) for Average of BLS.1 and BLS.2 on Drive Axle.

Test Result of BLS.2 Sensor on Trailer Axle

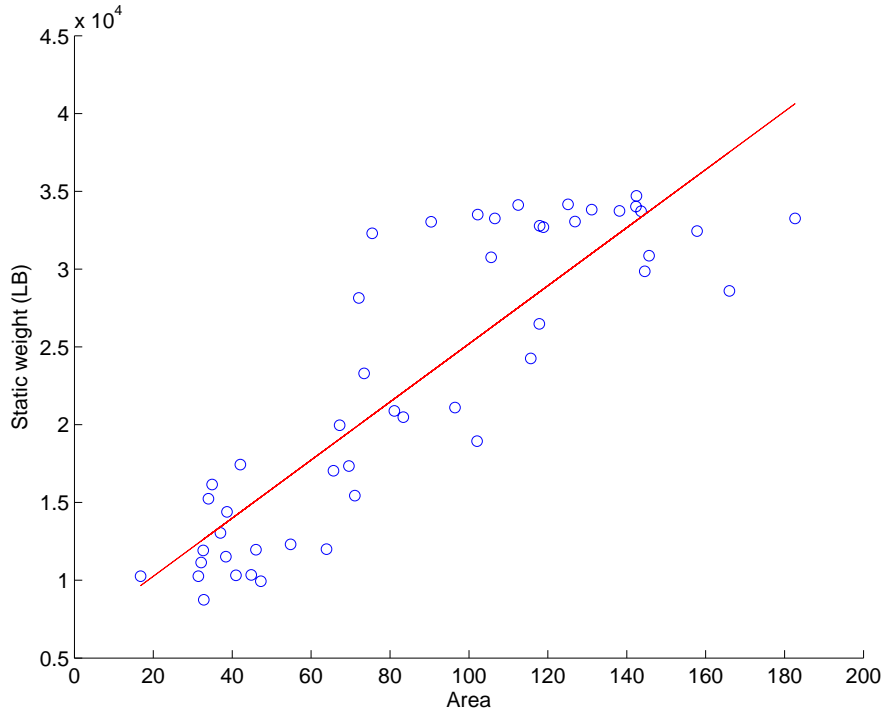


Figure 5-16: Load Calibration Function ($y = 186.7x + 6523.4$) for BLS.2 on Trailer Axle.

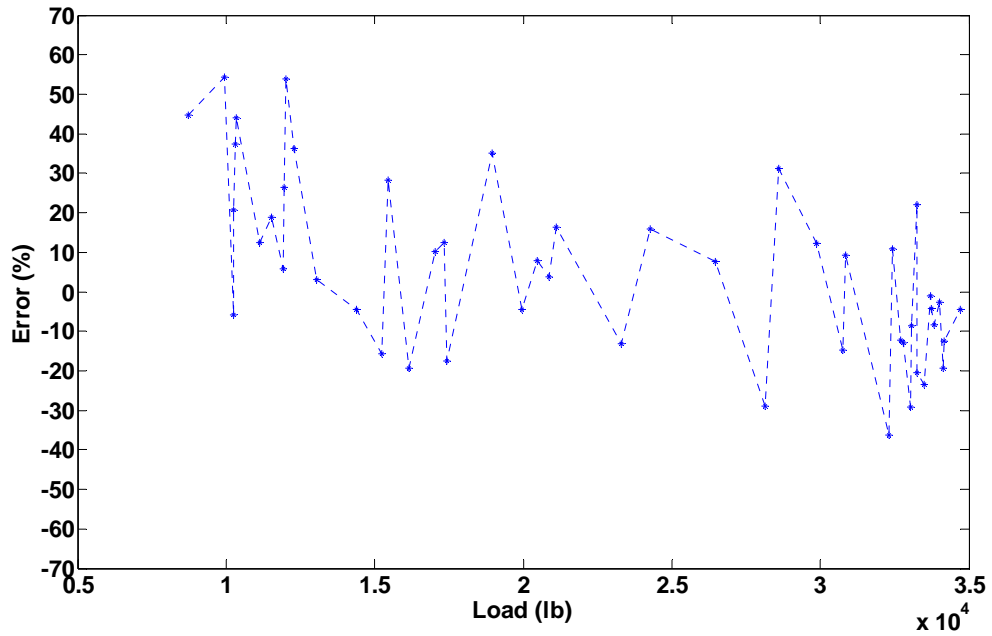


Figure 5-17: Error of Axle Load Measurement for BLS.2 on Trailer Axle.

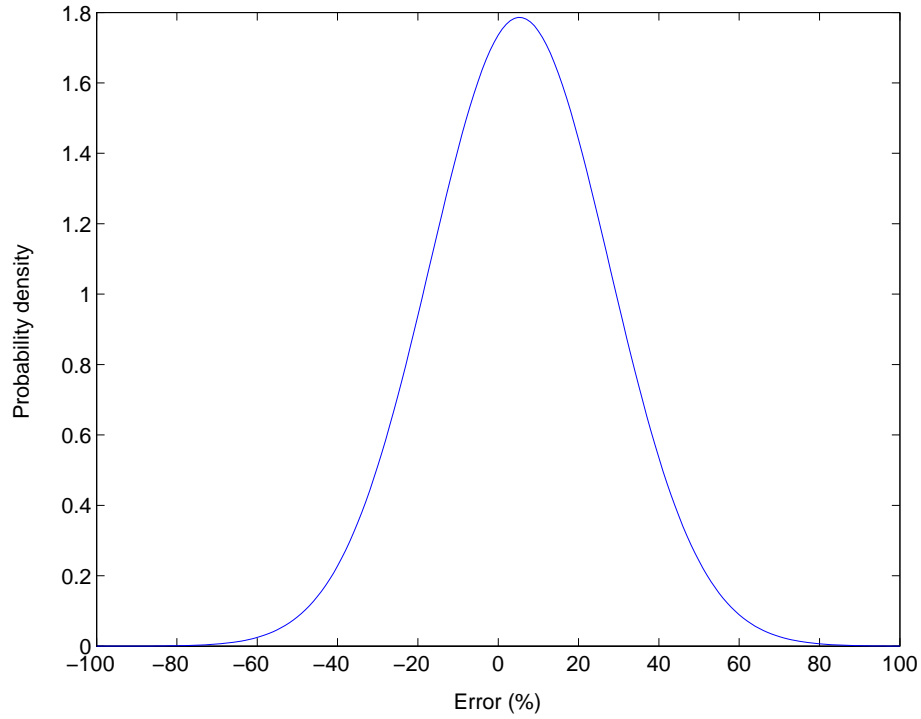


Figure 5-18: Probability Density Function ($\mu=5.33\%$, $\sigma=22.3\%$) for BLS.2 on Trailer Axle.

Table 5-2: Results of Test on BLS Sensors.

Sensor	Axle	Load Calibration Function	Accuracy Estimation	
			(μ , σ)	(μ , 1.96σ)
BLS.1	Drive Axle	$y = 131.3x + 3351.1$	(1.94%, 13.25%)	(1.94%, 25.97%)
	Trailer Axle	$y = 145.5x + 1232.0$	(2.25%, 14.58%)	(2.25%, 28.58%)
BLS.2	Drive Axle	$y = 143.2x + 10963.3$	(5.19%, 22.90%)	(5.19%, 44.88%)
	Trailer Axle	$y = 186.7x + 6523.4$	(5.33%, 22.30%)	(5.33%, 43.71%)

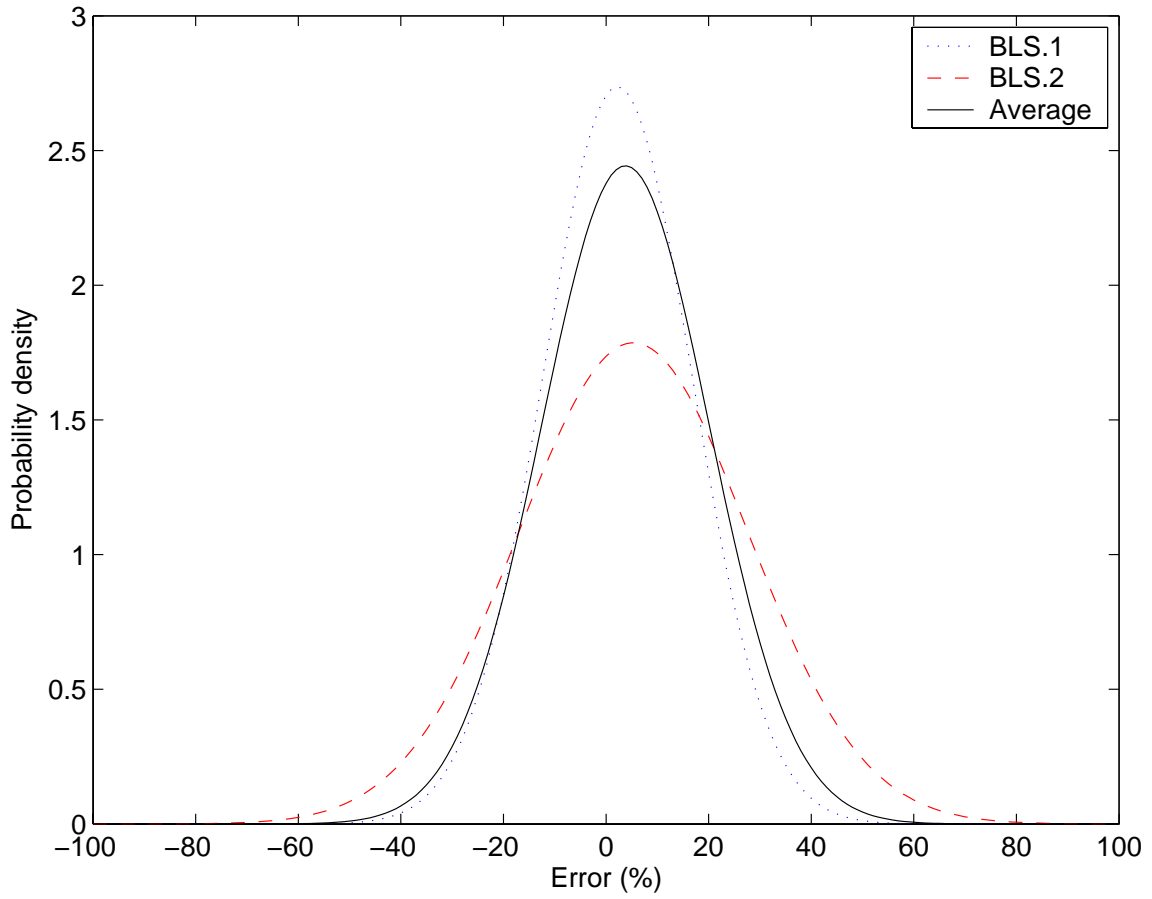


Figure 5-19: Probability Density Function ($\mu=3.79\%$, $\sigma=16.33\%$) for Average of BLS.1 and BLS.2 on Trailer Axle.

5.2.3 Test Results of BLL.1 Sensor

Test Result of BLL.1 Sensor on Drive Axle

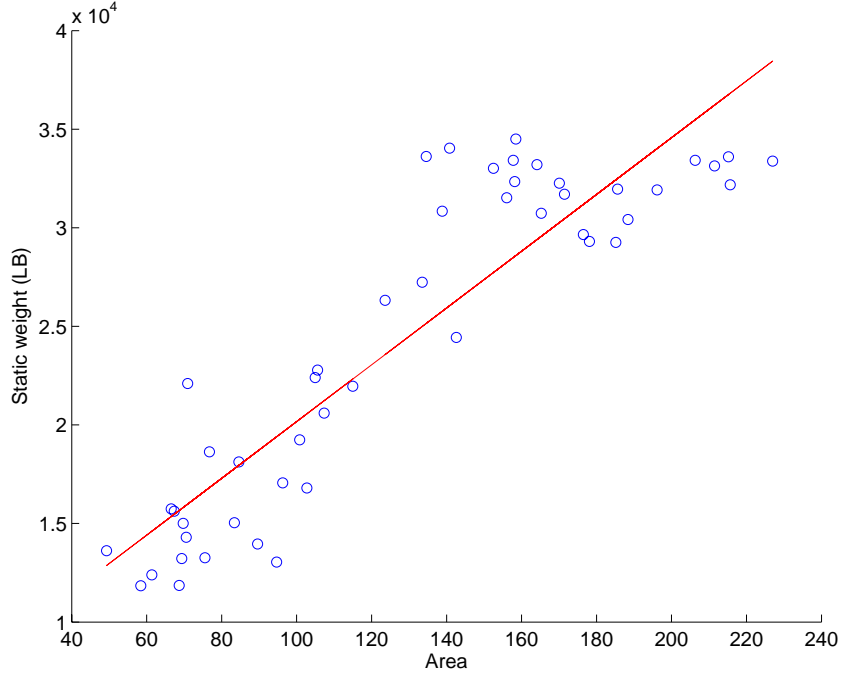


Figure 5-20: Load Calibration Function ($y = 144x + 5765$) for BLL.1 on Drive Axle.

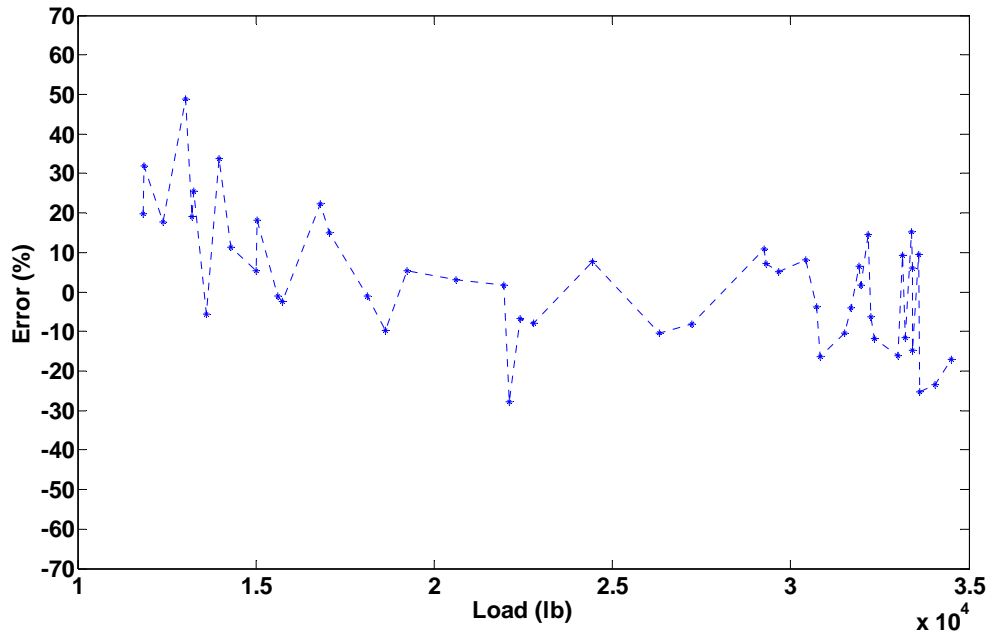


Figure 5-21: Error of Axle Load Measurement for BLL.1 on Drive Axle.

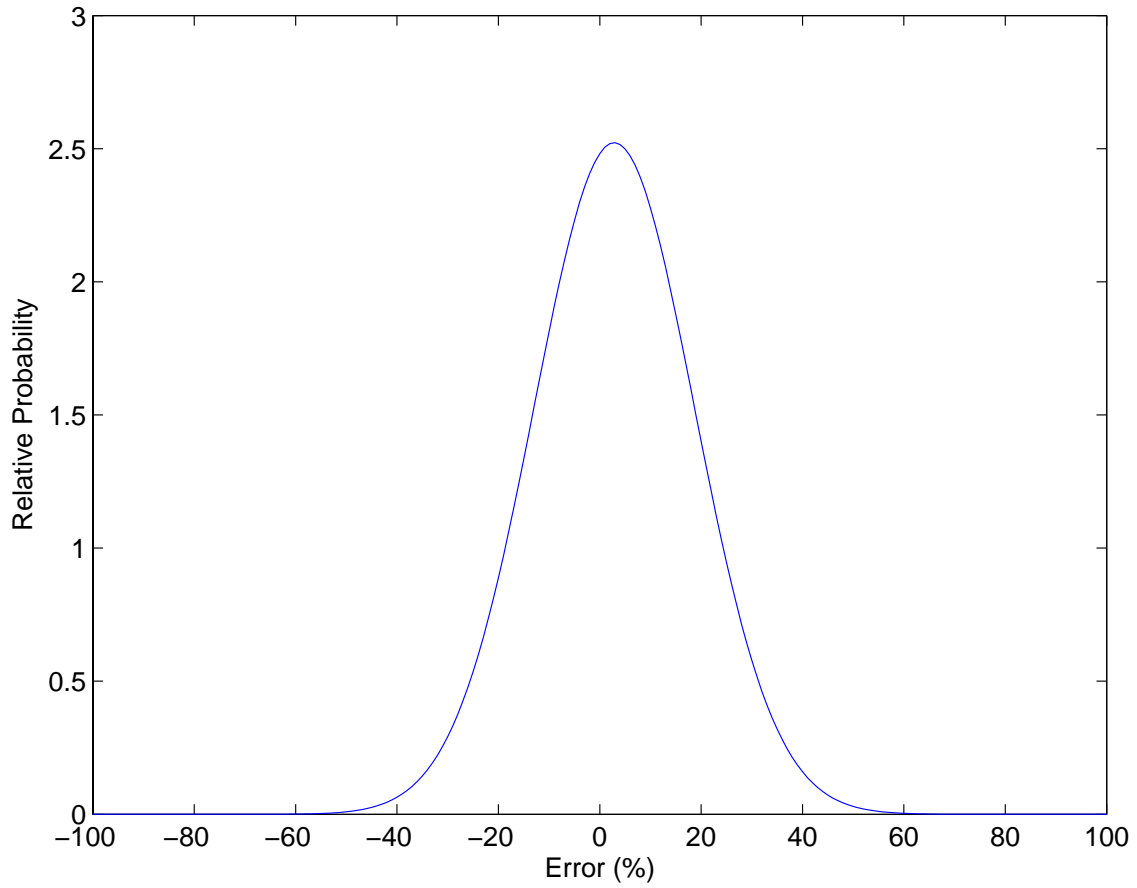


Figure 5-22: Probability Density Function ($\mu=2.85\%$, $\sigma=15.8\%$) for BLL.1 on Drive Axle.

Test Result of BLL.1 Sensor on Trailer Axle

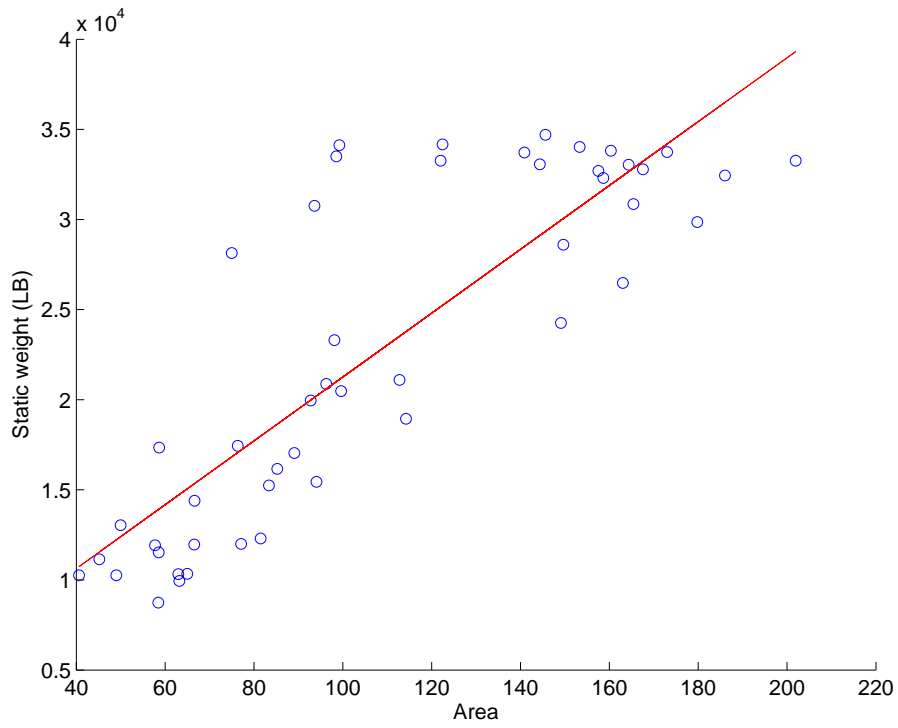


Figure 5-23: Load Calibration Function ($y = 177.15x + 3542.31$) for BLL.1 on Trailer Axle.

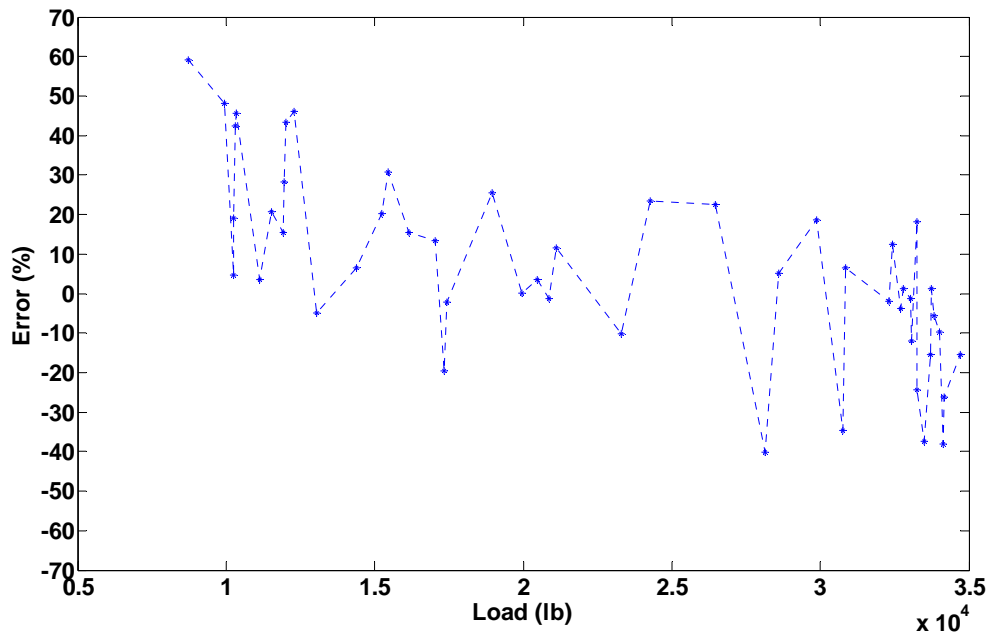


Figure 5-24: Error of Axle Load Measurement for BLL.1 on Trailer Axle.

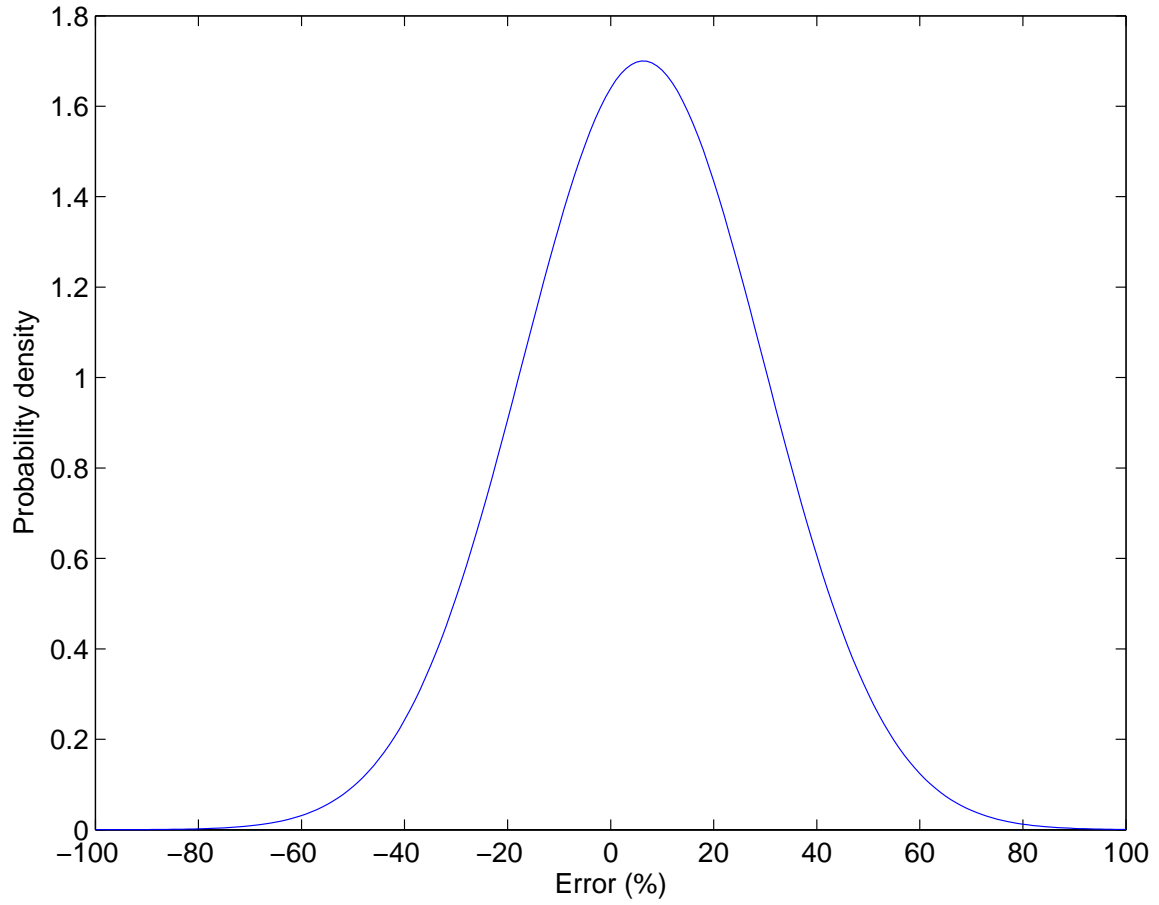


Figure 5-25: Probability Density Function ($\mu=6.31\%$, $\sigma=23.46\%$) for BLL.1 on Trailer Axle.

5.2.4 Test Results of BLL.2 Sensor

Test Result of BLL.2 Sensor on Drive Axle

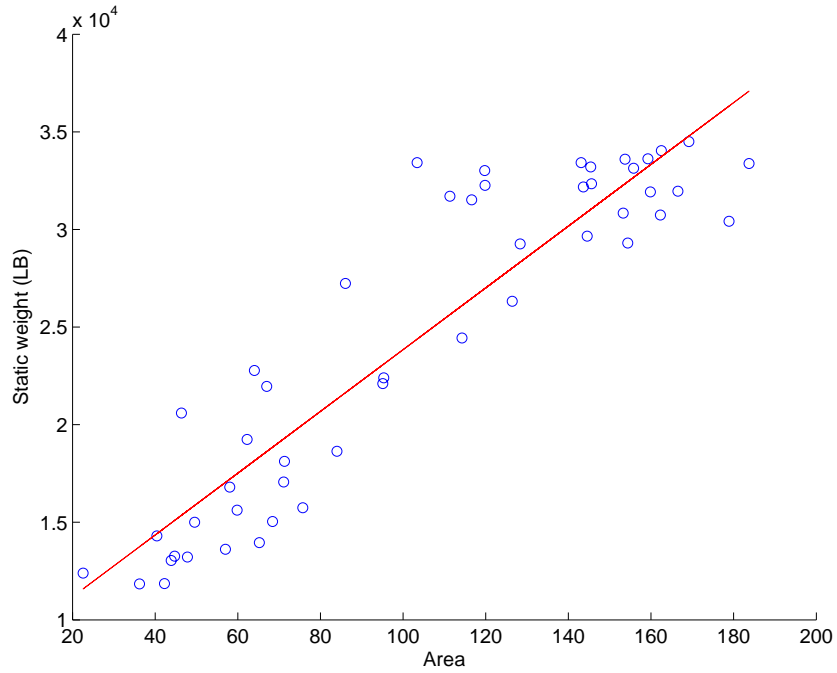


Figure 5-26: Load Calibration Function ($y = 158.2x + 8020.5$) for BLL.2 on Drive Axle.

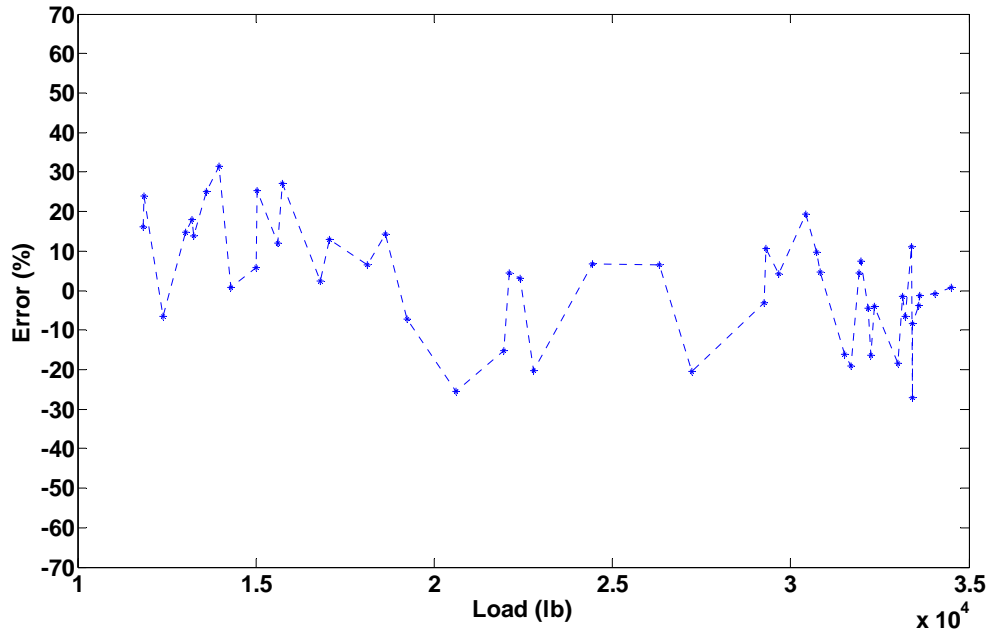


Figure 5-27: Error of Axle Load Measurement for BLL.2 on Drive Axle.

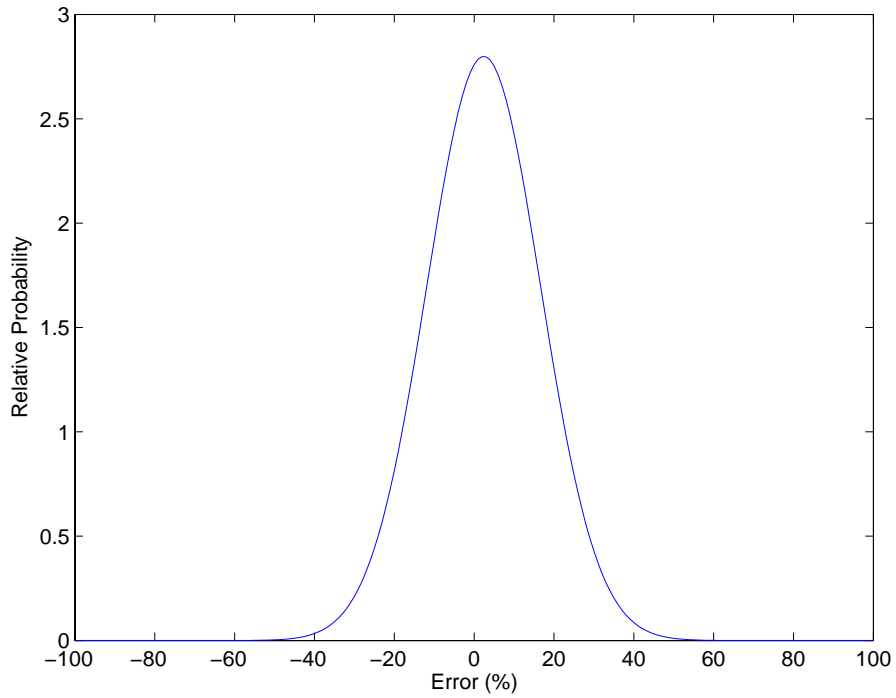


Figure 5-28: Probability Density Function ($\mu=0.4\%$, $\sigma=14.25\%$) for BLL.2 on Drive Axle.

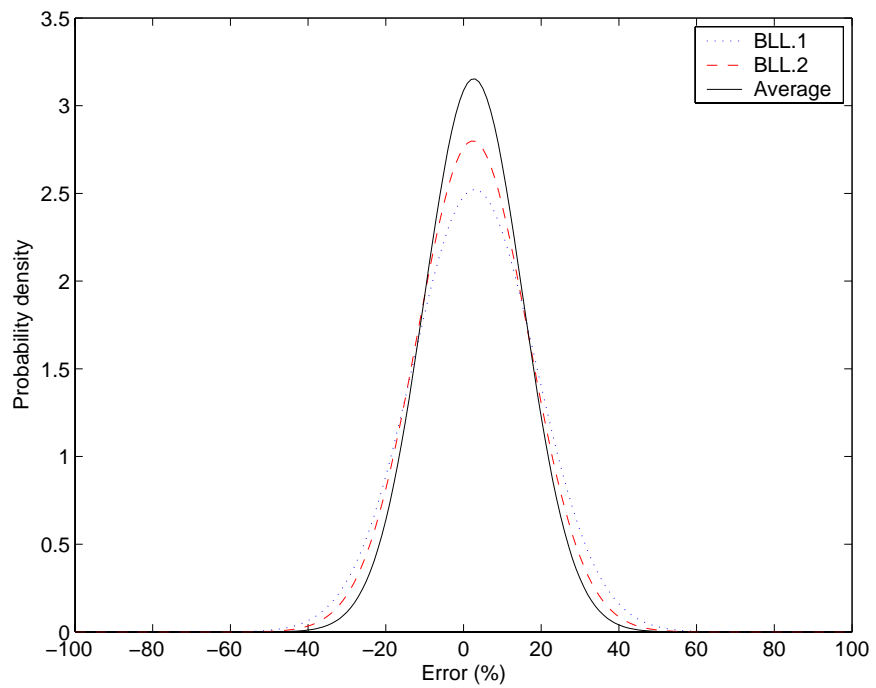


Figure 5-29: Probability Density Function ($\mu=2.62\%$, $\sigma=12.65\%$) for Average of BLL.1 and BLL.2 on Drive Axle.

Test Result of BLL.2 Sensor on Trailer Axle

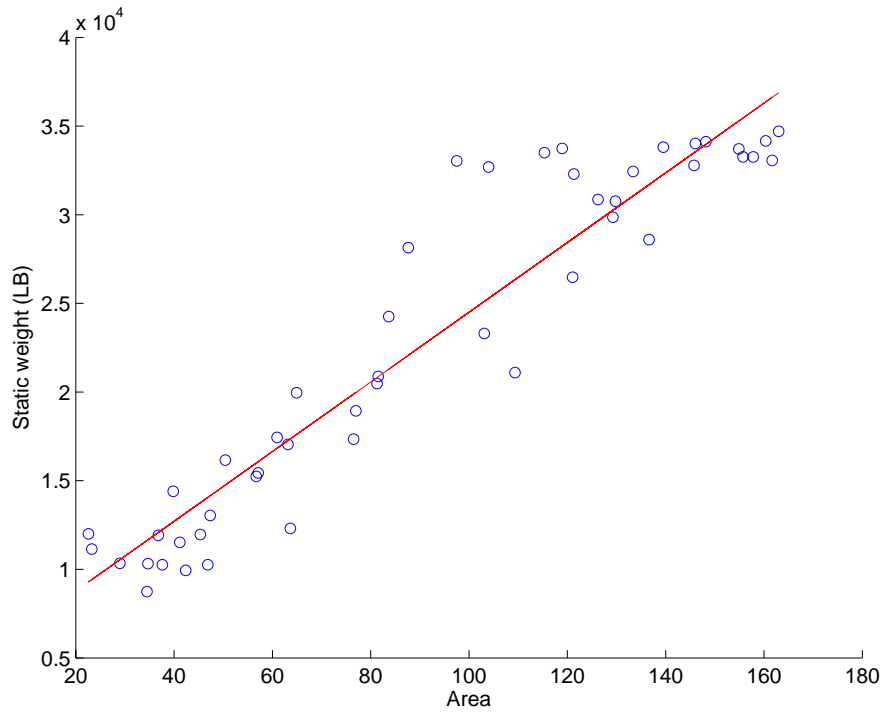


Figure 5-30: Load Calibration Function ($y = 196.56x + 4845.83$) for BLL.2 on Trailer Axle.

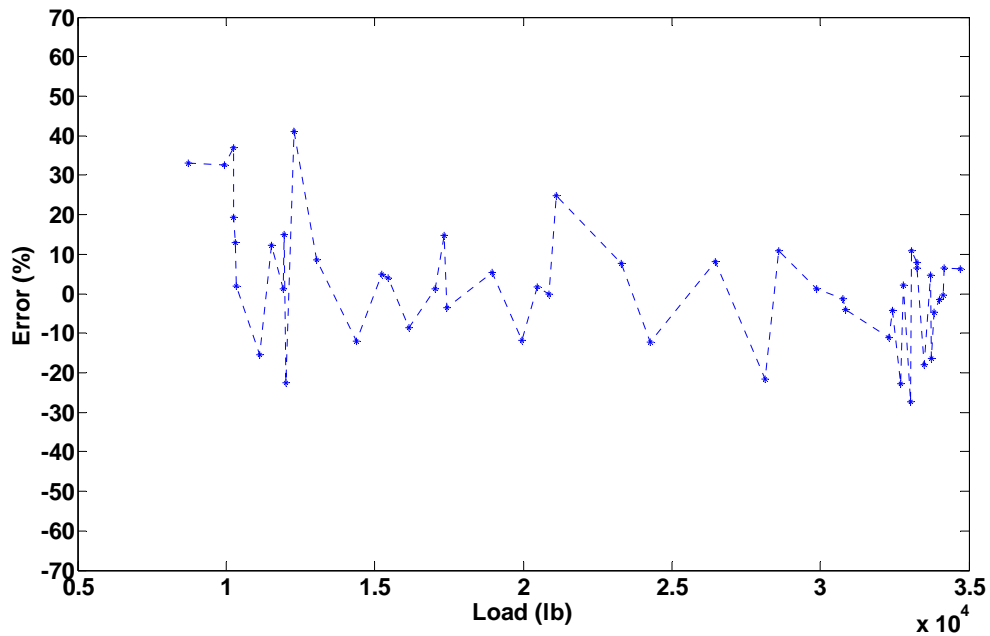


Figure 5-31: Error of Axle Load Measurement for BLL.2 on Trailer Axle.

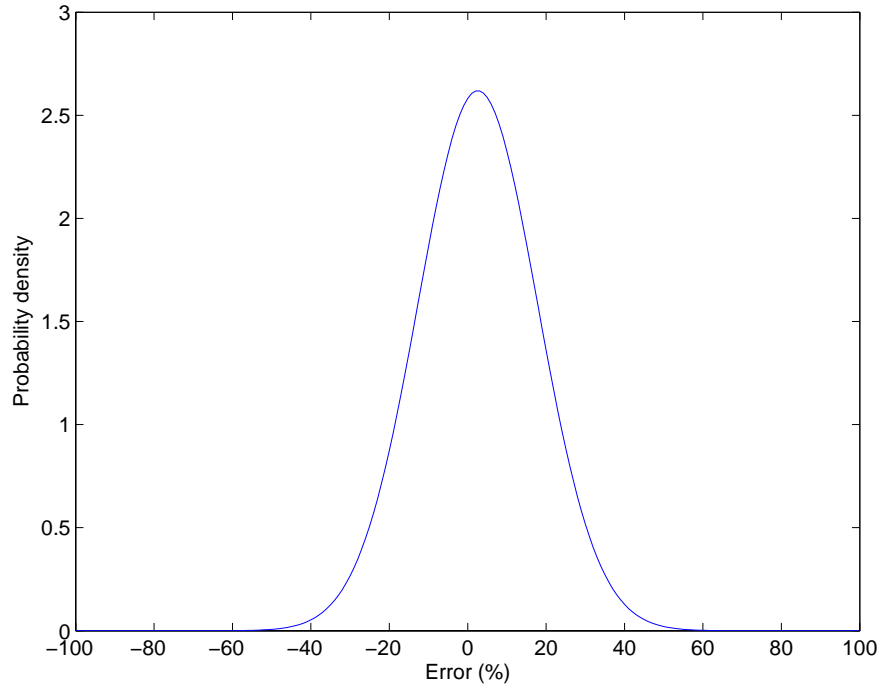


Figure 5-32: Probability Density Function ($\mu=2.57\%$, $\sigma=15.23\%$) for BLL.2 on Trailer Axle.

Table 5-3: Results of Test on BLL Sensors.

Sensor	Axle	Load Calibration Function	Accuracy Estimation	
			(μ, σ)	($\mu, 1.96\sigma$)
BLL.1	Drive Axle	$y = 144x + 5765$	(2.85%, 15.80%)	(2.85%, 30.97%)
	Trailer Axle	$y = 177.1x + 3542.3$	(6.31%, 23.46%)	(6.31%, 45.98%)
BLL.2	Drive Axle	$y = 158.2x + 8020.5$	(2.40%, 14.25%)	(2.40%, 27.93%)
	Trailer Axle	$y = 196.56x + 4845.8$	(4.44%, 16.29%)	(4.44%, 31.93%)

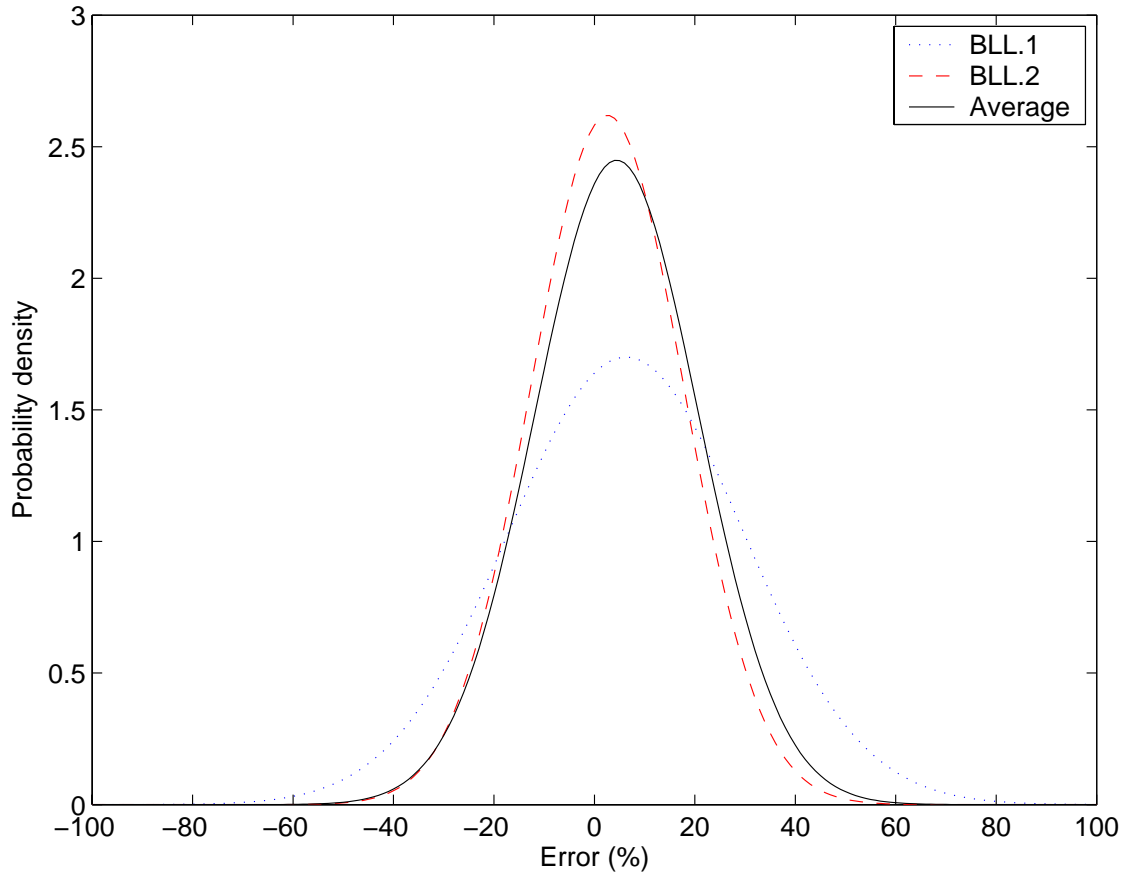


Figure 5-33: Probability Density Function ($\mu=4.44\%$, $\sigma=16.29\%$) for Average of BLL.1 and BLL.2 on Trailer Axle.

5.2.5 Test Results of TC-B.1 Sensor

Test Result of TC-B.1 Sensor on Drive Axle

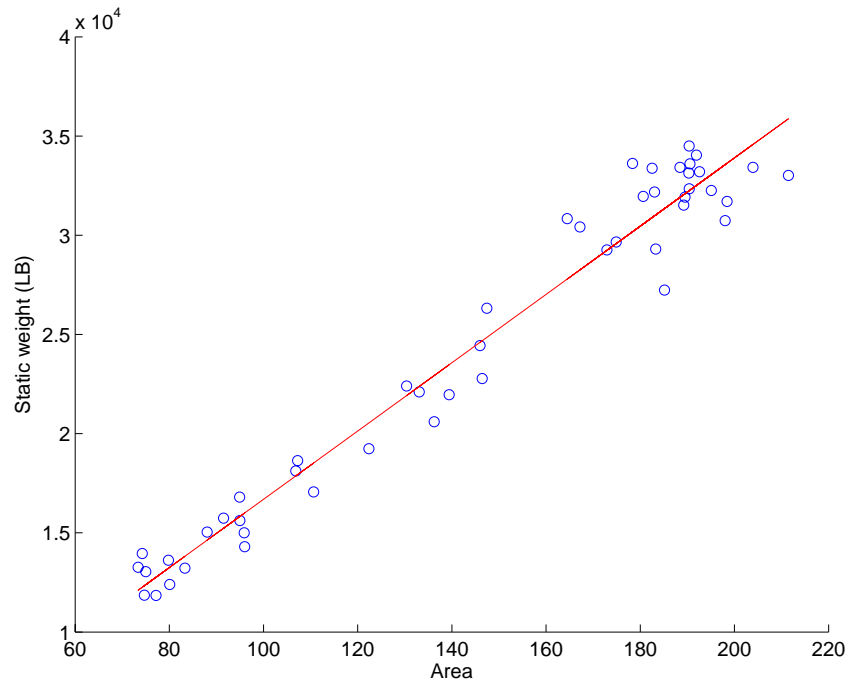


Figure 5-34: Load Calibration Function ($y = 172.1x - 522.9$) for TC-B.1 on Drive Axle.

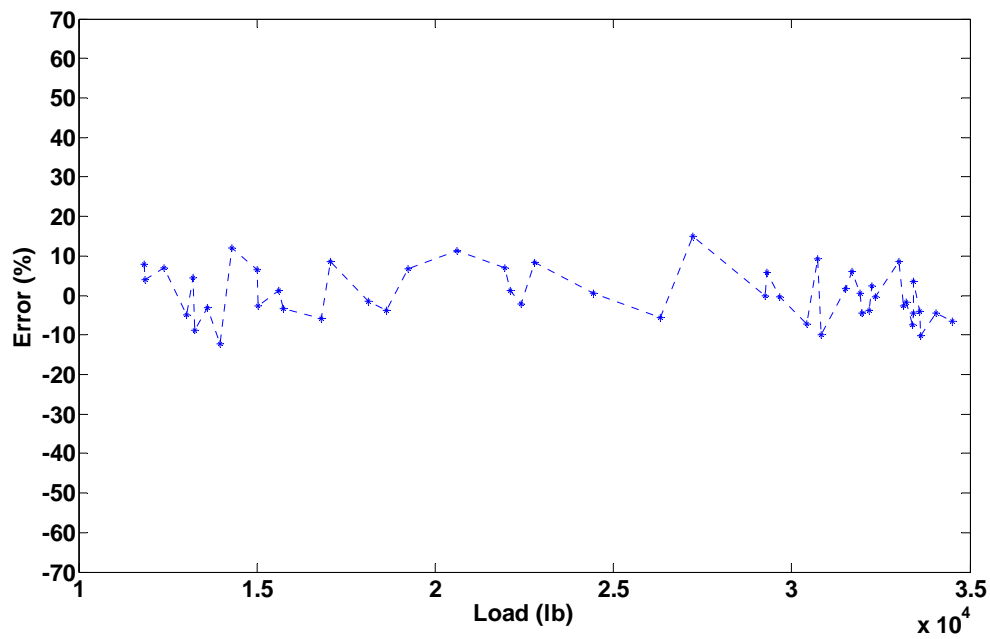


Figure 5-35: Error of Axle Load Measurement for TC-B.1 on Drive Axle.

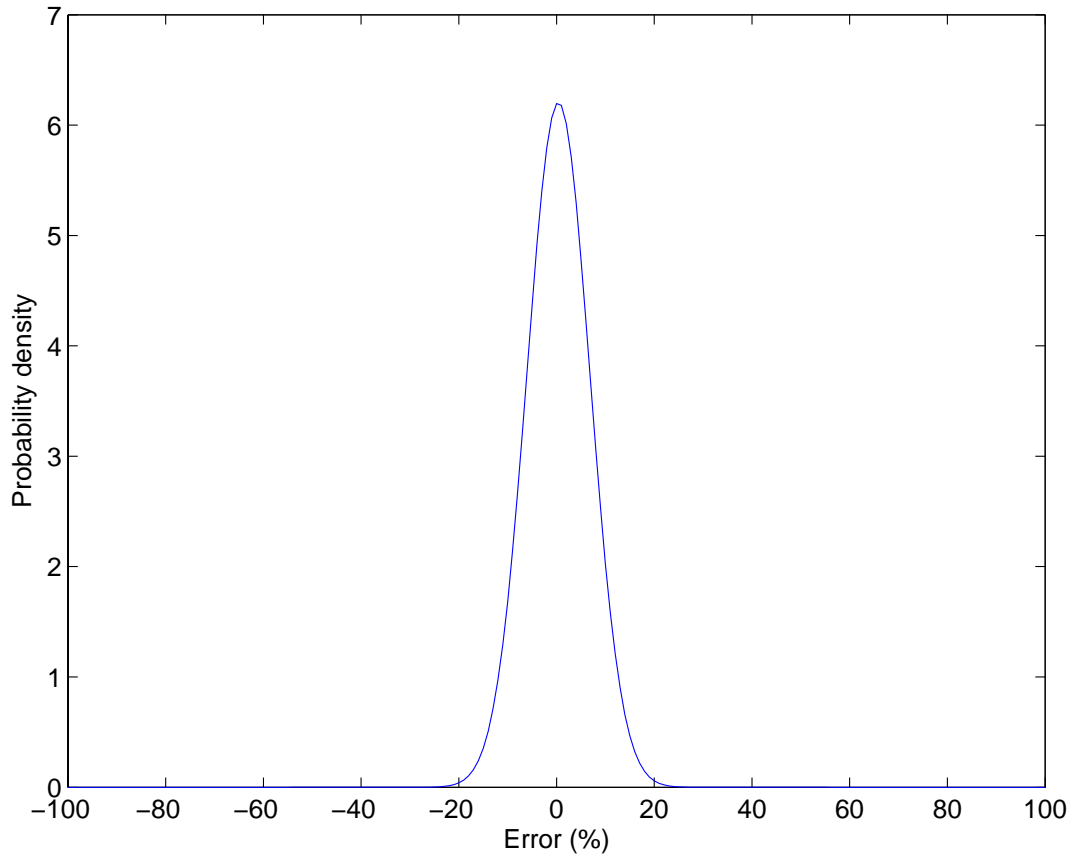


Figure 5-36: Probability Density Function ($\mu=0.38\%$, $\sigma=6.43\%$) for TC-B.1 on Drive Axle.

Test Result of TC-B.1 Sensor on Trailer Axle

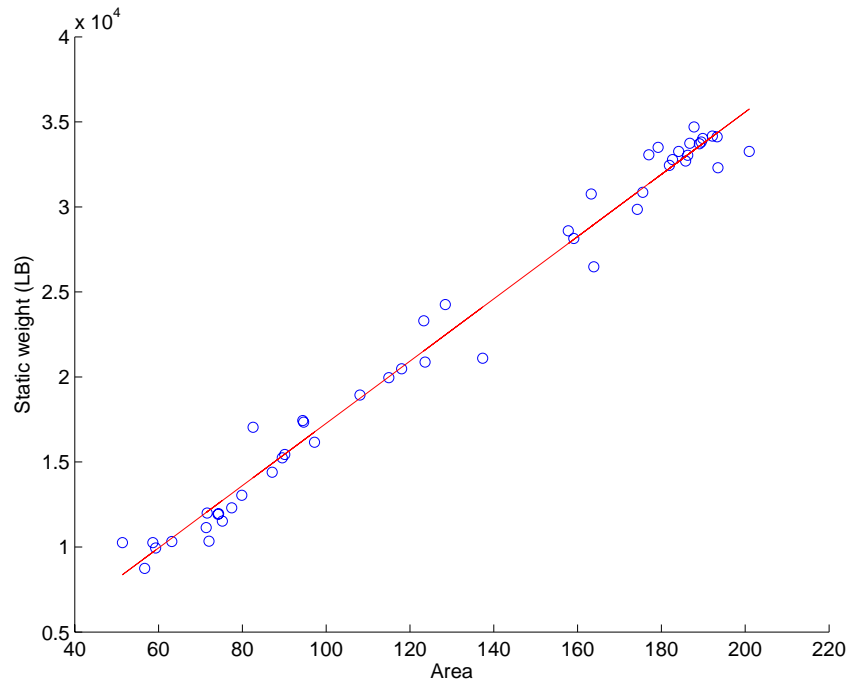


Figure 5-37: Load Calibration Function ($y = 183.1x - 1039.8$) for TC-B.1 on Trailer Axle.

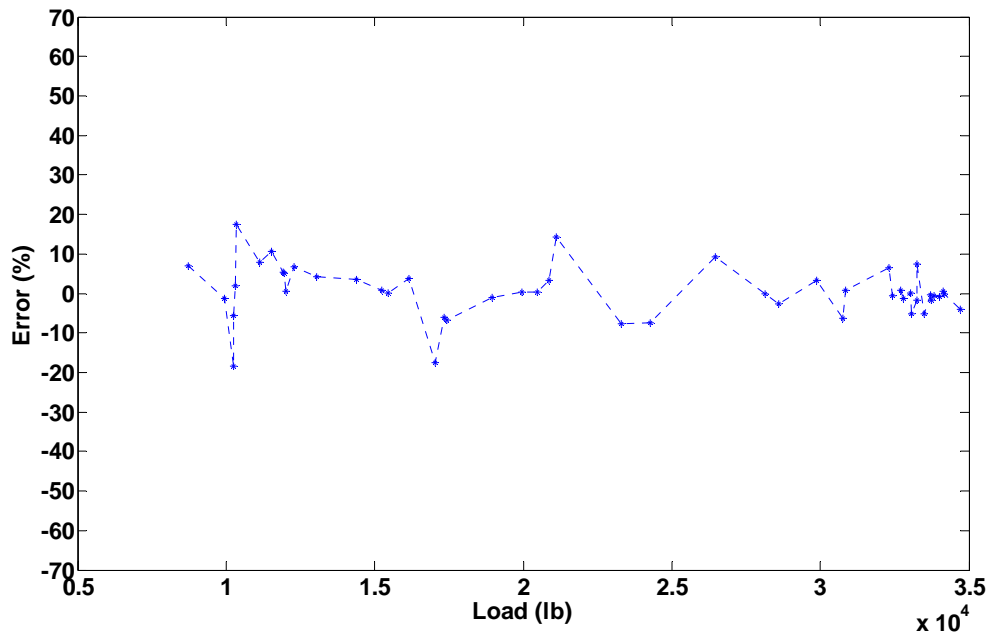


Figure 5-38: Error of Axle Load Measurement for TC-B.1 on Trailer Axle.

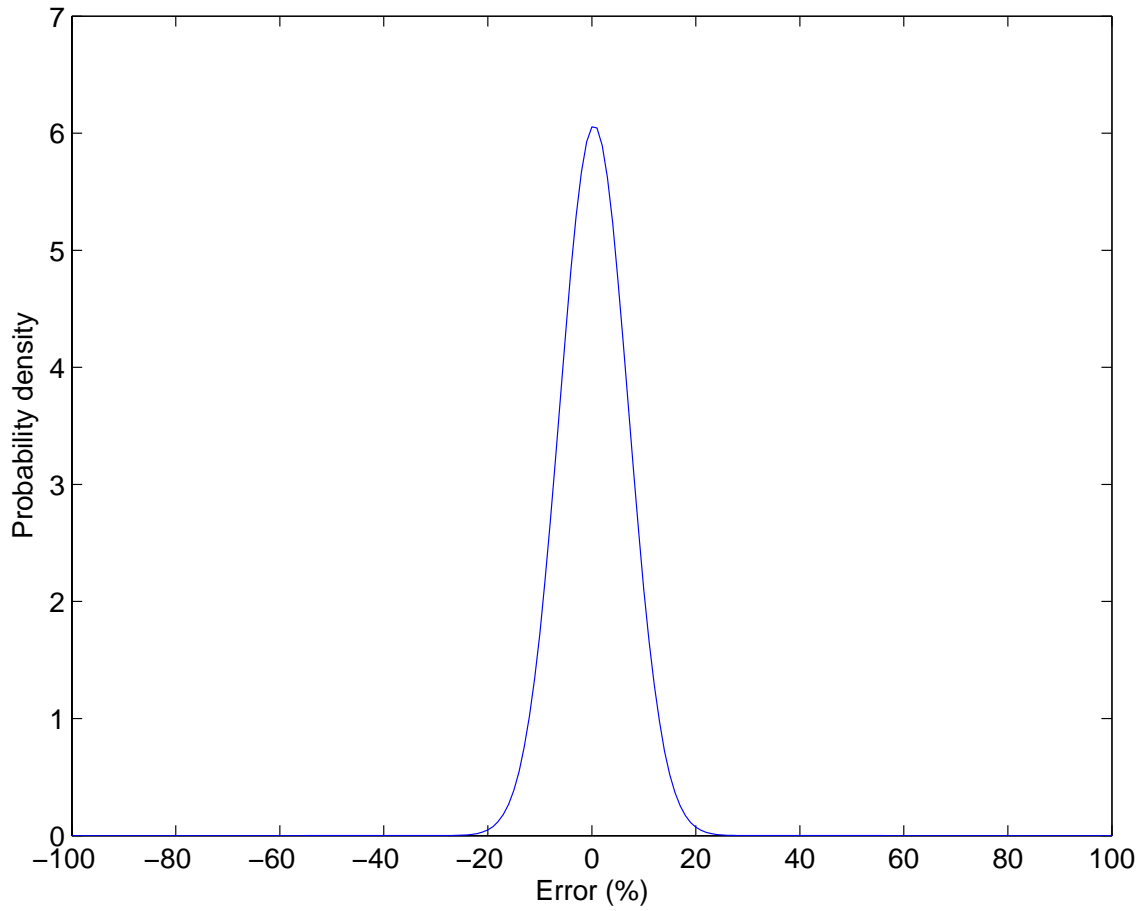


Figure 5-39: Probability Density Function ($\mu=0.43\%$, $\sigma=6.58\%$) for TC-B.1 on Trailer Axle.

5.2.6 Test Results of TC-B.2 Sensor

Test Result of TC-B.2 Sensor on Drive Axle

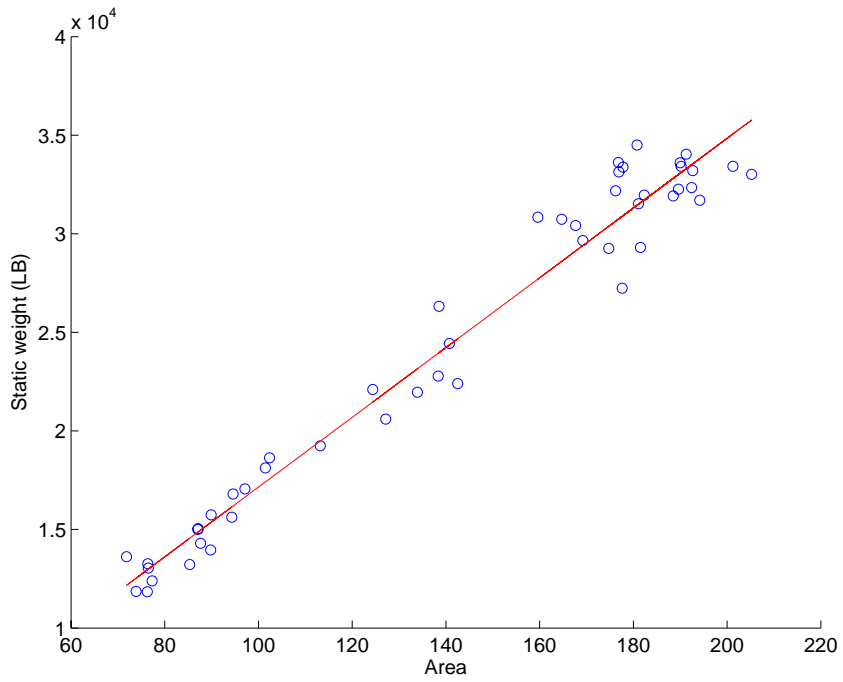


Figure 5-40: Load Calibration Function ($y = 176.9x - 541.7$) for TC-B.2 on Drive Axle.

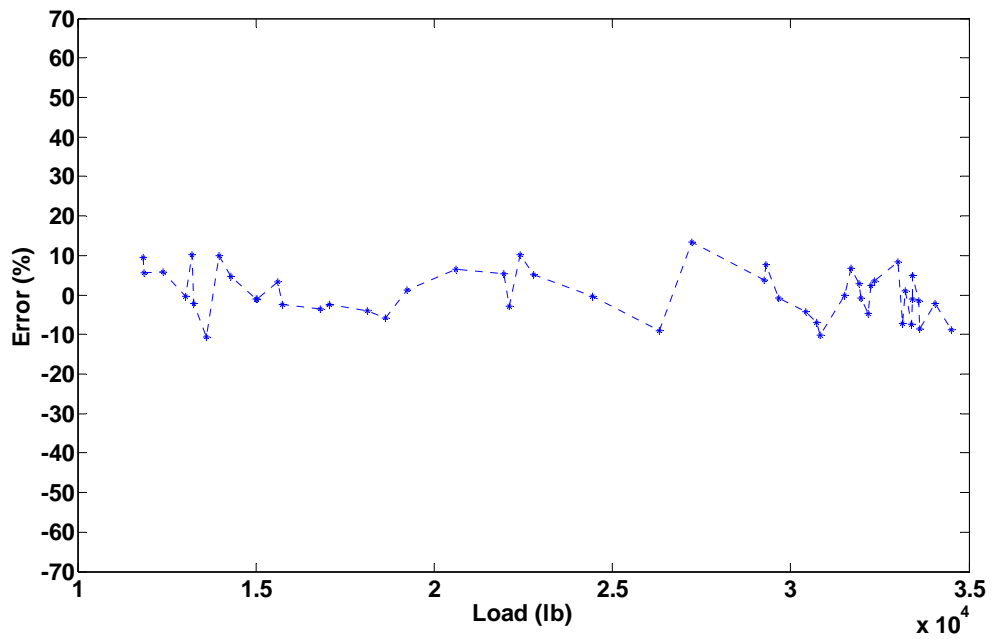


Figure 5-41: Error of Axle Load Measurement for TC-B.2 on Drive Axle.

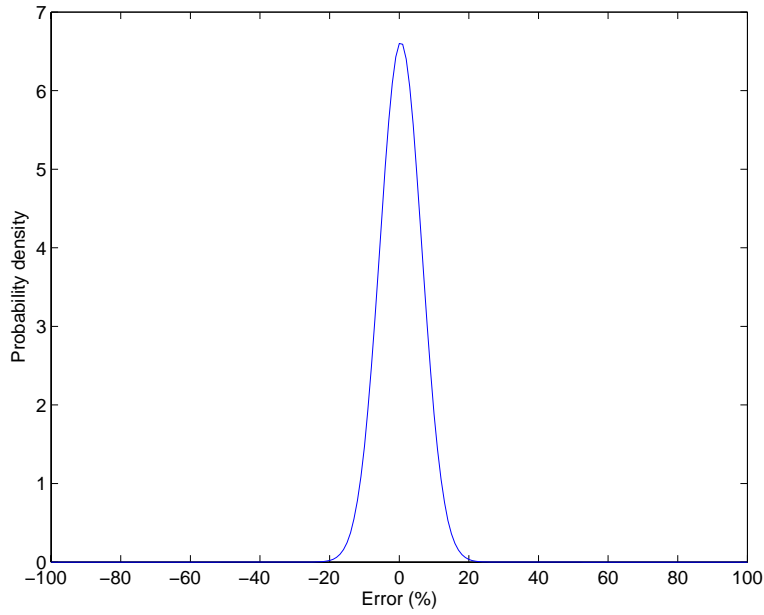


Figure 5-42: Probability Density Function ($\mu=0.45\%$, $\sigma=6.03\%$) for TC-B.2 on Drive Axle.

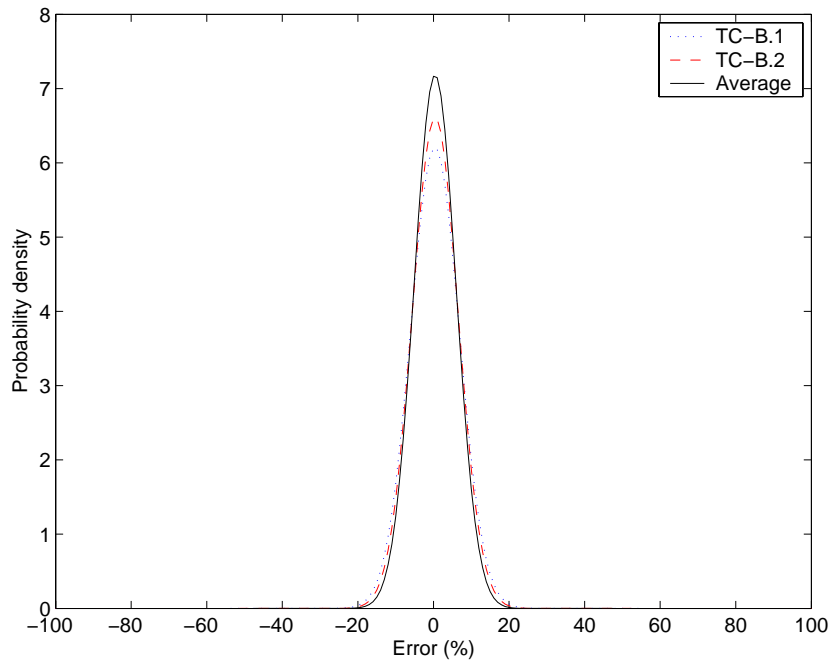


Figure 5-43: Probability Density Function ($\mu=0.42\%$, $\sigma=5.55\%$) for Average of TC-B.1 and TC-B.2 on Drive Axle.

Test of TC-B.2 Sensor on Trailer Axle

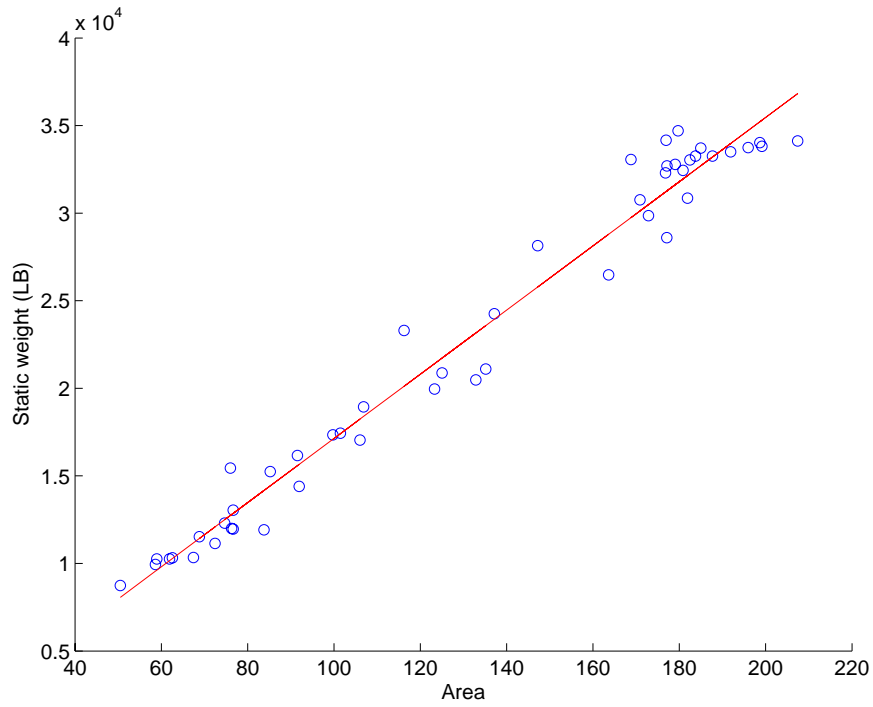


Figure 5-44: Load Calibration Function ($y = 183.2x - 1186.2$) for TC-B.2 on Trailer Axle.

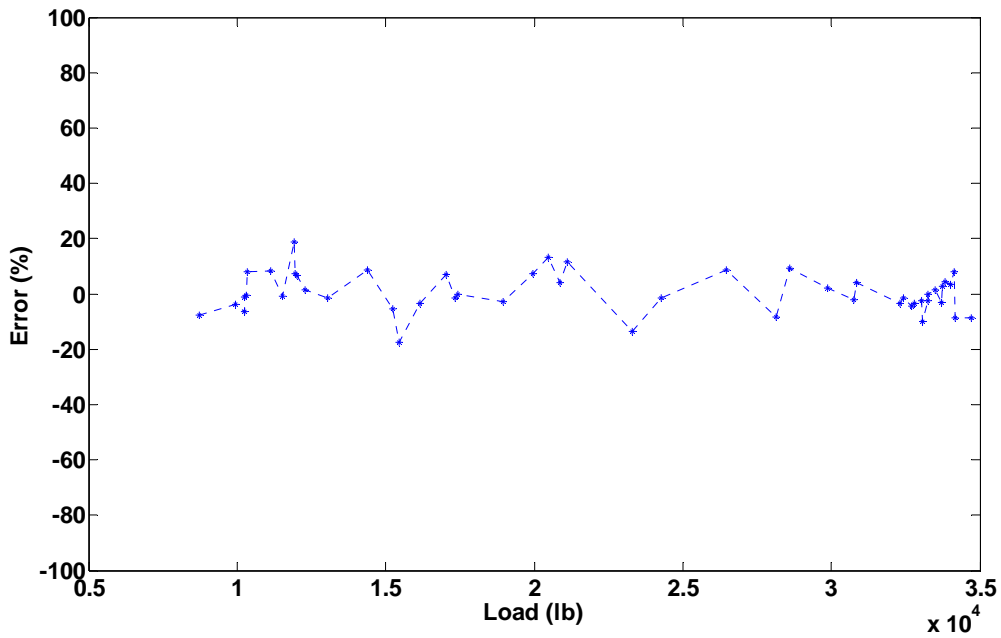


Figure 5-45: Error of Axle Load Measurement for TC-B.2 on Trailer Axle.

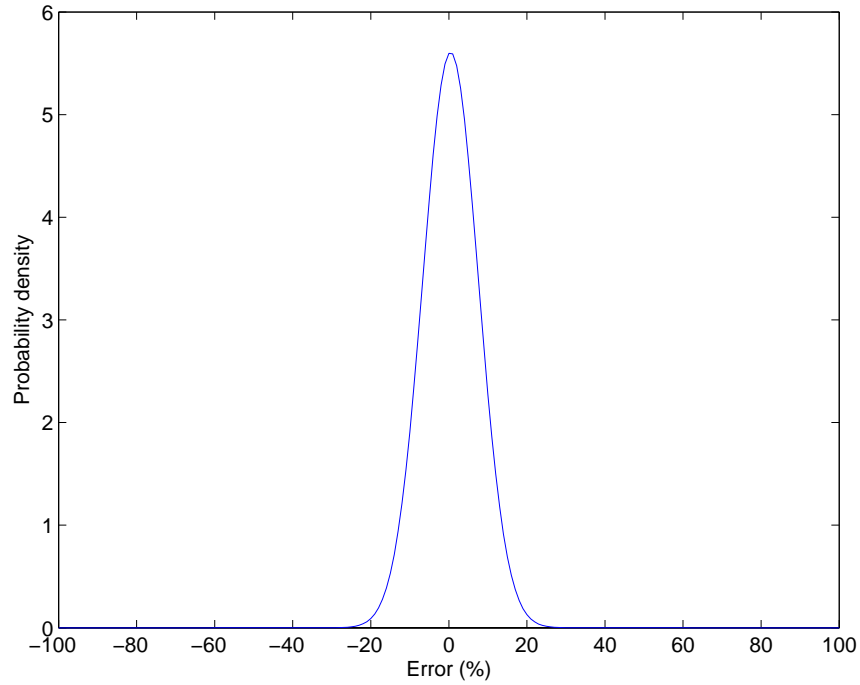


Figure 5-46: Probability Density function ($\mu=0.45\%$, $\sigma=7.11\%$) for TC-B.2 on Trailer Axle.

Table 5-4: Results of Test on TC-B Sensors.

Sensor	Axle	Load Calibration Function	Accuracy Estimation	
			(μ, σ)	($\mu, 1.96\sigma$)
TC-B.1	Drive Axle	$y = 172.1x - 522.9$	(0.38%, 6.43%)	(0.38%, 12.60%)
	Trailer Axle	$y = 183.1x - 1039.8$	(0.43%, 6.58%)	(0.43%, 12.90%)
TC-B.2	Drive Axle	$y = 176.9x - 541.7$	(0.45%, 6.03%)	(0.45%, 11.82%)
	Trailer Axle	$y = 183.2x - 1186.2$	(0.45%, 7.11%)	(0.45%, 13.94%)

Average for TC-B.1 and TC-B.2 on Trailer Axle

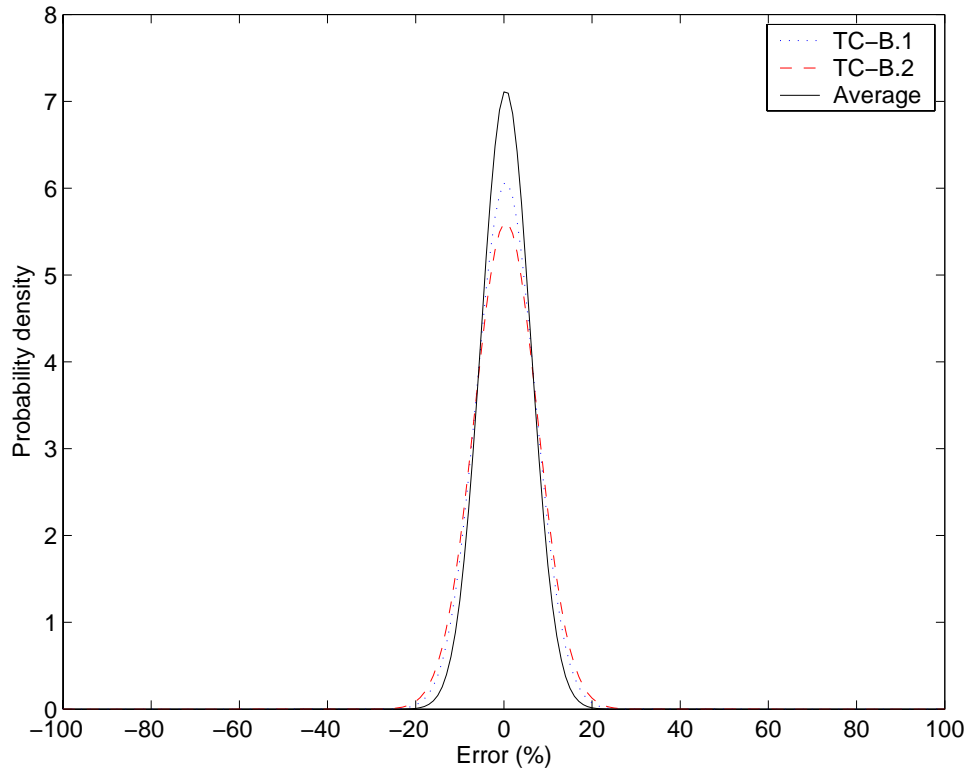


Figure 5-47: Probability Density Function ($\mu=0.44\%$, $\sigma=5.6\%$) for Average of TC-B.1 and TC-B.2 on Trailer Axle.

5.3 Summary

In this chapter, the integration load determination algorithm for piezoelectric sensors is introduced. The derivative method is used to detect the rising edge in response to the approaching axle and give out the threshold and range of the integration. The field test data have been used to evaluate different sensors. Among those sensors under test, the TC B sensor has the best test results. The accuracy for one TC-B sensor is around 12%–14%, with a 95% confidence requirement. The average of the two sensors can improve the measurement accuracy.

CHAPTER 6: PAVEMENT DEFLECTION LOAD DETERMINATION ALGORITHM FOR PIEZOELECTRIC SENSOR AND FIELD TEST

During the signal analysis of the piezoelectric sensor's output, not only a positive pulse is detected, but also a small negative response prior to the axle's arrival at the sensor is found. As stated in the previous chapter, the positive pulse is used to measure the truck's axle load. In this chapter, an analysis is made to characterize the negative response and determine the possibility of estimating the truck's axle load by using the negative response.

6.1 Sensor Responses to Pavement Deflection

Prior to introducing the load determination method based on pavement deflection, the response of WIM sensor, TC-B, will be analyzed. Then, the response from the pavement deflection can be found easily from the analysis. The reason for choosing the TC-B sensor is because it is accurate from the previous test results, and the circular section structure has a better response in the horizontal direction. [Figure 6-1](#) shows the data from one pass of a five-axle truck.

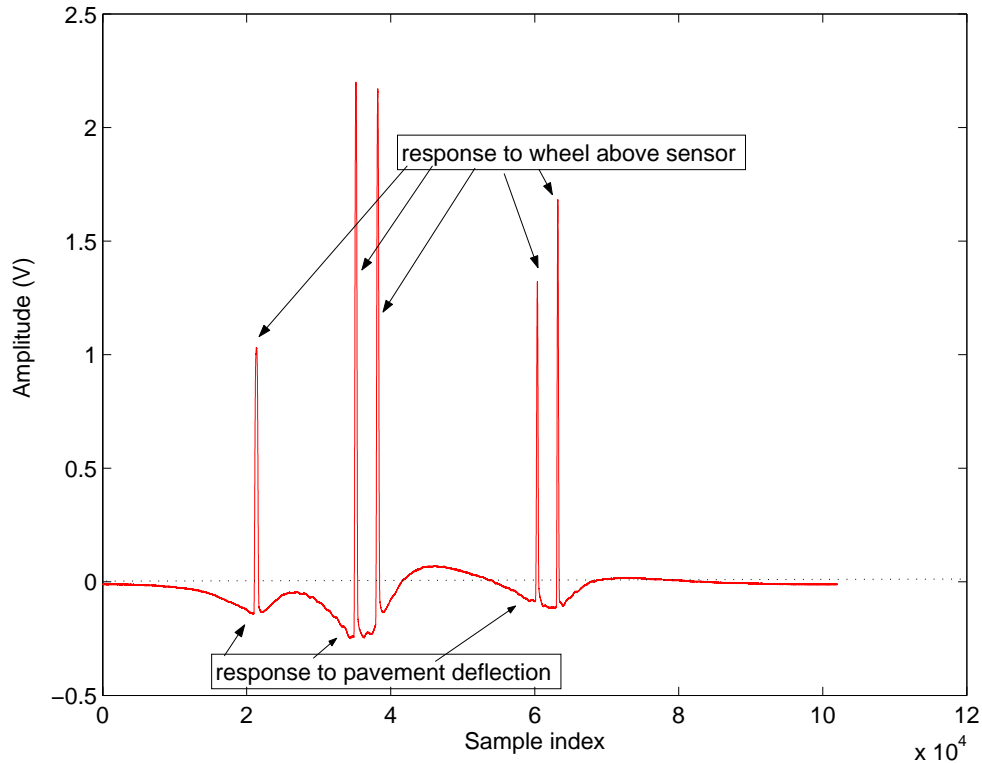


Figure 6-1: An Example of Pavement Deflection.

The positive pulses in the data are generated by the passing vehicle's wheels above the sensor, but before the pulse's arrival a signal dropdown is detected. This signal dropdown is the response to the pavement deflection which has maximum value when the wheels are right above the sensor. According to a study by Paul J. Cosentino, the horizontal force can be used to evaluate the vehicle axle loads [26]. Although the paper develops some models, the study lacks related field test WIM data for comparison. In order to use the response to deflection, some data processing is necessary. The negative dropdown value cannot be used directly. Since the pavement deflection is a very low frequency signal lasting much longer than the positive pulse, a longer tail following the positive pulse will appear when it is fed into the piezoelectric sensor's model, a resistor-capacitor (RC) circuit. So, the tail induced by a drive axle response will be added to the response of the trailer axle. To detect the deflection, signal recovery processing is necessary and will be discussed before addressing the pavement deflection load evaluation method.

6.2 Signal Recovery Processing

Since the model of the piezoelectric sensor was set up previously, the signal recovery processing can be evaluated easily according to this model.

$$U_{in}(s) = H^{-1}(s) \cdot U_{out}(s), \quad (6-1)$$

where

$$H(s) = \frac{sRC}{sRC + 1}, \quad (6-2)$$

$H(s)$: Model of piezoelectric sensor (transfer function);

R, C : Equivalent resistor and capacitor;

U_{in} : Input of piezoelectric model;

U_{out} : Output of piezoelectric model.

Referring to the datasheet of the TC-B sensor, the equivalent capacitor C is 27.18 nF. So, considering the equivalent resistor R , 18 M Ω , the time constant is RC , 0.49. The transfer function becomes $H(s) = 0.49s / (0.49s + 1)$. An example of the signal recovery is shown in [Figure 6-2](#). Since it is impossible for the parameters used for the model to be the same as the real ones, inevitable errors may exist and affect the recovery processing. However, it is still helpful to use these parameters during the data processing. The dropdown value before the positive pulse will be used as the relative deflection value for the load estimation.

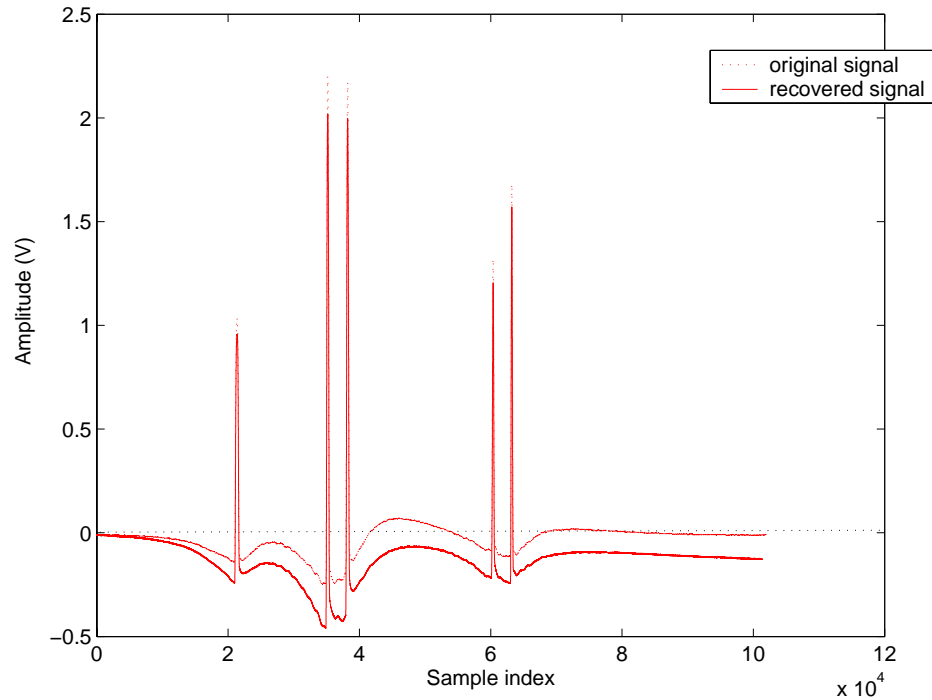


Figure 6-2: An Example of Signal Recovery.

6.3 Pavement Deflection Load Determination Algorithm for Piezoelectric Sensor

In this discussion, the vibrations of concrete pavement excited by heavy trucks are measured by using a pavement-embedded piezoelectric WIM sensor and are analyzed in different load situations (empty truck, lightly-loaded truck and fully-loaded truck). The corresponding results show that the piezoelectric WIM sensor can be used as a vibration sensor in addition to the load measurement.

From the acquired data, pavement vibration around the sensor related to the same moving truck is analyzed. The results show that the low-frequency component (about 2.5 Hz) of the pavement vibration excited by the truck can propagate further than other frequency components. The strongest vibration happens around the drive axle, which is about 10–20 Hz. After comparing the vibration between different loaded trucks, the results show that empty trucks have a much stronger vibration than others.

It is obvious that the fluctuation around the sensor response to pavement deflection is coming from pavement vibration generated by the vehicle's dynamics.

Therefore, removing those vibrations around the deflection signal can improve the measurement accuracy. The easiest way to do so is to make a curve fitting for the signal, as shown in Figure 6-3. The corresponding deflection signal is extracted from the original signal easily. Having this deflection signal available, the load estimation can be made by following the flowchart shown in Figure 6-4.

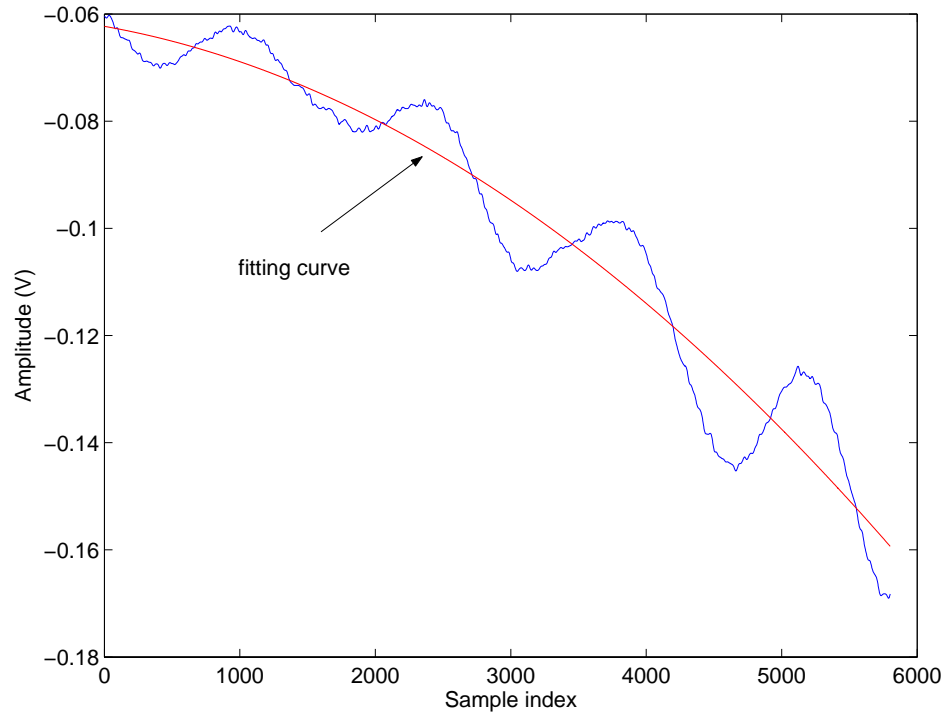


Figure 6-3: Deflection Curve Fitted to Remove Pavement Vibration (Dynamic Load).

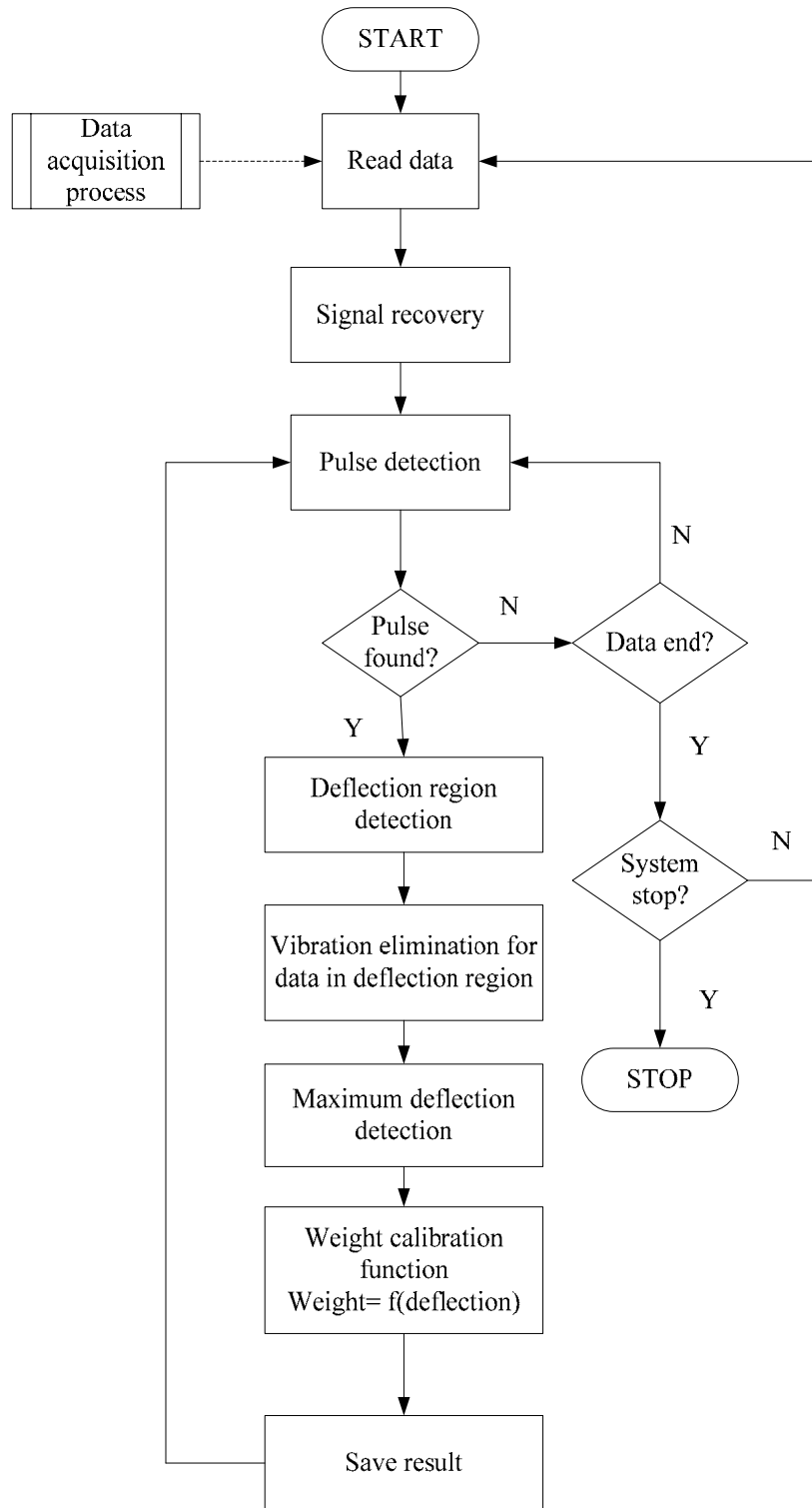


Figure 6-4: Flowchart of Pavement Deflection Weighing Method for Load Determination.

6.3.1 Results of Field Test Data

Test Result of TC-B.1 Sensor on Drive Axle

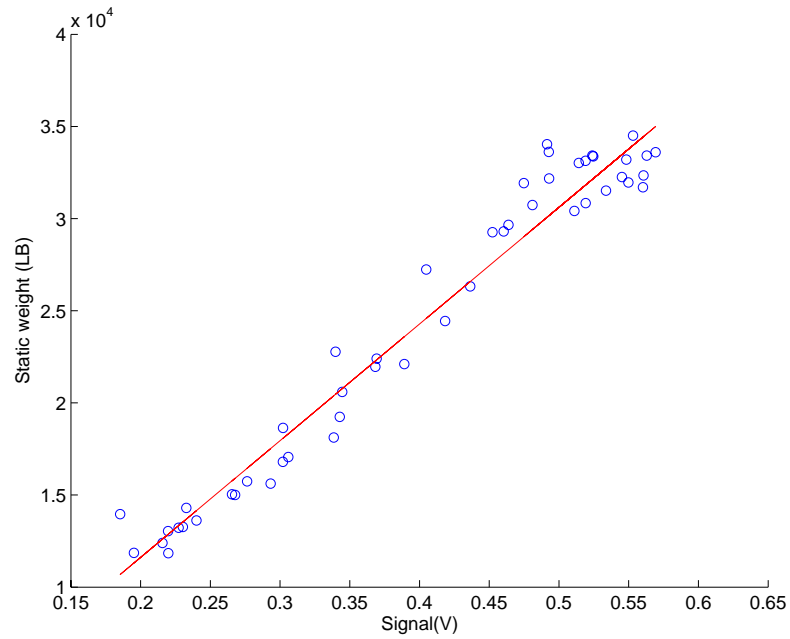


Figure 6-5: Load Calibration Function ($y = 63698.1x - 1116.4$) for TC-B.1 on Drive Axle.

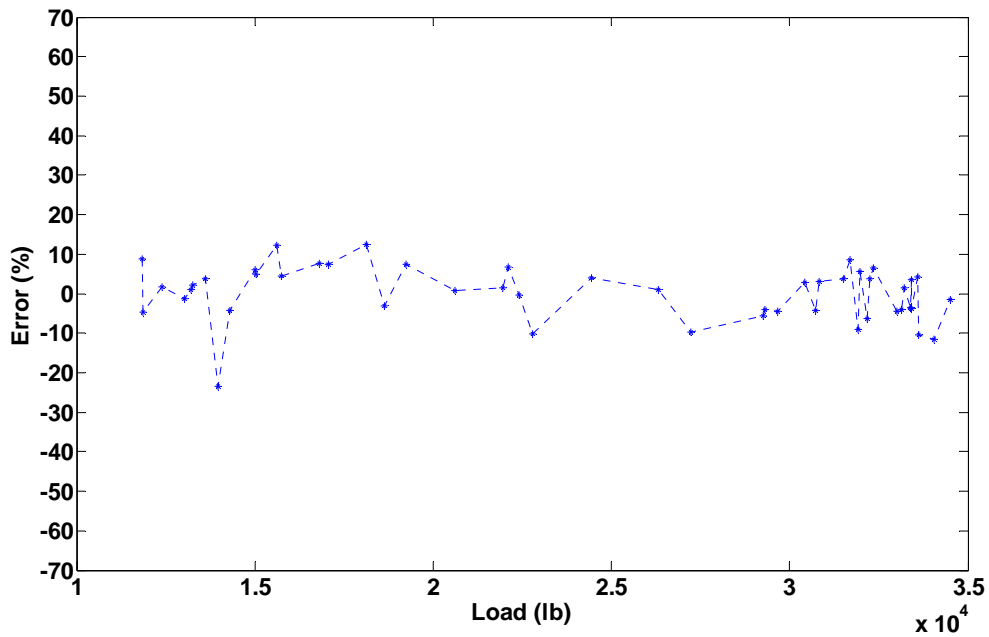


Figure 6-6: Error of Axle Load Measurement for TC-B.1 on Drive Axle.

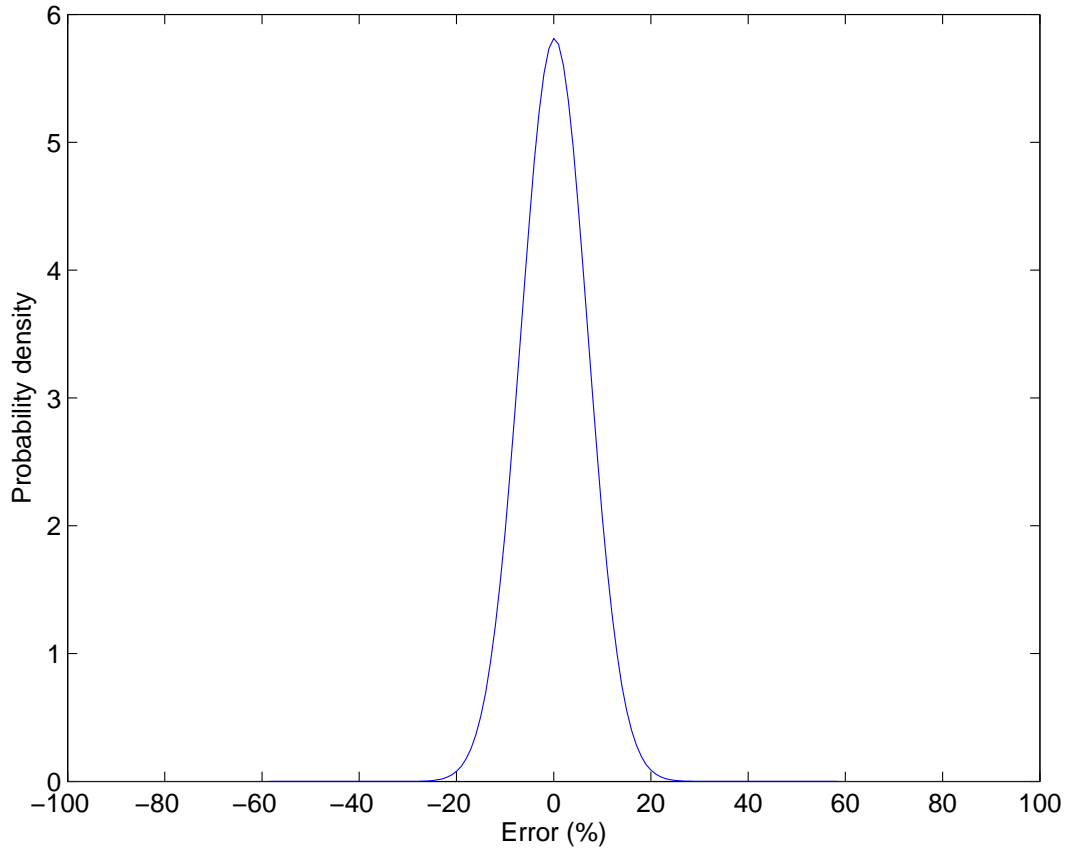


Figure 6-7: Probability Density Function ($\mu=0.14\%$, $\sigma=6.86\%$) for TC-B.1 on Drive Axle.

Test Result of TC-B.1 Sensor on Trailer Axle

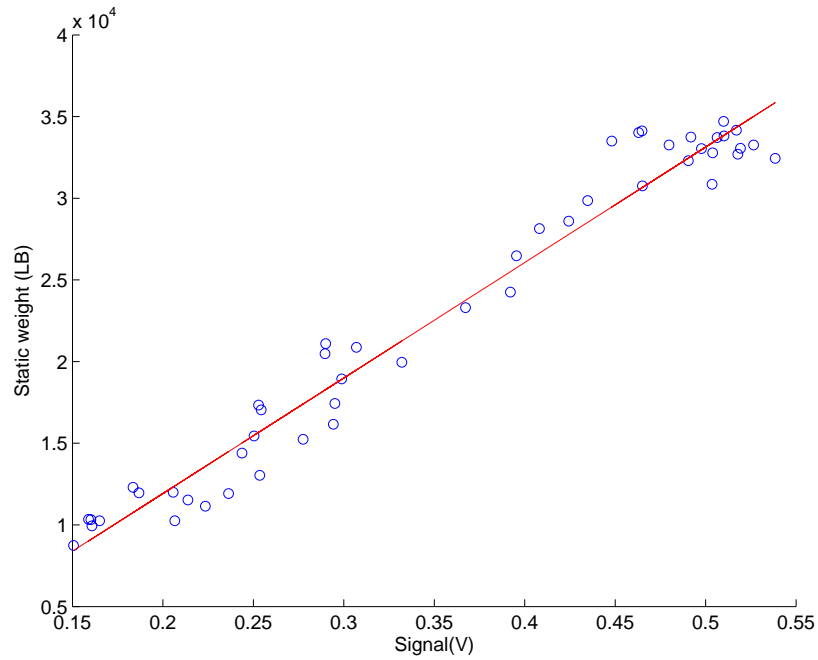


Figure 6-8: Load Calibration Function ($y = 70570.4x - 2111.6$) for TC-B.1 on Trailer Axle.

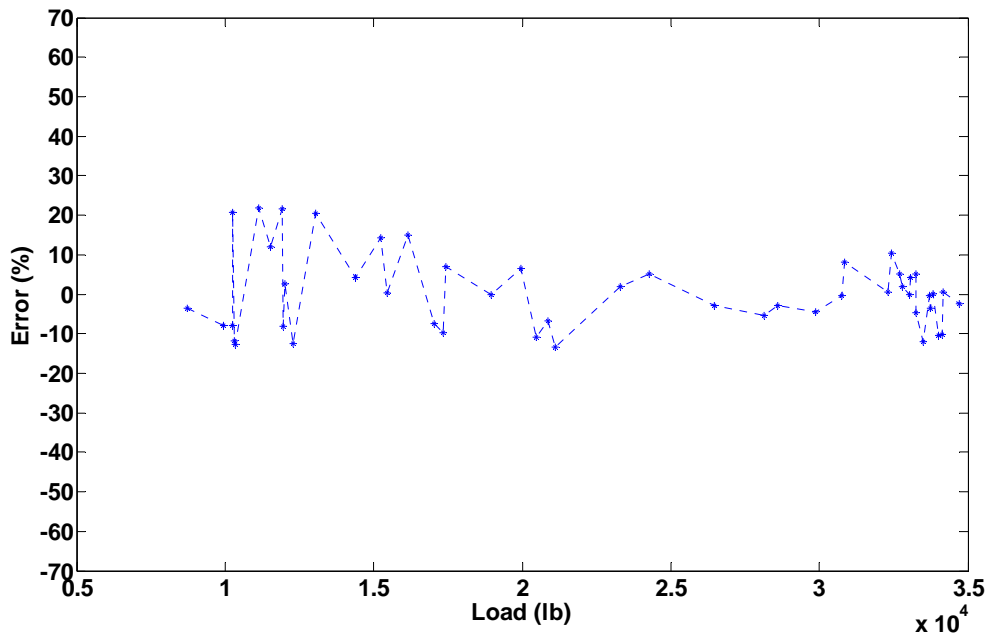


Figure 6-9: Error of Axle Load Measurement for TC-B.1 on Trailer Axle.

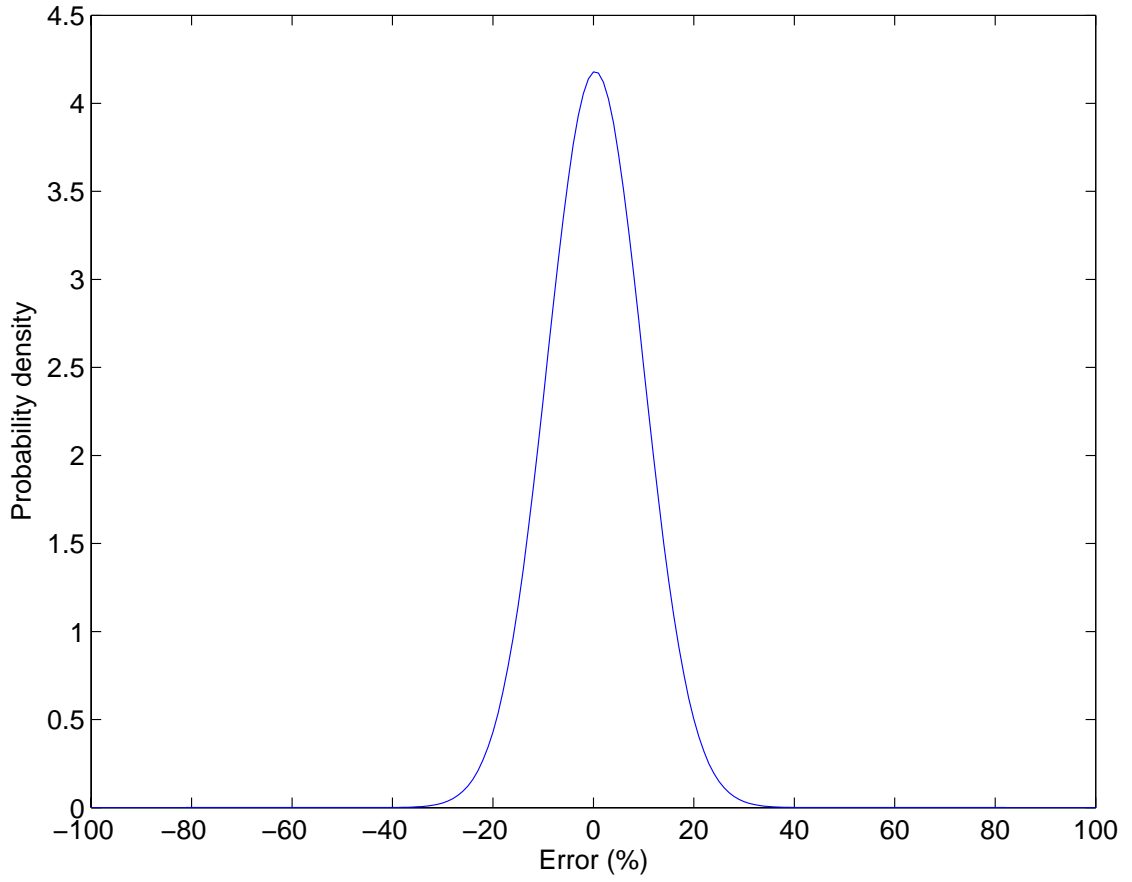


Figure 6-10: Probability Density Function ($\mu=0.36\%$, $\sigma=9.54\%$) for TC-B.1 on Trailer Axle.

Test Result of TC-B.2 Sensor on Drive Axle

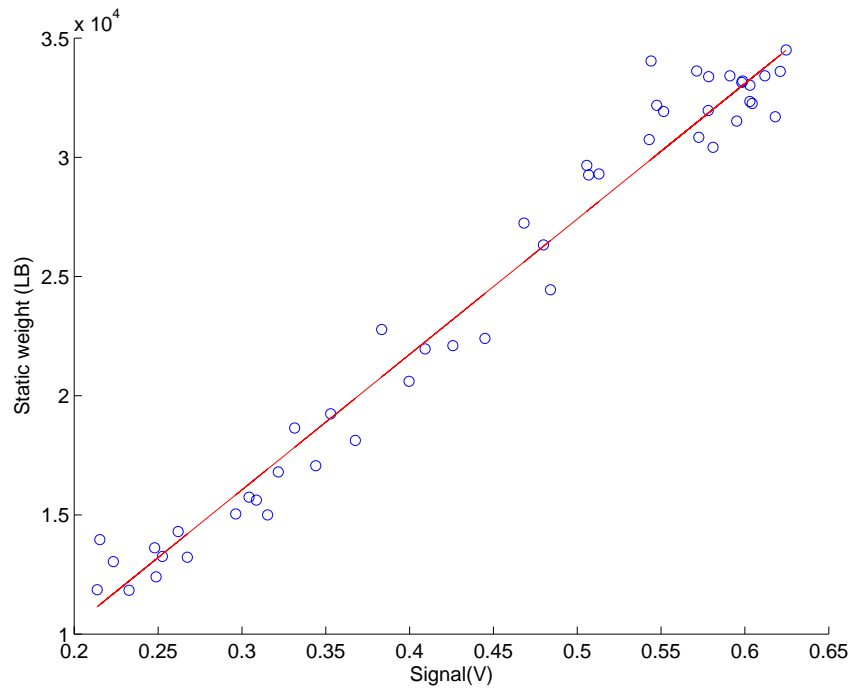


Figure 6-11: Load Calibration Function ($y = 57070.8x - 1054.0$) for TC-B.2 on Drive Axle.

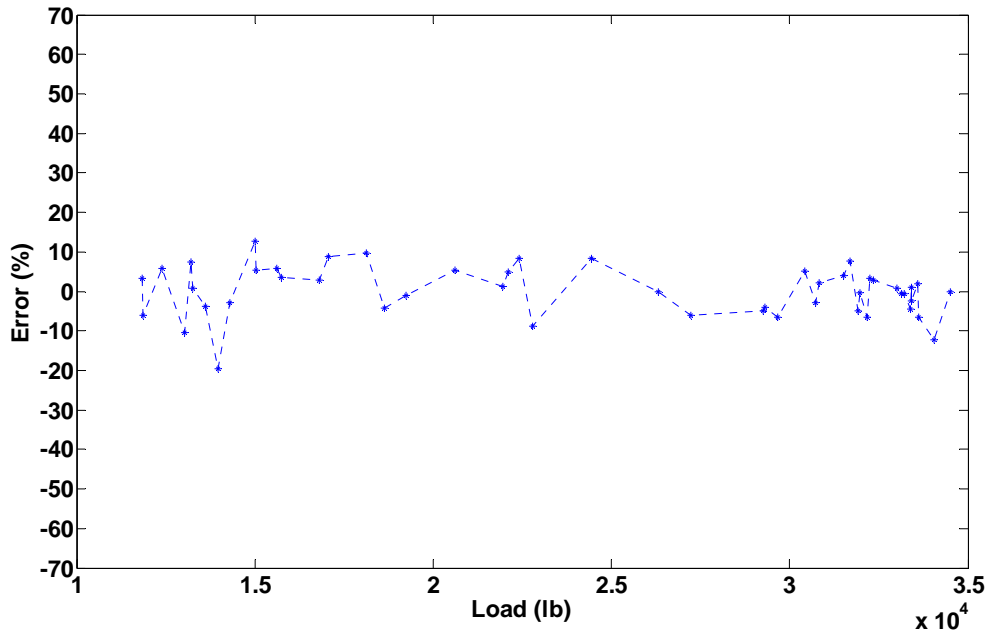


Figure 6-12: Error of Axle Load Measurement for TC-B.2 on Drive Axle.

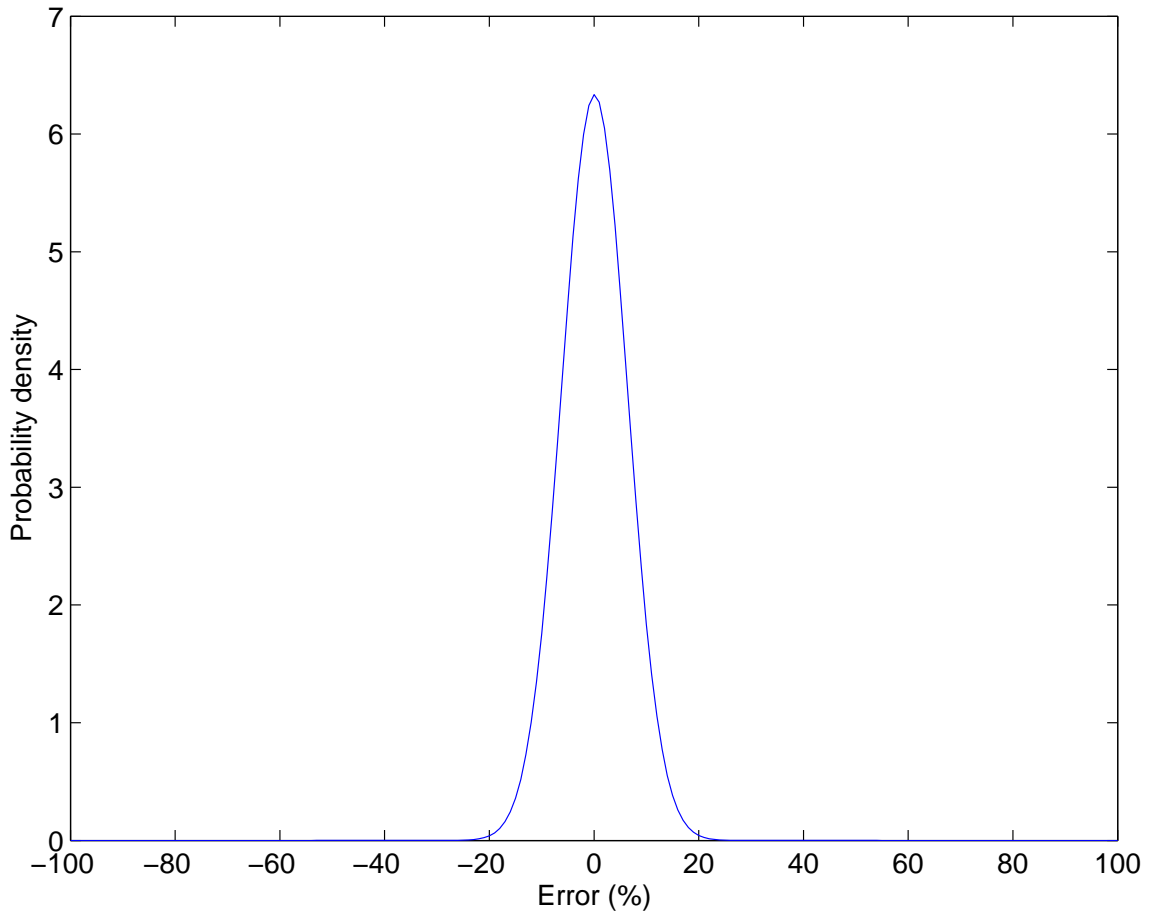


Figure 6-13: Probability Density Function ($\mu=0.1\%$, $\sigma=6.30\%$) for TC-B.2
on Drive Axle.

Test Result of TC-B.2 Sensor on Trailer Axle

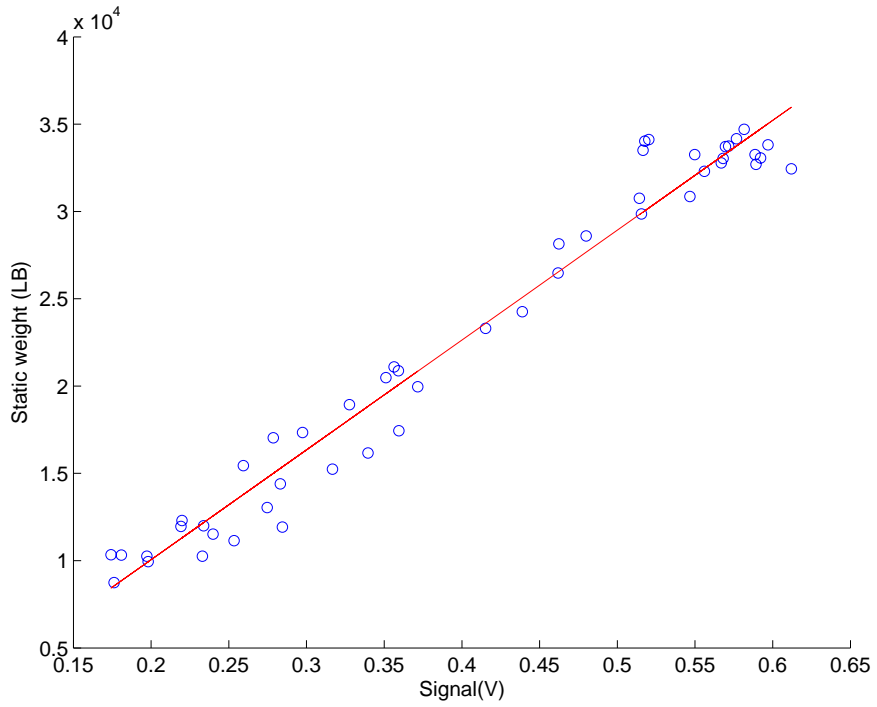


Figure 6-14: Load Calibration Function ($y = 62906.7x - 2526.7$) for TC-B.2 on Trailer Axle.

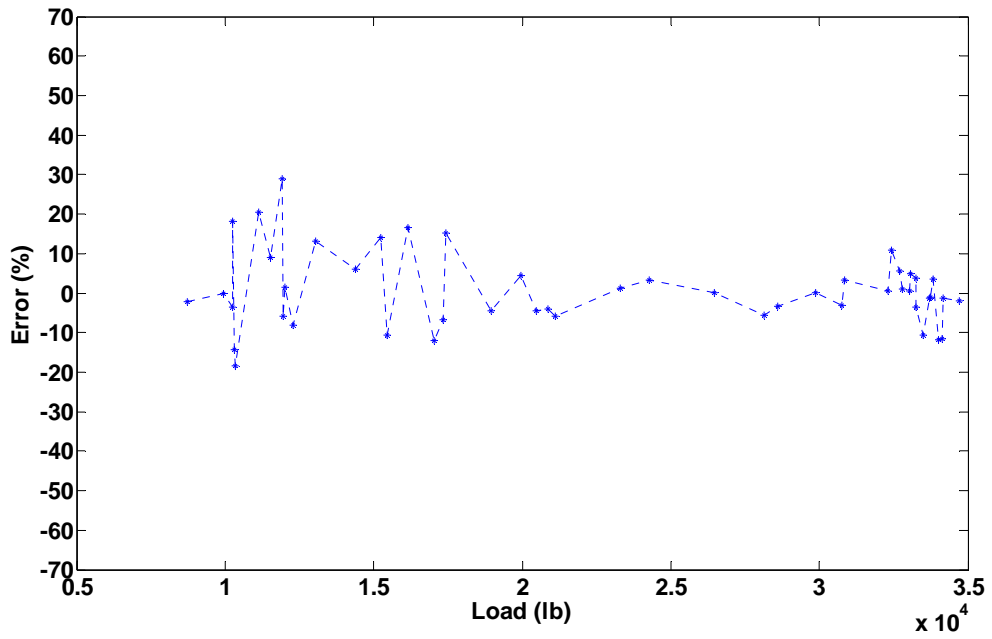


Figure 6-15: Error of Axle Load Measurement for TC-B.2 on Trailer Axle.

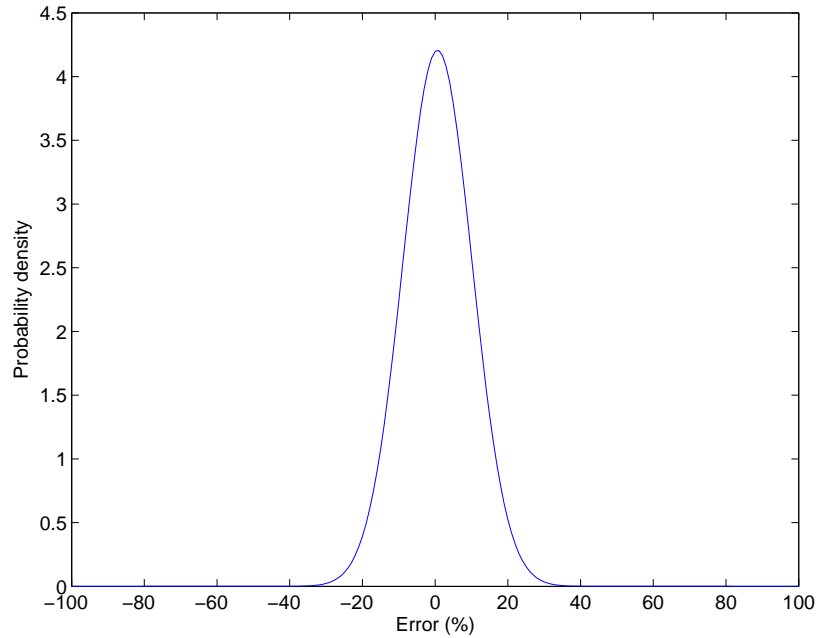


Figure 6-16: Probability Density Function ($\mu=0.65\%$, $\sigma=9.48\%$) for TC-B.2 on Trailer Axle.

Table 6-1: Result of Test on TC-B Sensor with Pavement Deflection Weighing Method

Sensor	Axle	Load Calibration Function	Accuracy Estimation	
			(μ, σ)	($\mu, 1.96\sigma$)
TC-B.1	Drive Axle	$y = 63698.1x - 1116.4$	(0.14%, 6.86%)	(0.14%, 13.45%)
	Trailer Axle	$y = 70570.4x - 2111.6$	(0.36%, 9.54%)	(0.36%, 18.70%)
TC-B.2	Drive Axle	$y = 57070.8x - 1054.0$	(0.10%, 6.30%)	(0.10%, 12.35%)
	Trailer Axle	$y = 62906.7x - 2526.7$	(0.65%, 9.48%)	(0.65%, 18.58%)

6.4 Summary

Although there are many varieties of WIM systems used, installation generally involves compromising the pavement structure. A bridge WIM system can be a good choice for a nondestructive application which uses a bridge as a platform to measure the vehicle's weight. However, locations available are limited for bridges. In order to find a

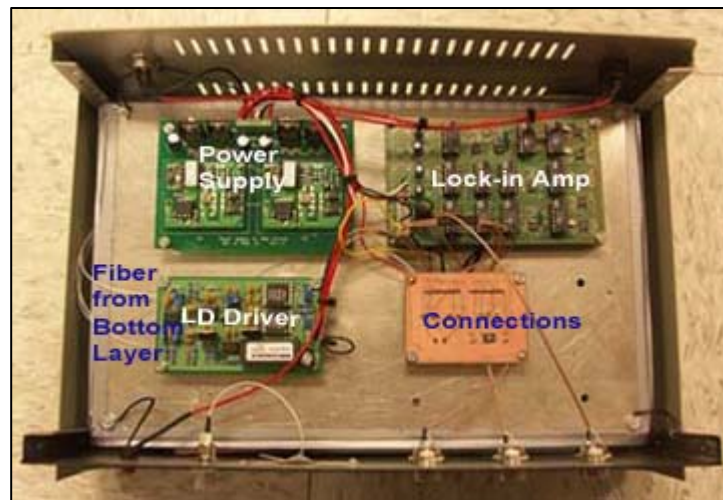
better way, much research has been conducted using different technologies. In 1999, Vortek, LLC (formed as an offshoot of Engineering Analysis, Inc.) tried to develop a seismic WIM (SWIM) system to measure the moving truck's weight without cutting pavement, but there are still no results published. In practicality, portable WIM sensors are a good choice. However, with sensors placed on the pavement surface, the traffic will be affected. It is not only uncomfortable for drivers but also dangerous for highway safety. On the other hand, vehicle dynamic motion may be increased since these portable mats are not flush with the pavement surface.

In this chapter, the pavement deflection load determination algorithm is introduced. This new algorithm uses the sensor's response of the pavement deflection to estimate the vehicle's static weight. The signal of pavement vibration is also analyzed and compared with existing research results. The piezoelectric model is used in the signal recovery for the load determination algorithm. The results of evaluating field data by this algorithm show that the accuracy of drive axle loads of around 13% (95% confidence) is better than the trailer axle of around 19%. Although the results are not as good as the results of integration algorithm, pavement deflection is proven to be useful for the WIM application. In conclusion, these test results indicate new sensors can be developed for conducting the WIM load measurements by monitoring pavement deflection.

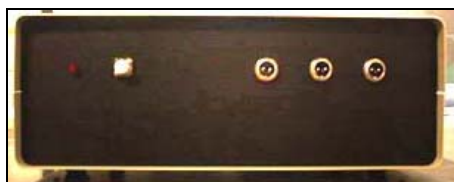
CHAPTER 7:FIBER OPTIC SENSOR FIELD TEST DATA

7.1 Equipment Setup

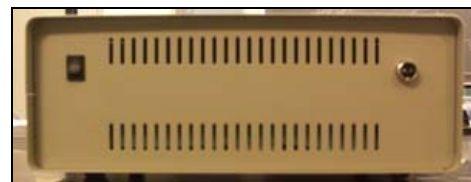
The laser diode (LD) driver and photo diode (PD) receiver, the dual-phase lock-in amplifier, and the fiber optic system (not including the FBG sensor component) constitute the signal detector for FBG sensor measurement, as shown in Figure 7-1: (a). It contains two layers. The bottom layer is for the fiber optic system, and the top layer is for the electronics. A PCI-MIO-16E-4 DAQ card from National Instruments was used for data acquisition. It has two 12-bit analog outputs, eight digital I/O lines, two 24-bit counters, and analog triggering. Figure 7-1: (b) and (c) show the front and back of the detector.



(a)



(b)



(c)

Figure 7-1: (a) Inside View of Developed Signal Detector; (b) Front of Detector; (c) Back of Detector.

A commercial interrogator I-sense-14000 from Intelligent Fiber Optic System (IFOS) was set up for FBG sensor measurement as well, as shown in [Figure 7-2](#). The system could be demultiplexed up to 16 channels, which means a total of 16 different center wavelengths could be tested simultaneously with real time display.



(a)



(b)

Figure 7-2: (a) Front of I-sense-14000; (b) Back of I-sense-14000.

7.2 Data Records

The signal coming from the forwardmost piezoelectric sensor opposite the traffic flow was taken as the trigger signal. Both pieces of equipment for the FBG sensor measurement were triggered once there was a positive edge detected. Data was manually stored after every selected vehicle passed through the sensor area, which was recorded as one test group, and was processed later on.

Field tests were conducted on August 11, 2004, and August 31, 2004. In order to compare the measured data easily with the records (static weights) of the nearby weigh station operated by the Department of Public Safety (DPS), eighteen-wheelers with identical axle groups and matching axle distances were selected for testing. These trucks have five axles in a common configuration. Axle two and axle three become one axle group, and axle four and axle five consist of another axle group, as illustrated in [Figure](#)

7-3. BL in Figure 7-3 stands for base length, which means the total wheelbase length of the truck (distance from the front axle to the trailing axle).

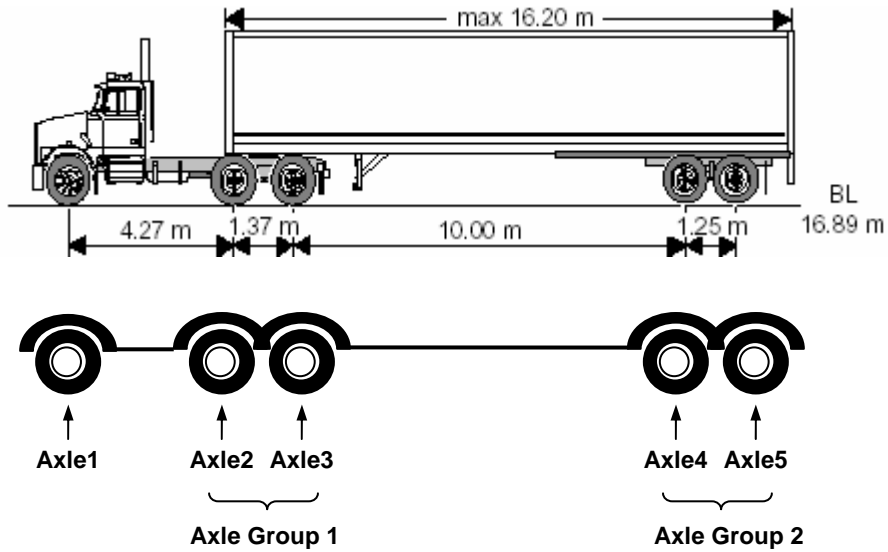


Figure 7-3: The Selected Vehicle and the Axle Group.

Table 7-1 and Table 7-2 show the axle static loads recorded by the bending plate of the existing DPS weigh station on August 11, 2004, and August 31, 2004.

Table 7-1: Axle Static Loads Recorded by the DPS Weigh Station on August 11, 2004.

Group No.	Static Load (lb)		
	Axle 1	Axle 2+3	Axle 4+5
1	11,560	29,260	35,900
2	10,540	16,960	12,600
3	11,860	34,920	32,000
4	10,760	28,500	30,460
5	11,500	27,860	28,840
6	10,320	12,680	9,840
7	10,320	17,920	16,960
8	10,040	17,100	12,840
9	10,300	30,420	38,820
10	10,460	17,820	13,620

Table 7-2: Vehicle Static Load Recorded by the DPS Weigh Station on August 31, 2004.

Group No.	Static Load (lb)		
	Axle 1	Axle 2+3	Axle 4+5
1	9,360	12,840	10,020
2	10,340	25,120	12,920
3	11,000	30,560	22,840
4	11,480	32,040	33,320
5	11,600	33,740	33,640
6	10,720	13,860	9,960
7	9,620	12,720	11,220
8	11,520	32,980	33,740
9	11,260	12,100	10,340
10	11,600	34,960	32,440
11	12,000	34,420	33,740
12	11,080	14,060	9,060
13	11,180	33,720	30,280
14	11,680	25,260	31,420
15	11,040	28,180	36,680
16	9,600	18,600	21,620
17	9,380	15,200	13,500

Figure 7-4 and Figure 7-5 show the plots of the original data generated by I-sense-14000 recorded on August 11, 2004. Only one grating with a center wavelength at 1539 nm was applied for this test. Figure 7-14 through Figure 7-30 show the plots of the original data generated by I-sense-14000 on August 31, 2004. Four gratings with a center wavelength of 1530 nm, 1539 nm, 1550 nm, and 1559 nm were all tested. For each plot, there are five peaks, which correspond to five axles on the selected vehicles.

Figure 7-31 shows the plot of the original data recorded on August 11th by the fiber optic detector developed for this project. The bandwidth of the current laser source used by the developed detector is only 5 nm wide. This limits the measurement range. When a load is applied to the grating, the center wavelength of the reflected wave will shift. The current laser source may not be able to cover it. If that is the case, the fiber optic detector could not detect the load on the FBG sensor.

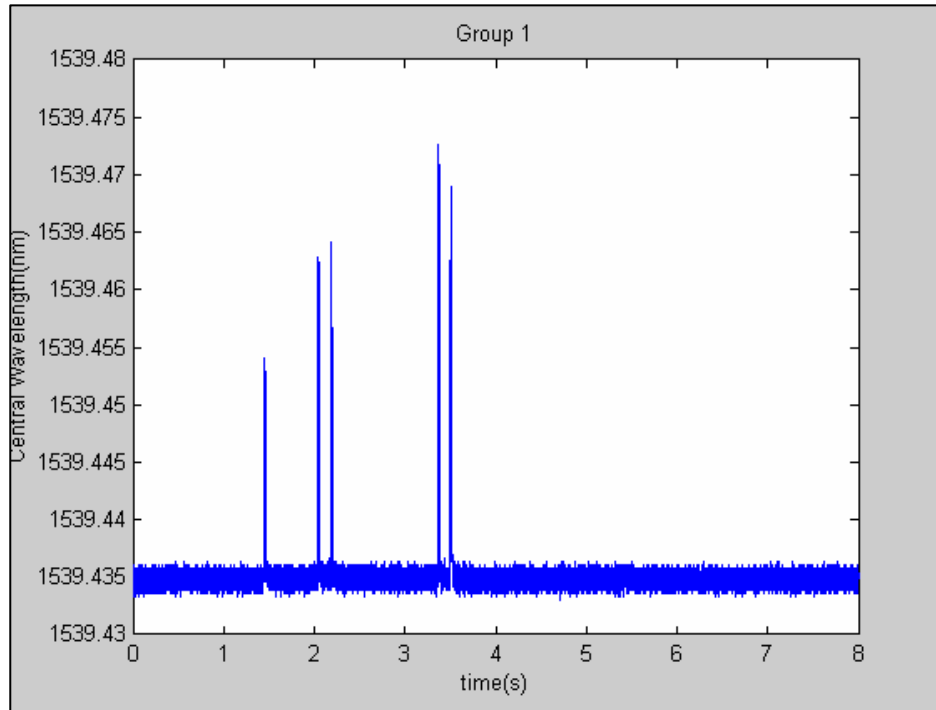


Figure 7-4: Plot of Measured Data for Field Test Group 1.
The test was performed on August 11, 2004.

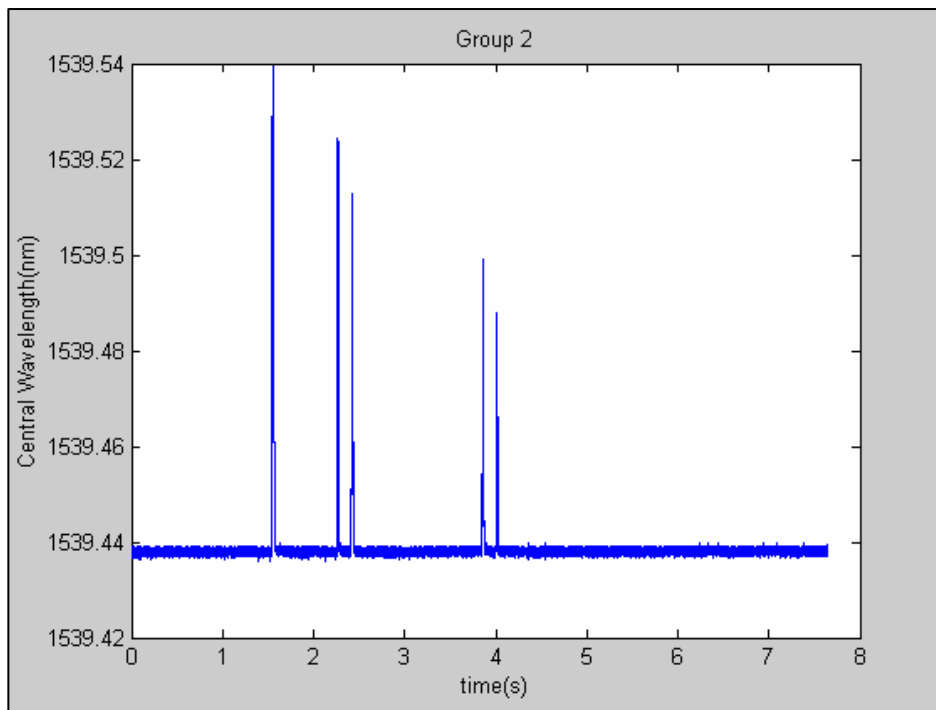


Figure 7-5: Plot of Measured Data for Field Test Group 2.
The test was performed on August 11, 2004.

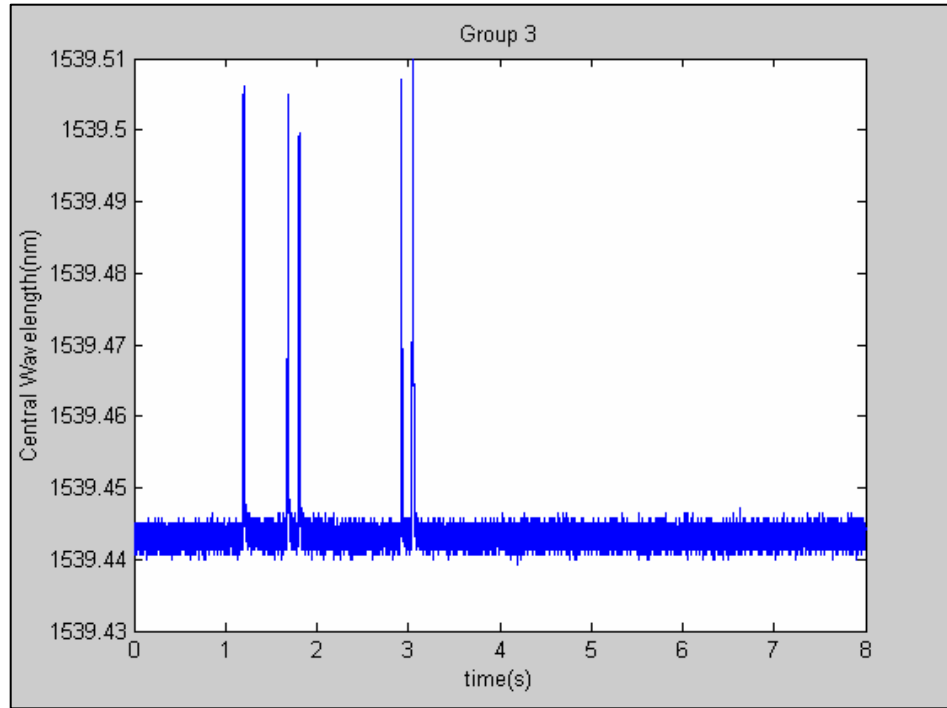


Figure 7-6: Plot of Measured Data for Field Test Group 3.
The test was performed on August 11, 2004.

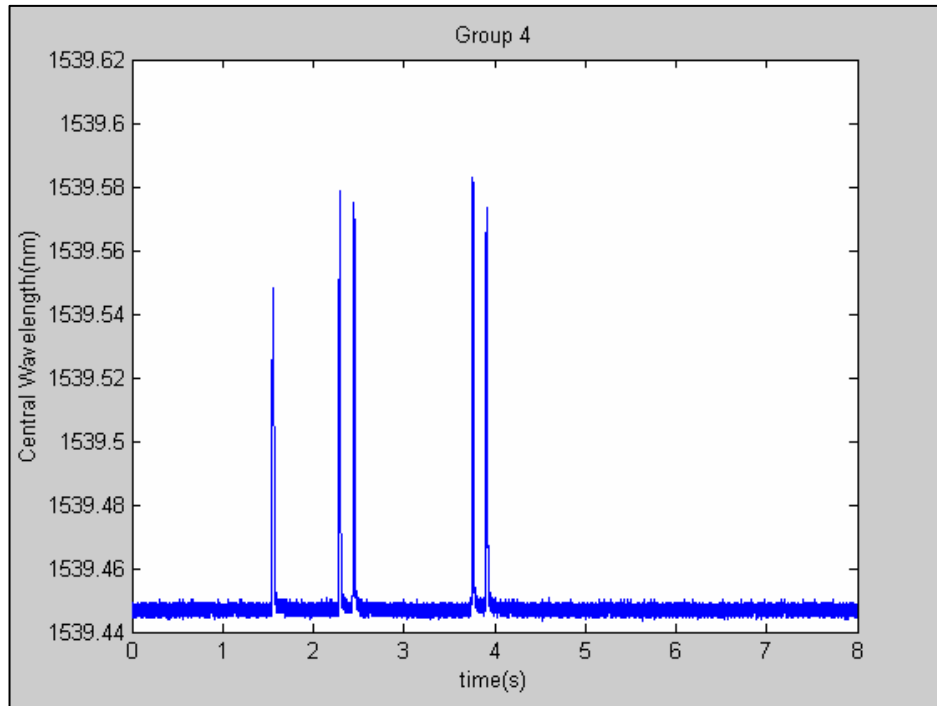


Figure 7-7: Plot of Measured Data for Field Test Group 4.
The test was performed on August 11, 2004.

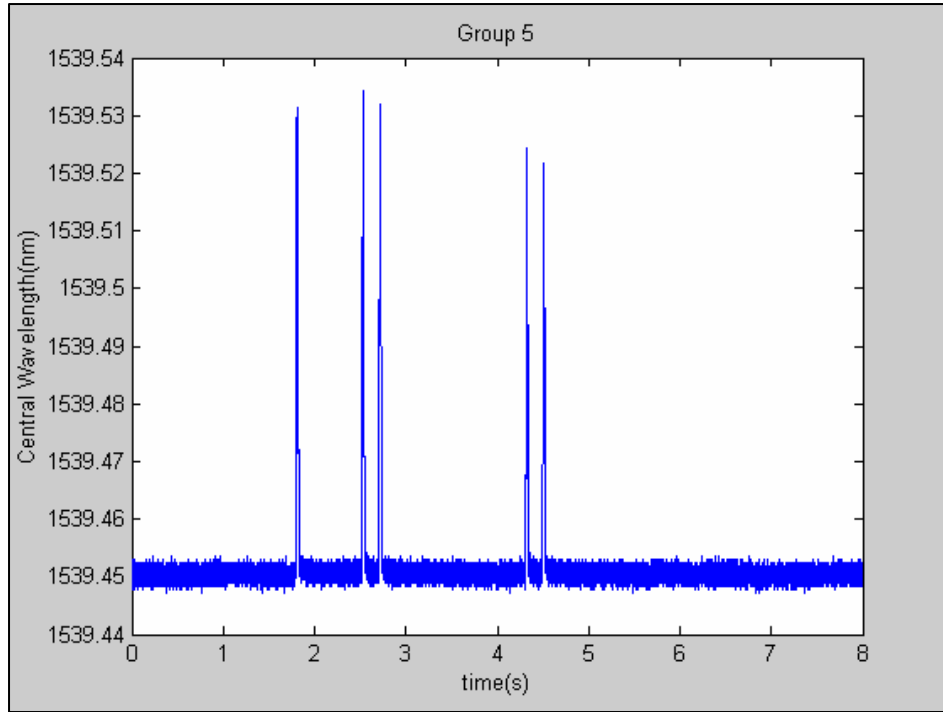


Figure 7-8: Plot of Measured Data for Field Test Group 5.
The test was performed on August 11, 2004.

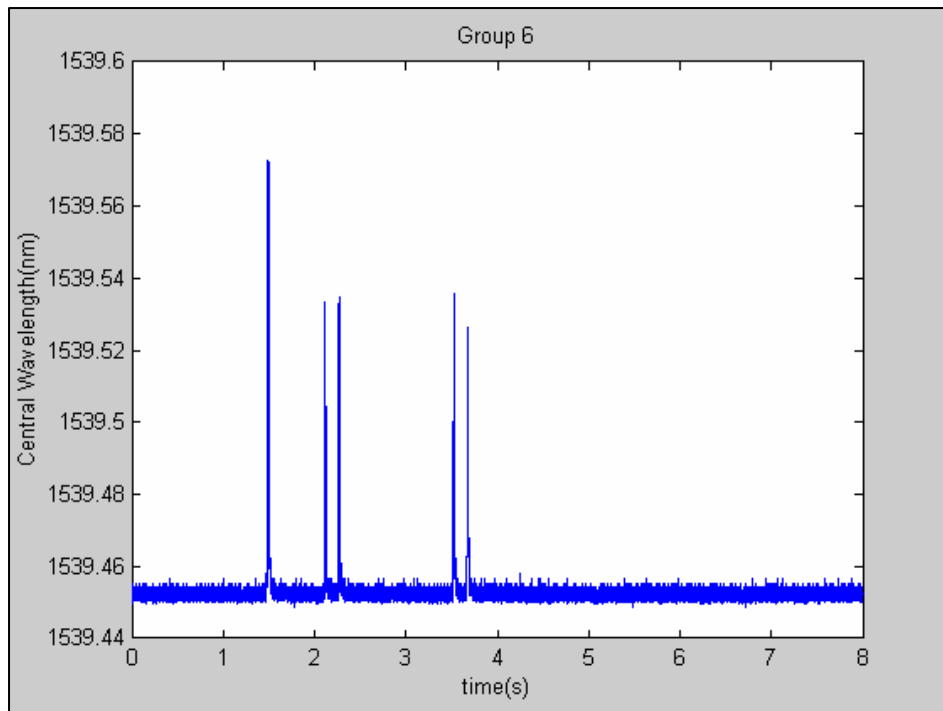


Figure 7-9: Plot of Measured Data for Field Test Group 6.
The test was performed on August 11, 2004.

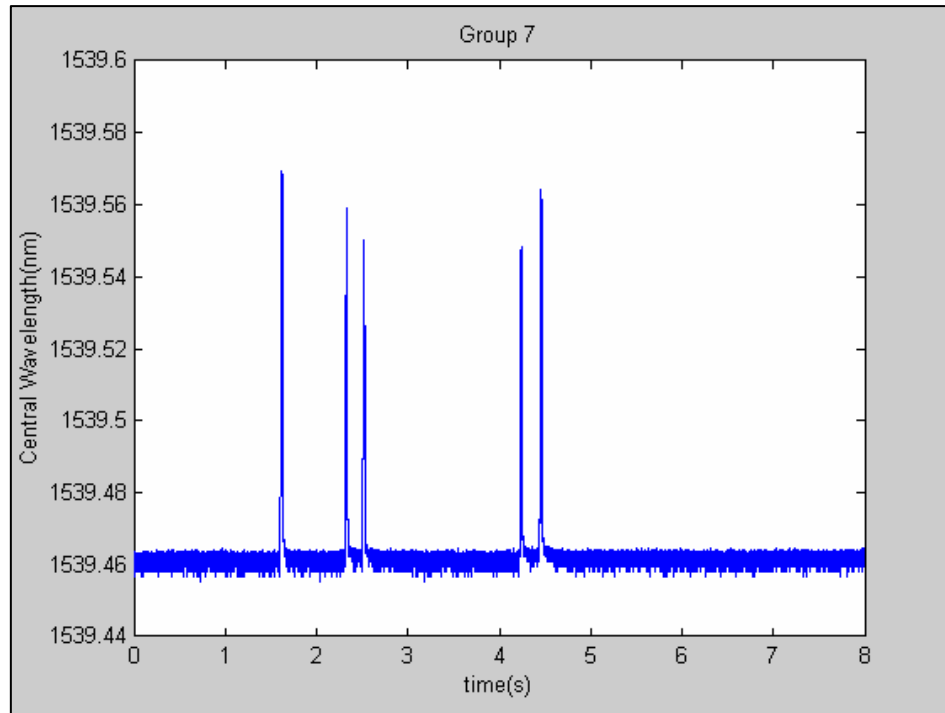


Figure 7-10: Plot of Measured Data for Field Test Group 7.
The test was performed on August 11, 2004.

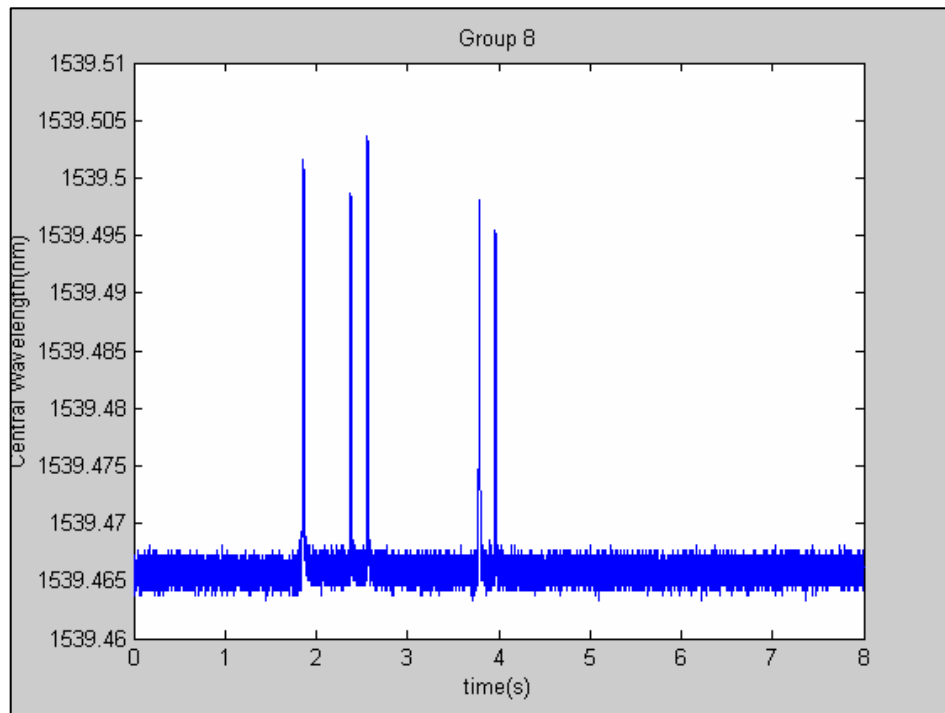


Figure 7-11: Plot of Measured Data for Field Test Group 8.
The test was performed on August 11, 2004.

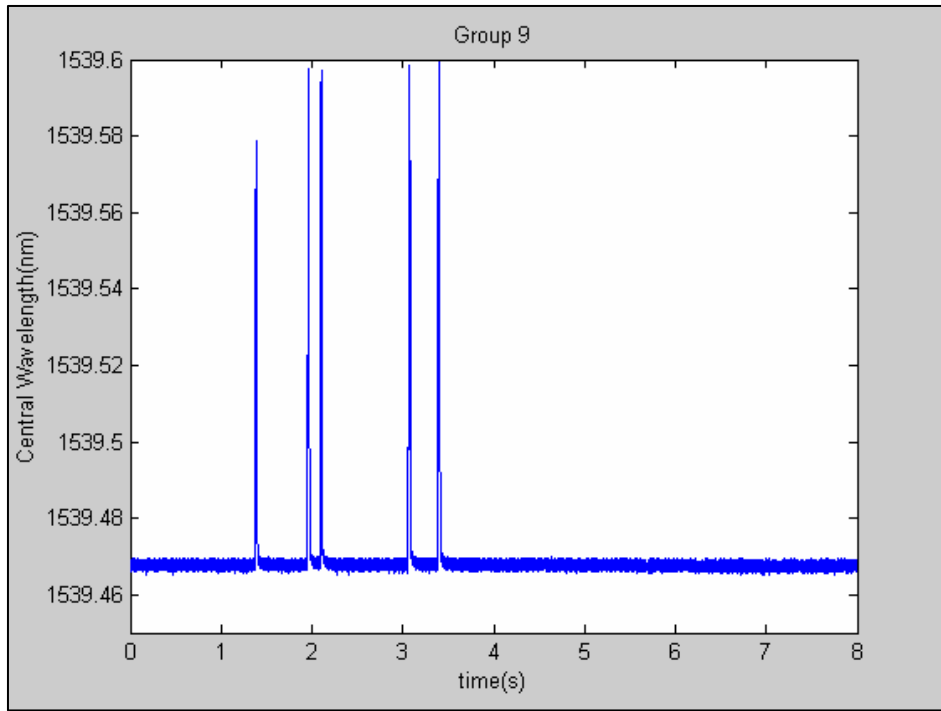


Figure 7-12: Plot of Measured Data for Field Test Group 9.
The test was performed on August 11, 2004.

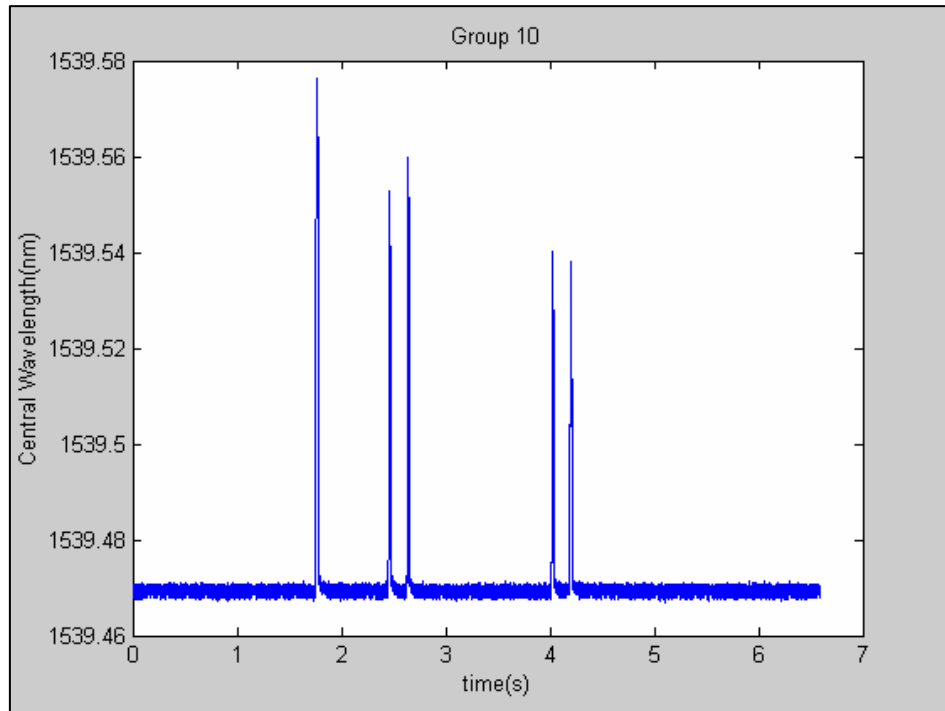


Figure 7-13: Plot of Measured Data for Field Test Group 10.
The test was performed on August 11, 2004.

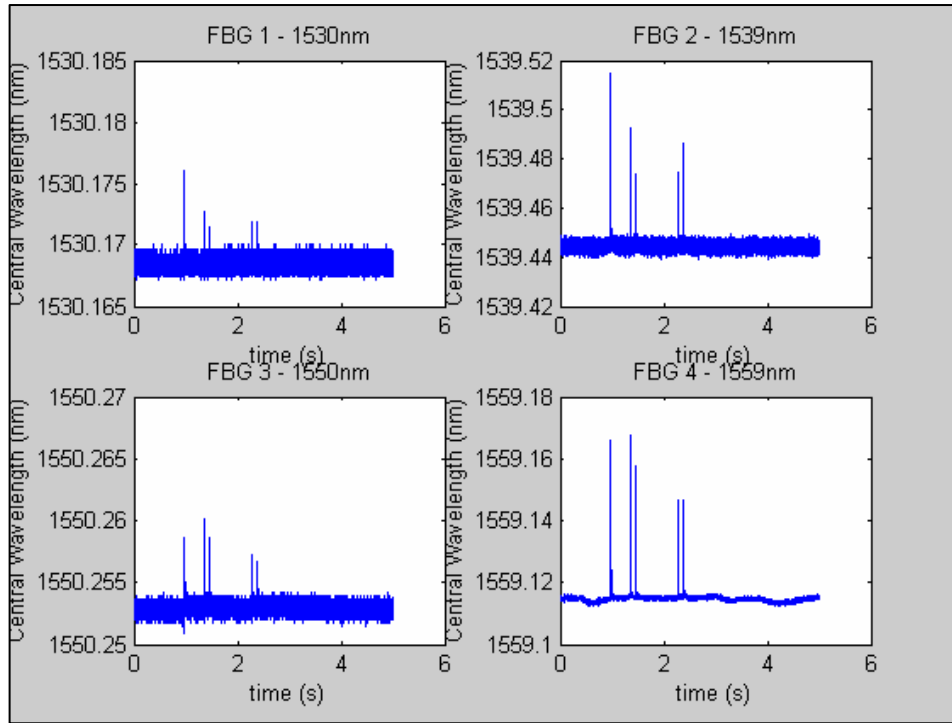


Figure 7-14: Plot of the Measured Data for Field Test Group 1. The test was performed on August 31, 2004.

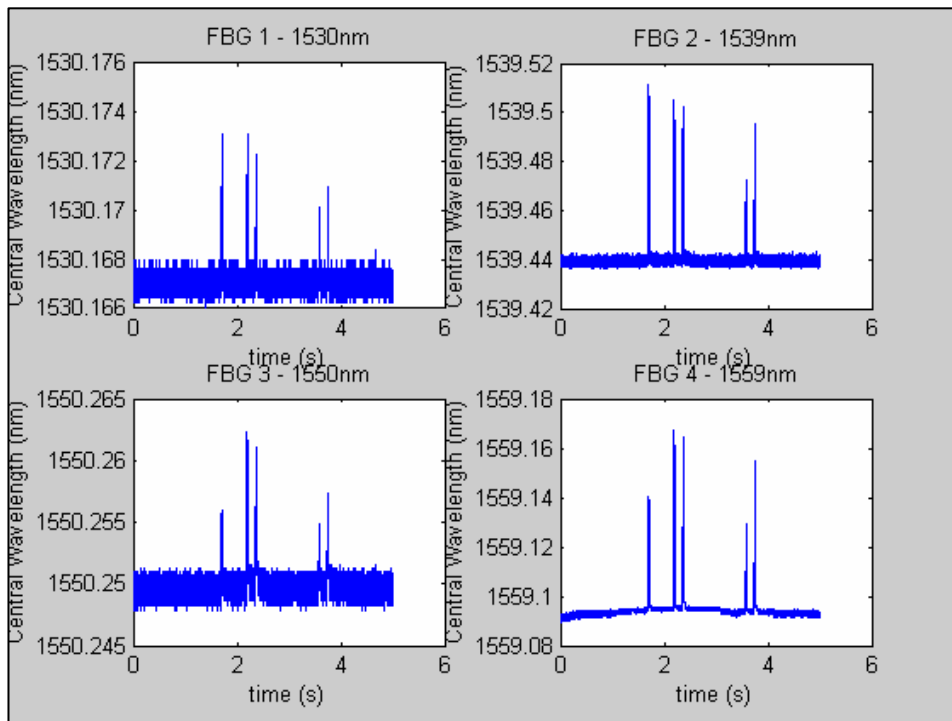


Figure 7-15: Plot of Measured Data for Field Test Group 2. The test was performed on August 31, 2004.

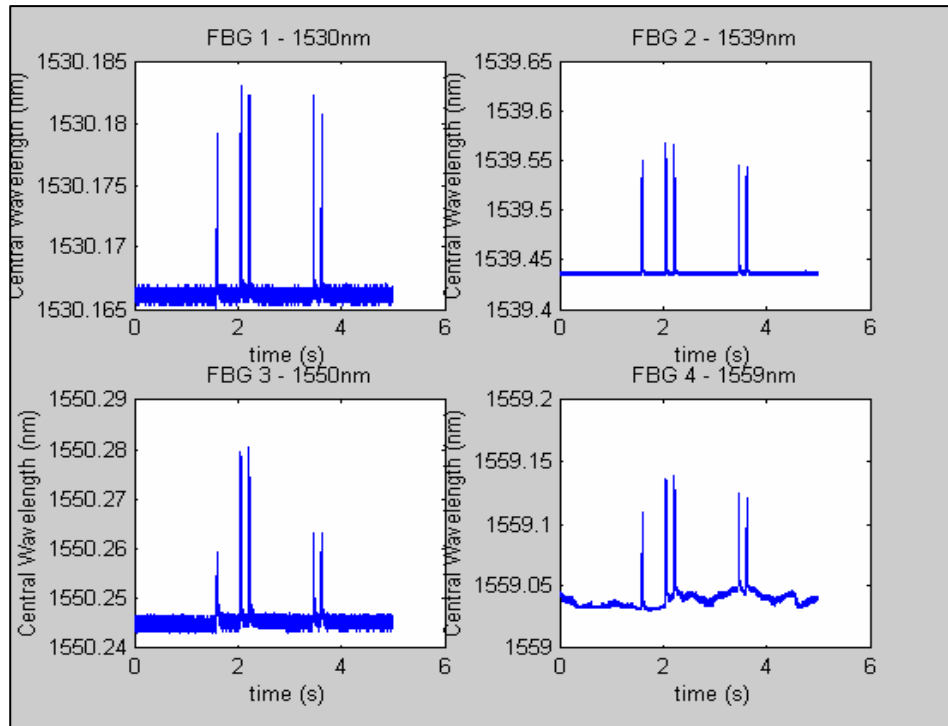


Figure 7-16: Plot of Measured Data for Field Test Group 3. The test was performed on August 31, 2004.

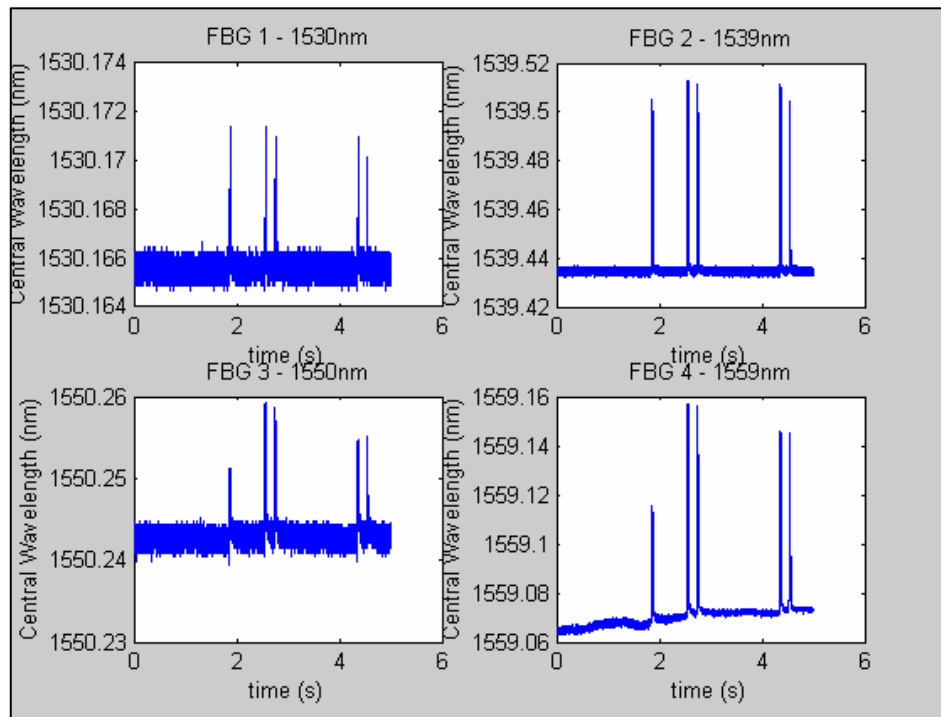


Figure 7-17: Plot of Measured Data for Field Test Group 4. The test was performed on August 31, 2004.

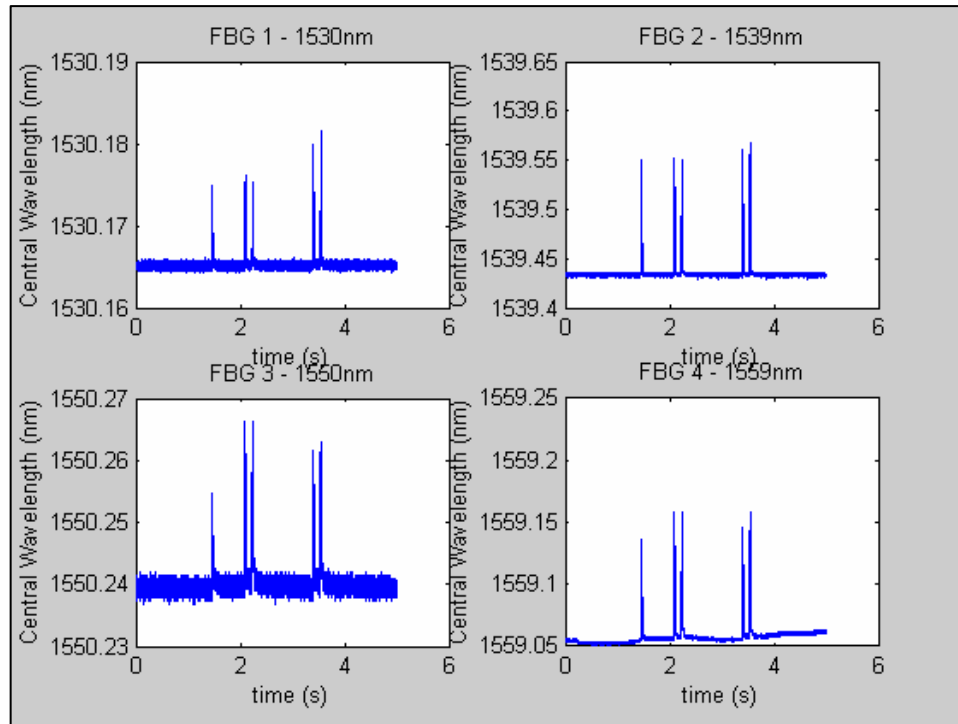


Figure 7-18: Plot of Measured Data for Field Test Group 5. The test was performed on August 31, 2004.

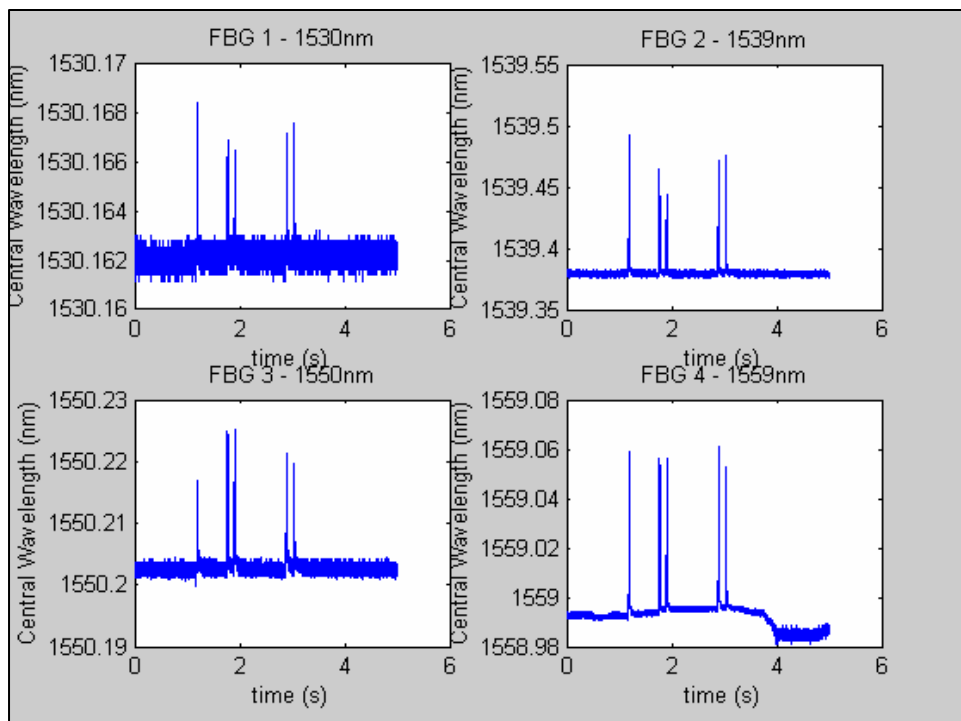


Figure 7-19: Plot of Measured Data for Field Test Group 6. The test was performed on August 31, 2004.

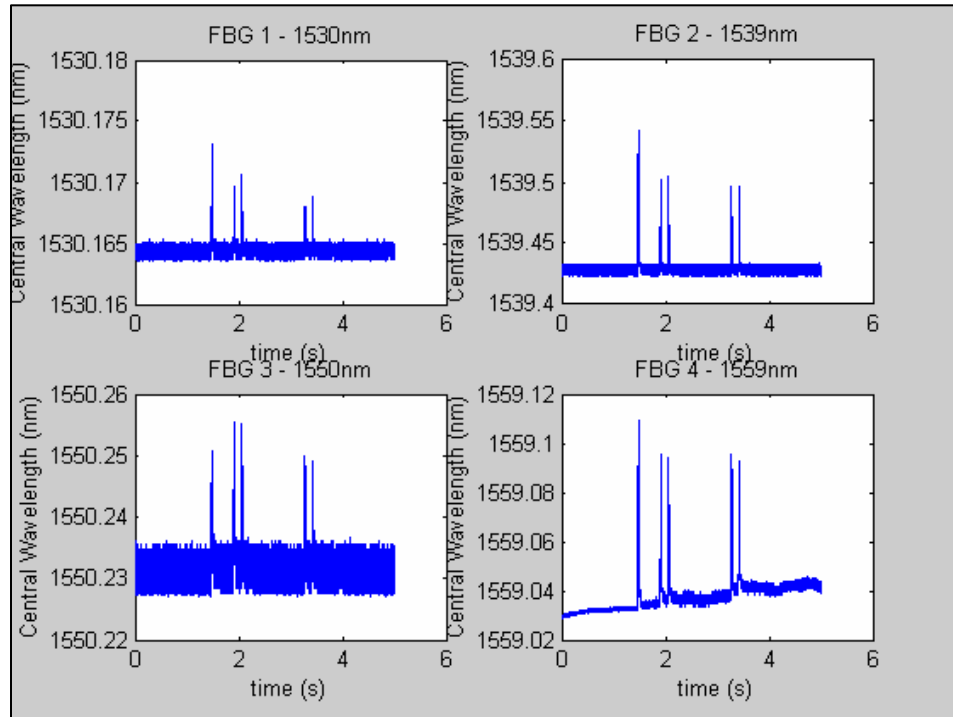


Figure 7-20: Plot of Measured Data for Field Test Group 7. The test was performed on August 31, 2004.

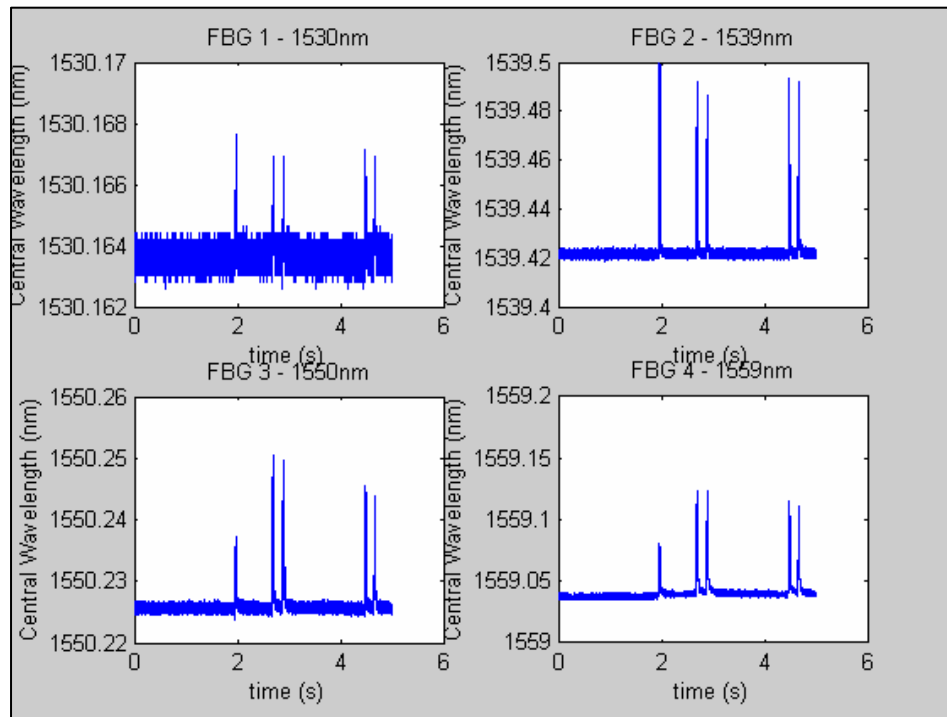


Figure 7-21: Plot of Measured Data for Field Test Group 8. The test was performed on August 31, 2004.

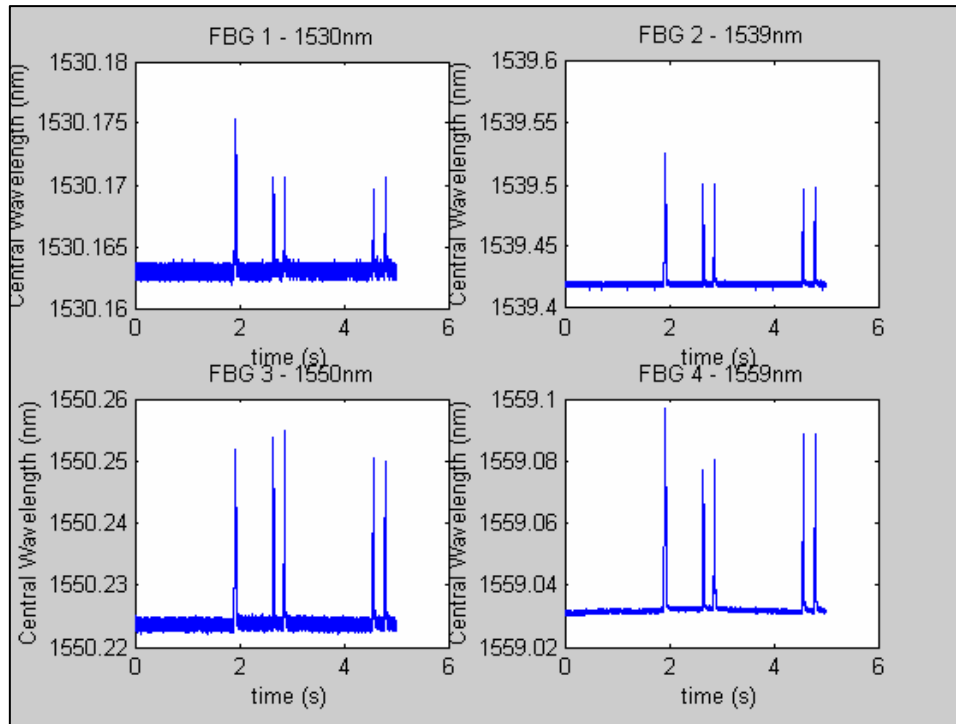


Figure 7-22: Plot of Measured Data for Field Test Group 9.
The test was performed on August 31, 2004.

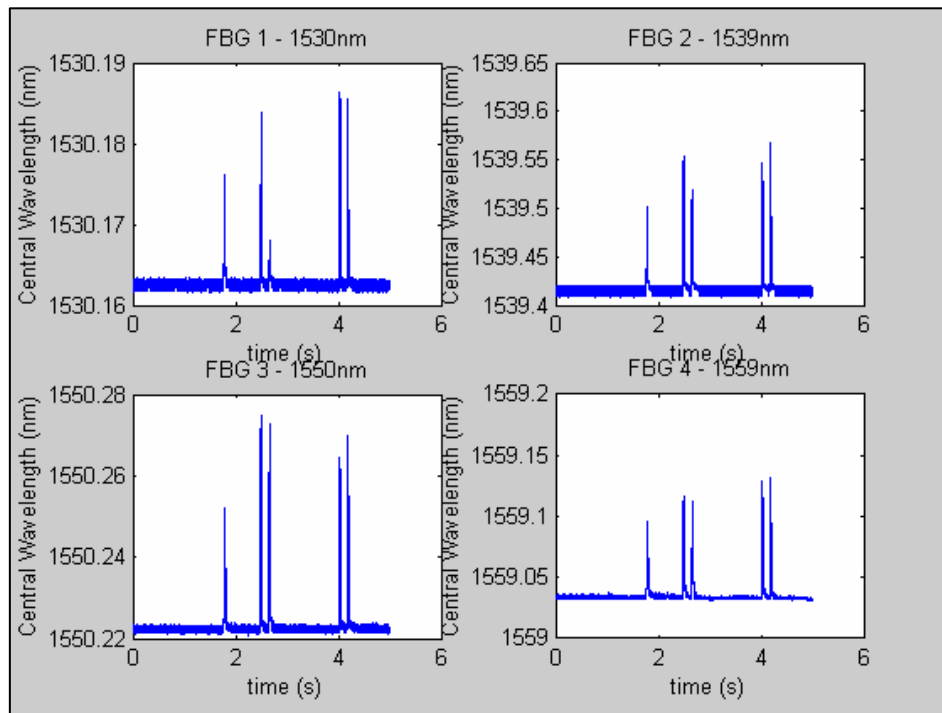


Figure 7-23: Plot of Measured Data for Field Test Group 10.
The test was performed on August 31, 2004.

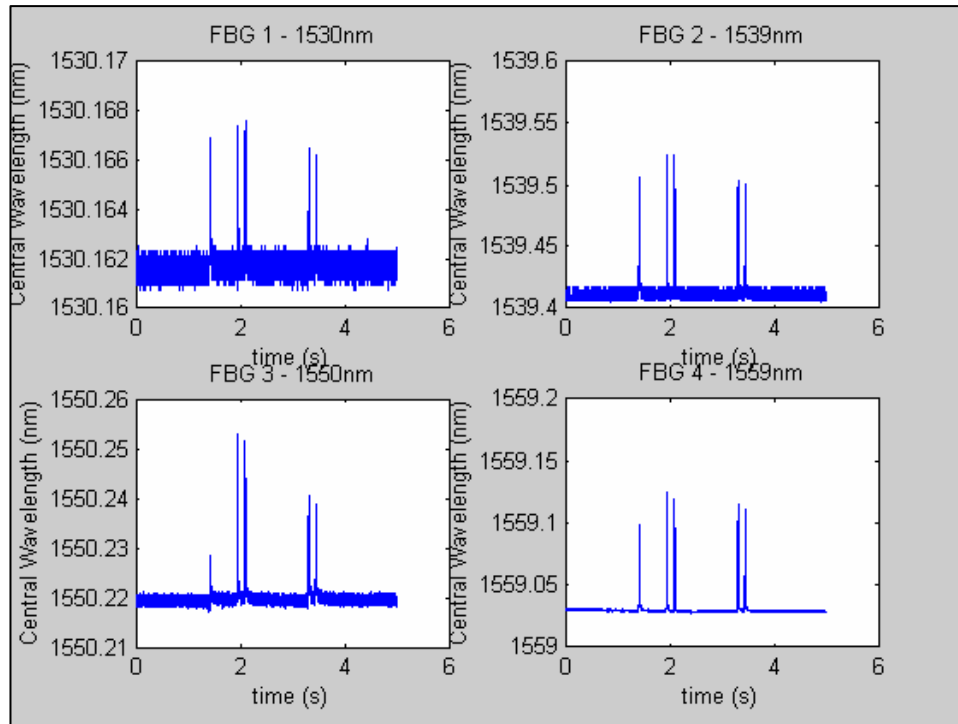


Figure 7-24: Plot of Measured Data for Field Test Group 11. The test was performed on August 31, 2004.

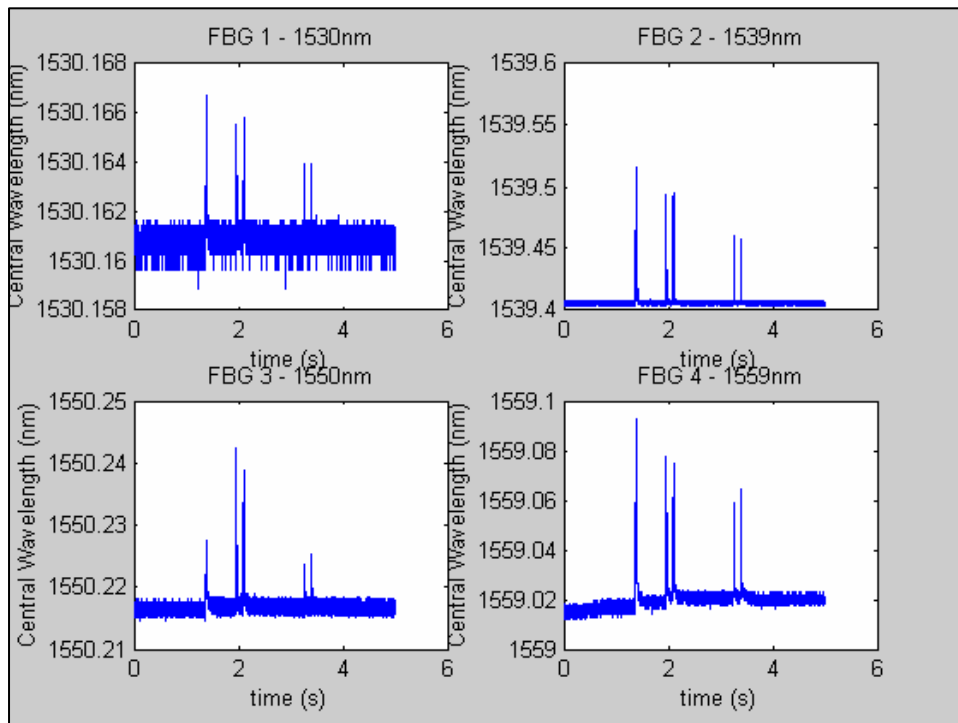


Figure 7-25: Plot of Measured Data for Field Test Group 12. The test was performed on August 31, 2004.

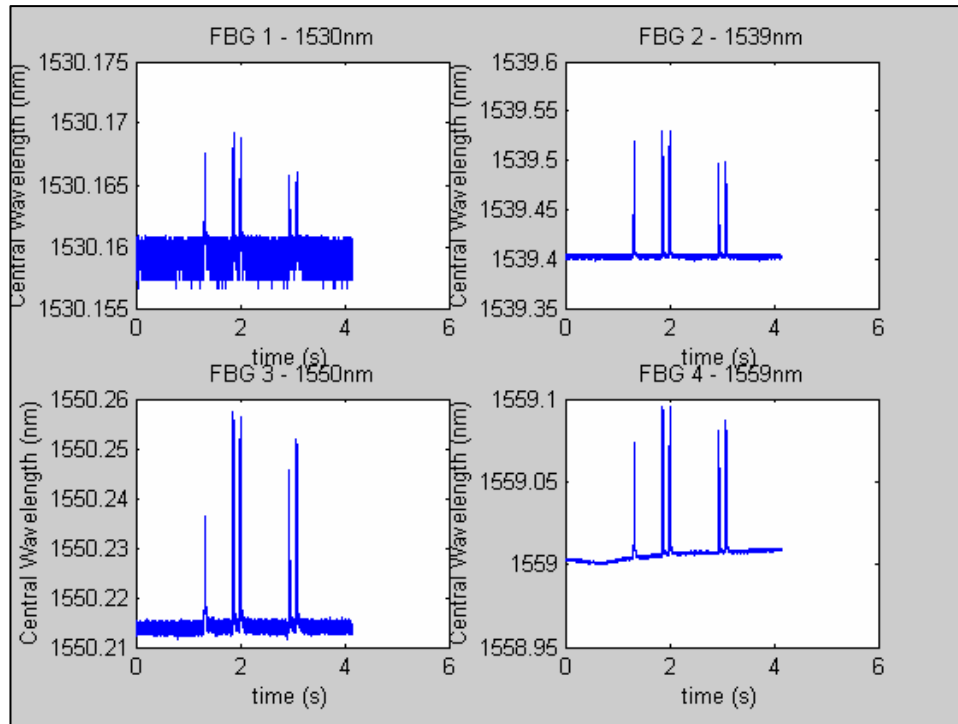


Figure 7-26: Plot of Measured Data for Field Test Group 13.
The test was performed on August 31, 2004.

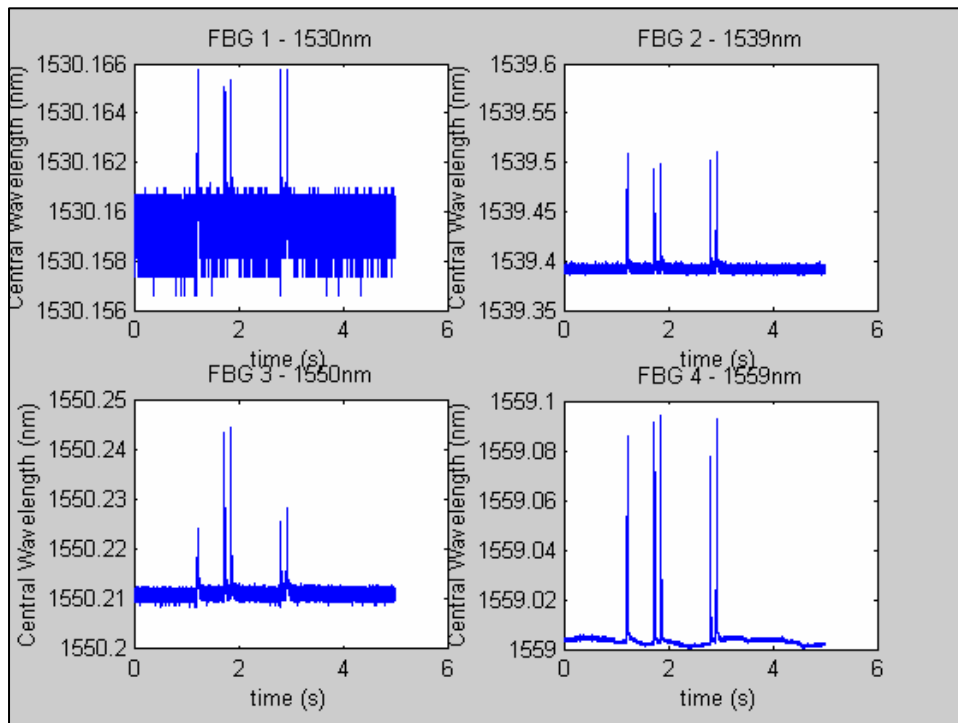


Figure 7-27: Plot of Measured Data for Field Test Group 14.
The test was performed on August 31, 2004.

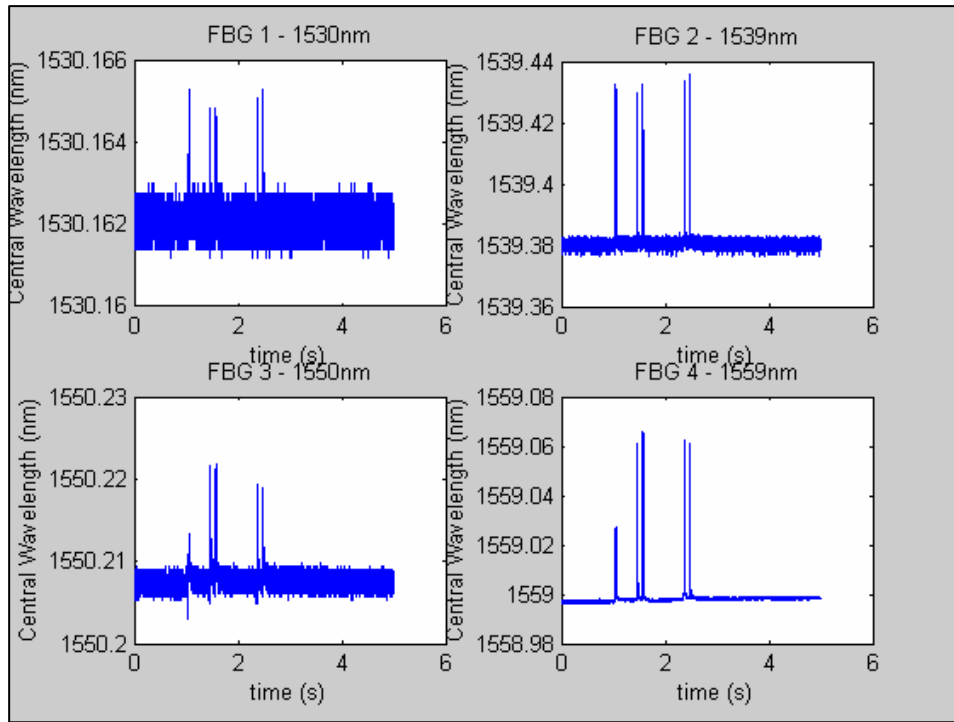


Figure 7-28: Plot of Measured Data for Field Test Group 15.
The test was performed on August 31, 2004.

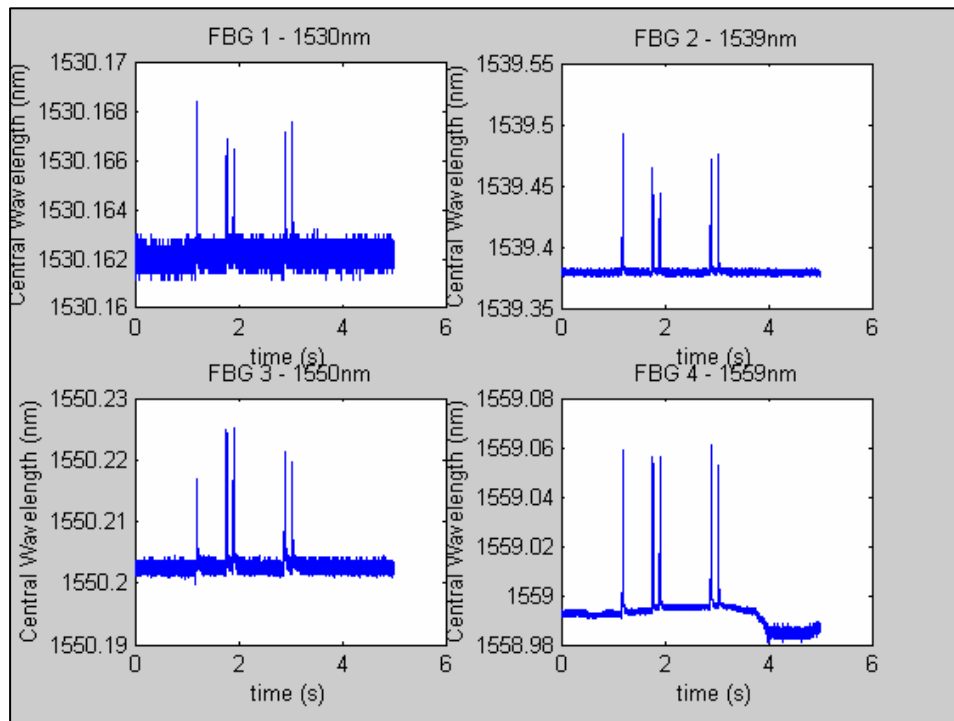


Figure 7-29: Plot of Measured Data for Field Test Group 16.
The test was performed on August 31, 2004.

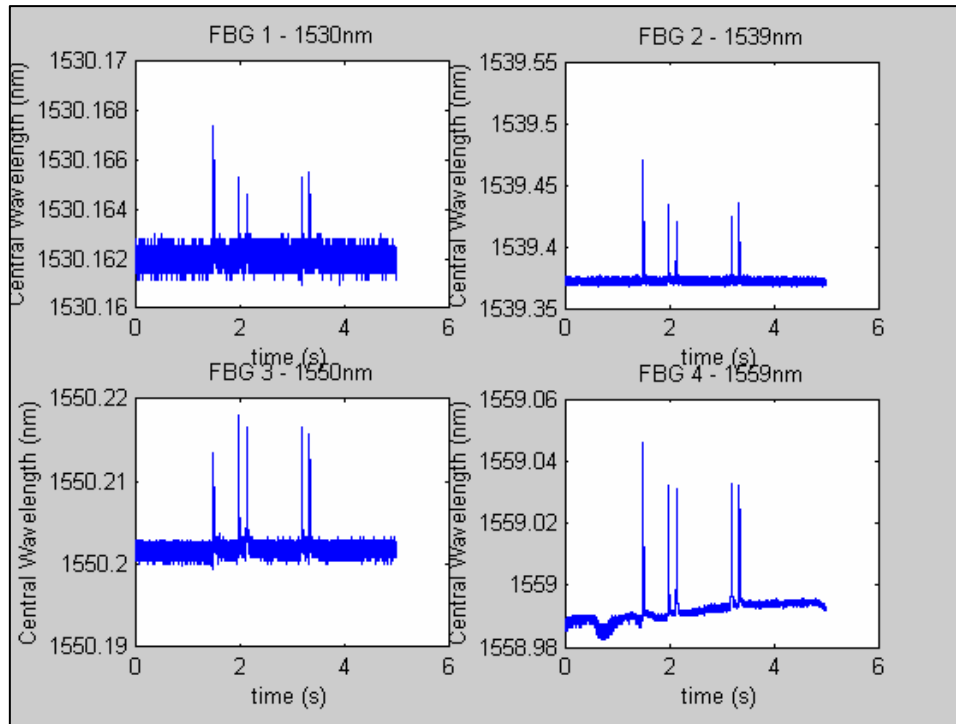


Figure 7-30: Plot of Measured Data for Field Test Group 17. The test was performed on August 31, 2004.

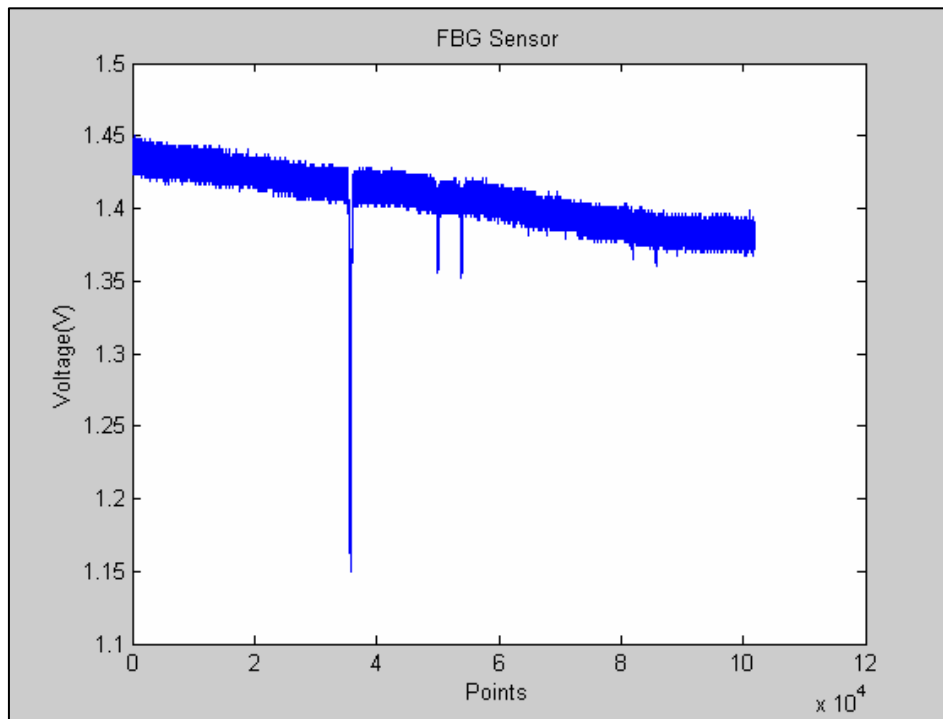


Figure 7-31: Plot of Measured Data Generated by the Designed Detector. The test was performed on August 11, 2004.

7.3 Data Analysis

7.3.1 Center Wavelength Shift

There are five data peaks for each plot of one field test group of one Bragg grating. Subtracting the base value from the peak value yields the center wavelength of the applied loads, as shown in [Figure 7-32](#).

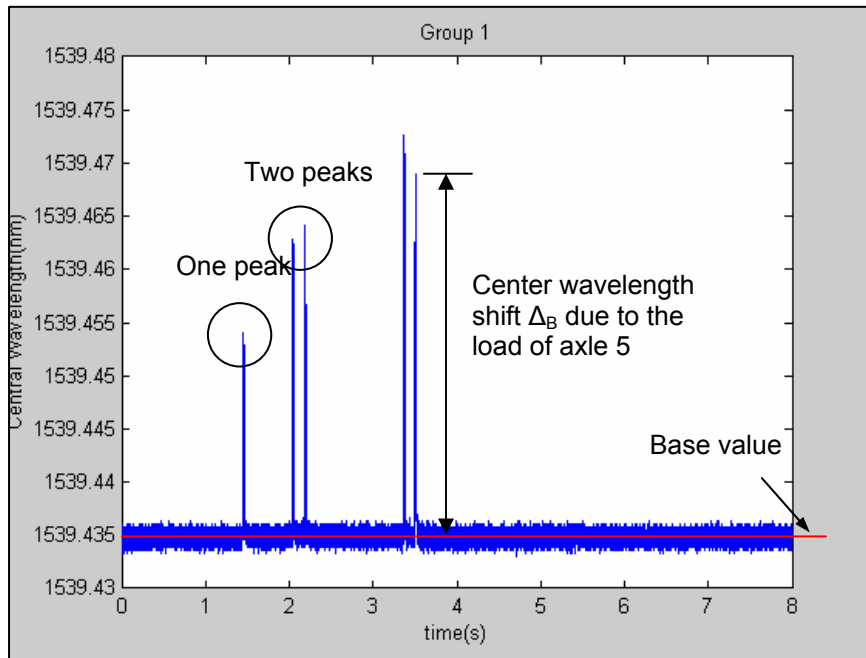


Figure 7-32: Peaks and Center Wavelength Shift.

For the field test conducted on August 11, 2004, [Table 7-3](#) shows the center wavelength shifts for each axle group, where column “Axle 2+3” is simply generated by adding the center wavelength shifts of the loads of axle two and axle three together. Column “Axle 4+5” is generated by adding the center wavelength shifts of the loads of axle four and axle five.

Table 7-3: Center Wavelength Shifts Calculated from Field Test Data Obtained on August 11, 2004.

Group No.	Center Wavelength Shift		
	Axle 1	Axle 2+3	Axle 4+5
1	0.017379773480	0.054051306510	0.069264738810
2	0.099150512900	0.155346039780	0.104515716330
3	0.060915415500	0.115007579800	0.125452072360
4	0.098672026730	0.254032201510	0.255938910110
5	0.078654999110	0.160113574210	0.138172680860
6	0.118512697960	0.158804792870	0.151188003360
7	0.105251160540	0.179990269311	0.183106526150
8	0.034168440710	0.068334034380	0.059576324810
9	0.107878915450	0.253645284940	0.257954259260
10	0.104442007360	0.167812976790	0.134207327910

For the field test conducted on August 31st, [Table 7-4](#) shows the center wavelength shifts for each axle group. Since four gratings were applied, the corresponding center wavelength shifts of each axle for each grating are added together.

Table 7-4: Center wavelength shift calculated from field test data obtained on August 31, 2004

Group No.	Center Wavelength Shift		
	Axle 1	Axle 2+3	Axle 4+5
1	0.125892641599	0.177689819950	0.128746479189
2	0.121198975520	0.289175082300	0.190617205490
3	0.198207256831	0.521638088680	0.421144283691
4	0.119018510029	0.348616927160	0.308099939330
5	0.208248011710	0.484129243061	0.494265445031
6	0.203217342590	0.286488043179	0.187367966730
7	0.197898271170	0.308019597611	0.279322704009
8	0.121782764030	0.331693100059	0.307082813570
9	0.203056832450	0.311874618050	0.315821932749
10	0.176767511331	0.494951518640	0.581476132680
11	0.169777888630	0.473159935080	0.382515482410
12	0.191285067200	0.330687838030	0.190554217379
13	0.194901689050	0.507988396572	0.402744504730
14	0.207401261800	0.441140893970	0.414734318769
15	0.079123056370	0.238795893210	0.246202982280
16	0.189037632729	0.305647523359	0.347040980749
17	0.159601969471	0.210216306430	0.216368110150

7.3.2 Noise Floor

Like any other analog circuit application, thermal noise and other interference exist in the circuits. There is also another source of noise, the opto-electronic components (LD driver and PD receiver). The noise level is the most important factor that will affect the accuracy of the measurement. From [Figure 7-34](#), it can be seen that the maximum noise level is about 0.027 nm, and the constant noise level is about 0.0011 nm.

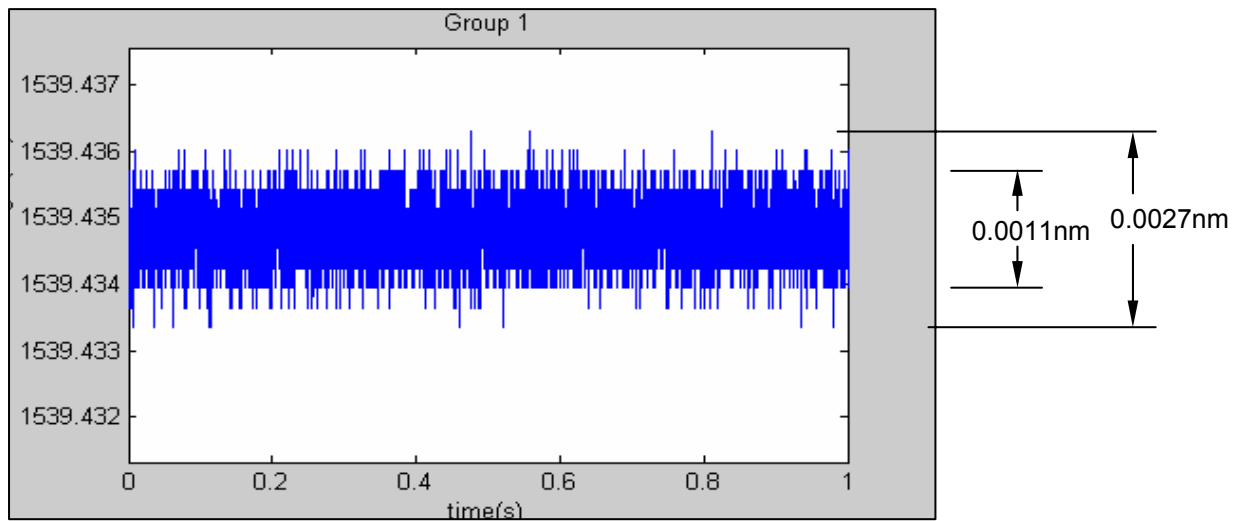


Figure 7-34: Noise floor

The maximum noise level of each field test data is shown in [Figure 7-35](#) and [Figure 7-36](#).

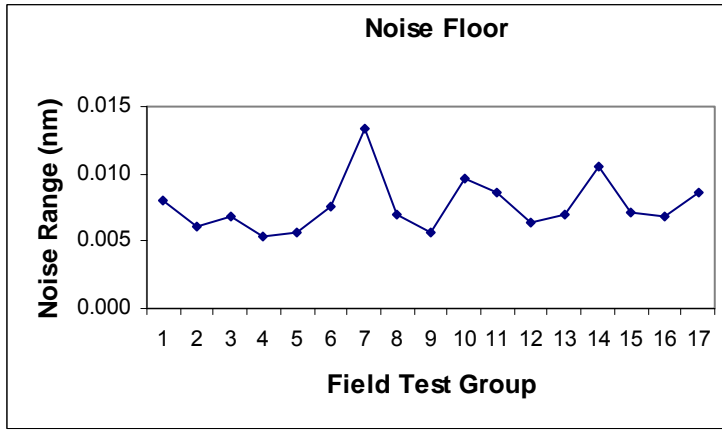


Figure 7-35: Maximum Noise Level of Field Test Data Obtained on August 11, 2004.

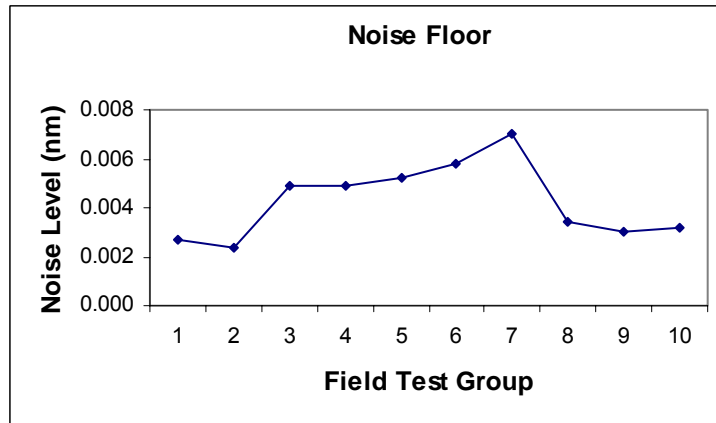


Figure 7-36: Maximum Noise Level of Field Test Data Obtained on August 31, 2004.

7.3.3 Measurement Error

The measurement error was calculated by

$$error = \frac{K \cdot V - W_s}{W_s} \times 100\%, \quad (7-1)$$

where W_s is the static weight of an axle/axle group, K is a calibration constant and V is the output of the FBG sensor system. The results are shown in [Table 7-5](#) and [Table 7-6](#) and plotted in [Figure 7-37](#) and [Figure 7-38](#).

Table 7-5: Measurement Error of Field Test Data Obtained on August 11, 2004.

Group No.	Factor K	Error (%)		
		Axle 1	Axle 2+3	Axle 4+5
1	574926.5869	-13.563	6.205	10.925
2	112011.5603	5.370	2.598	-7.088
3	251135.2849	28.988	-17.290	-1.545
4	113417.1355	4.006	1.093	-4.702
5	176311.3137	20.589	1.327	-15.529
6	77336.7541	-11.188	-3.143	18.825
7	96745.2639	-1.332	-2.828	4.450
8	253200.5303	-13.830	1.183	17.483
9	121966.8259	27.744	1.697	-18.955
10	102608.5623	2.454	-3.372	1.107

Table 7-6: Measurement Error of Field Test Data Obtained on August 31, 2004.

Group No.	Factor K	Error (%)		
		Axle 1	Axle 2+3	Axle 4+5
1	74812.39546	0.623	3.531	-3.874
2	79987.28734	-6.244	-7.921	18.010
3	56105.11246	1.095	-4.232	3.452
4	98836.11608	2.468	7.540	-8.609
5	64485.18034	15.766	-7.471	-5.253
6	51429.27266	-2.506	6.305	-3.251
7	43358.50020	-10.805	4.994	7.941
8	101298.85678	7.087	1.880	-7.803
9	42330.02215	-23.664	9.105	29.292
10	64015.04912	-2.450	-9.370	14.745
11	77210.37367	9.238	6.138	-12.465
12	49328.99405	-14.838	16.021	3.751
13	66308.62130	15.596	-0.107	-11.805
14	63111.97203	12.068	10.219	-16.694
15	135506.99471	-2.883	14.828	-9.045
16	57978.68936	14.168	-4.726	-6.933
17	64490.44898	9.731	-10.810	3.361

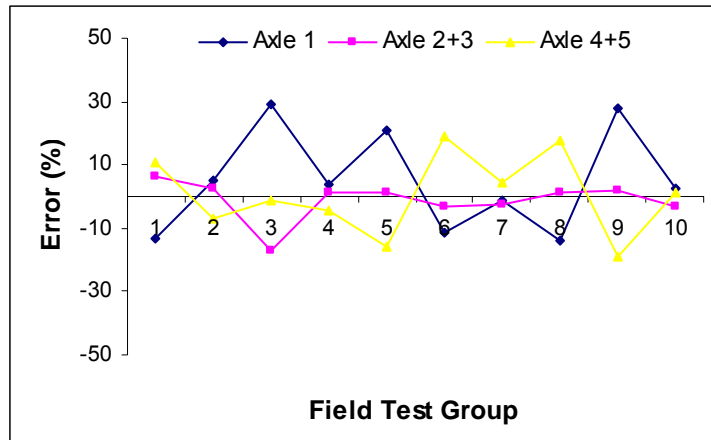


Figure 7-37: Plot of Error for Field Test Data Obtained on August 11, 2004.

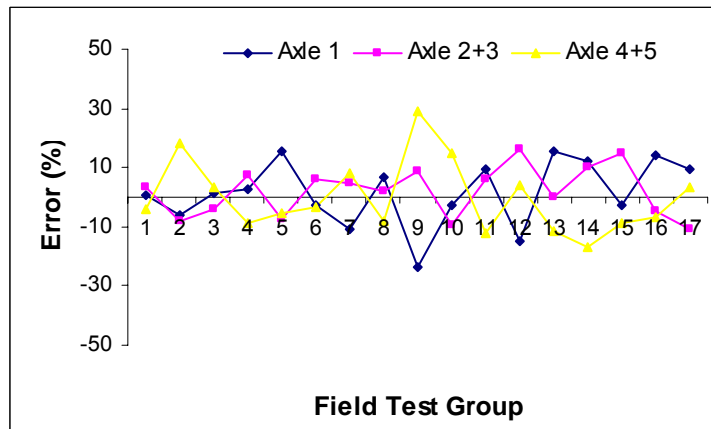


Figure 7-38: Plot of Error for Field Test Data Obtained on August 31, 2004.

For each test group, a different calibration factor, K , is currently used for error calculation, because vehicles touch different sensor areas at different times. Since the applied FBG sensors do not cover the whole lane, some vehicles did not even touch the sensor area during tests. This is the main reason for the measurement error in addition to the effects of the noise. The average error of the second field test data is less than the error of the first field test data because the sensing area was expanded. Meanwhile,

vehicle speed and pavement temperature also affect the results. Neither aspect is considered in current data processing.

7.4 Summary

With further refinement, the FBG sensor shows potential to be a very good candidate for future WIM systems. Compared to piezoelectric sensors, FBG sensors offer a simpler and more explicit load determination algorithm, and the lifetime of the sensors is longer. However, it is necessary to build a sensor holder for a FBG sensor. The comparison of different WIM sensor features is shown in [Table 7-7](#).

For the current FBG WIM system, the vehicle has to contact the same position of the sensor area to obtain accurate results. This is a limitation in the current FBG sensor holder. Meanwhile, the bandwidth of the current laser source used by the developed detector is not wide enough, which limits the measurement range.

Table 7-7: Comparison Table of Different WIM Sensors.

	Piezoelectric	Bending Plate	Load Cell	FBG
Accuracy	Low	Medium	High	According to the sensor holder
Expected Life	Short	Medium	Long	Long
Sensor Holder	No	No	No	Yes
Installation	Easy & Low Cost	Hard & High Cost	Hard & Very High Cost	According to the sensor holder & medium cost

CHAPTER 8: LAB TEST RESULTS OF MICROWAVE WIM SENSOR

8.1 Test Setup

An innovative sensor based on microwave cavity theory was developed by the researchers as part of this study. To record the data, one PCI version data acquisition card with sampling rate as high as 5 MSPS is used to do the sampling on the output signal of the power detector. To ensure the same start point for data acquisition was used, a synchronizing signal was used as the external trigger for the DAQ card. Although the 5 MSPS sampling rate is fast, only 320 points can be acquired during one sweep as shown in Figure 8-1. The points used to detect the resonant frequency are too few. So, interpolation and low pass filter (LPF) are effective ways to improve the measurement accuracy. And among those resonant frequencies, the one with maximum peak is chosen for detection.

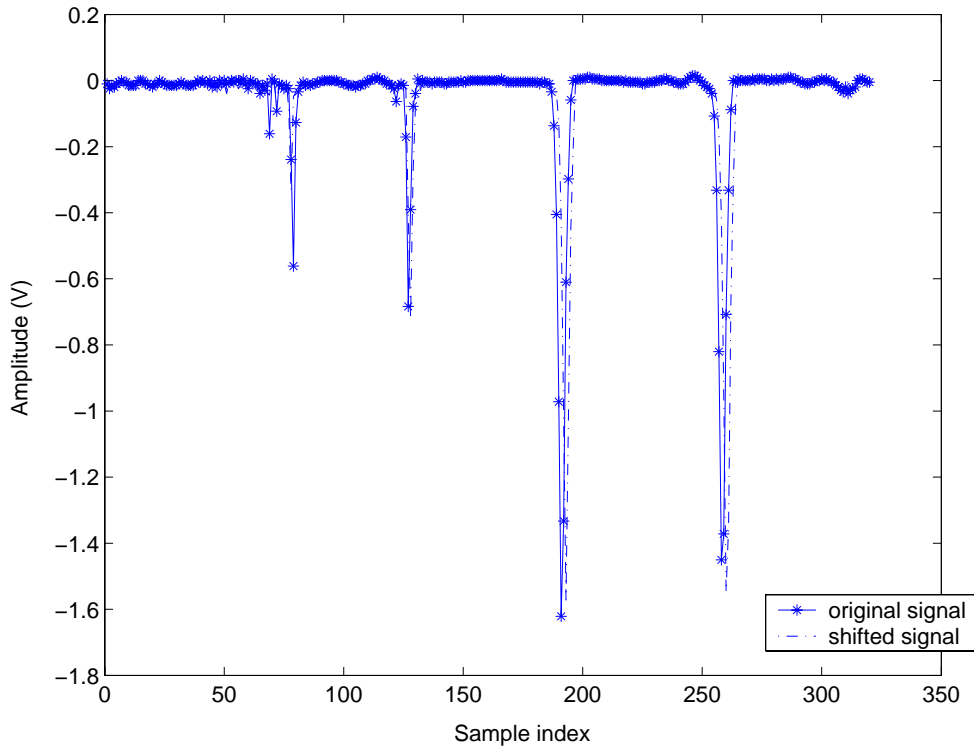
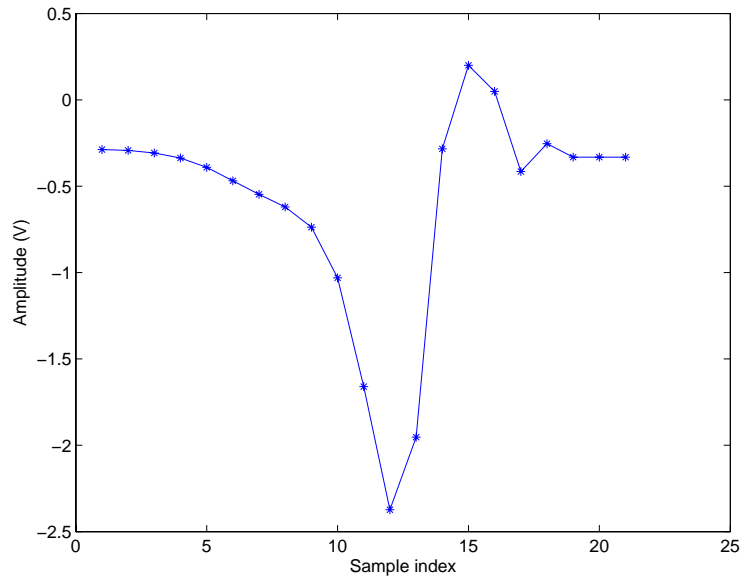
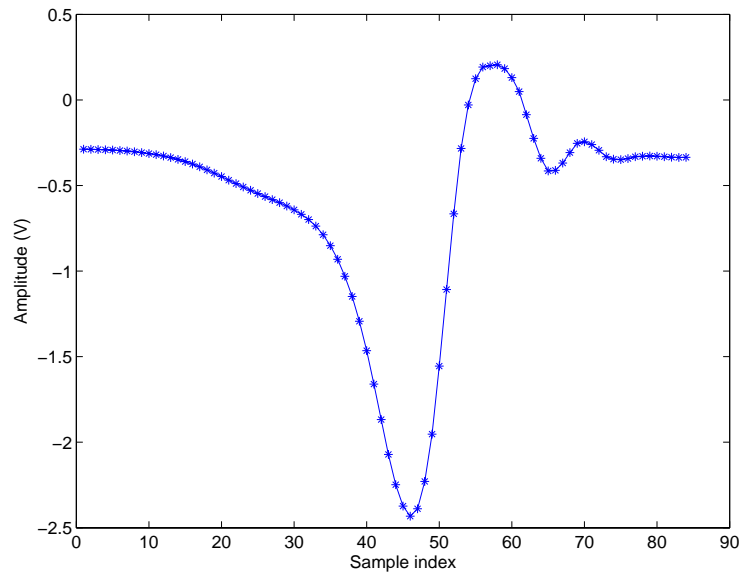


Figure 8-1: Data Acquired during One Sweep by DAQ Card.

An example of interpolation and LPF processing for the signal of power detector's output is shown in Figure 8-2. It is easy to detect the signal's peak position after the processing.



(a)



(b)

Figure 8-2: (a) Signal of Power Detector's Output Before Interpolation and LPF Processing; (b) Signal of Power Detector's Output after Interpolation and LPF Processing.

The test setup is shown in [Figure 8-3](#). The output of the circuit is fed to the computer with a data acquisition card installed. Data is recorded under a 5-Mhz sampling rate. There are eleven test points along the sensor to evaluate uniformity and linearity. The load was applied to each test point by a loading machine, with loads ranging from about 100–300 lbs., as shown in [Table 8-1](#). The data was then recorded and processed to extract the shifted sample points. Errors were calculated and compared among these 11 test points.

Table 8-1: Load Applied on Sensor.

Position	Load (lb)							
	1	106	148	166	186	226	246	286
2	109	150	170	192	250	270	290	310
3	100	120	164	200	240	264	282	302
4	100	140	160	180	220	262	280	300
5	100	120	142	182	242	260	282	300
6	102	120	140	184	240	260	280	300
7	100	140	160	200	220	260	280	300
8	100	120	140	182	240	260	280	300
9	100	120	162	184	240	260	282	300
10	100	120	140	180	202	240	280	302
11	100	124	162	182	220	260	280	302

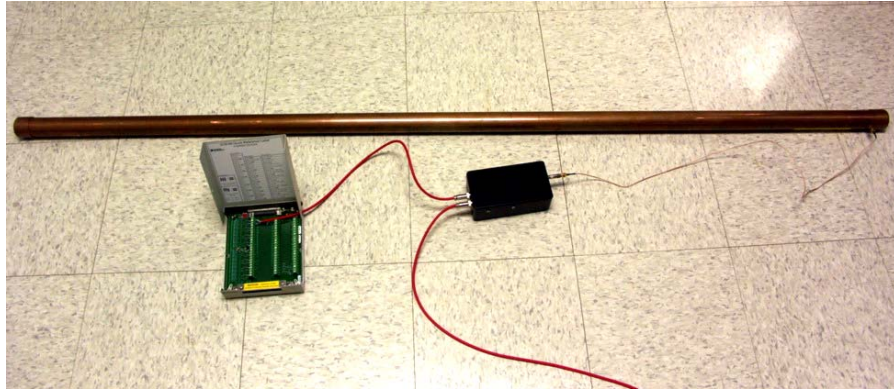


Figure 8-3: Test Setup.

8.2 Uniformity and Linearity Test

Before reviewing all of the test results, the results at test position 1 will be discussed. According to the acquired data, 10 points are interpolated between two points of the original data. LPF is also applied to the data. Then, the shifted sample points are used to measure the change of load. As shown in [Figure 8-4](#), the measured data and the corresponding linear fitted curve ($y = 0.10x + 113.89$) are plotted. If the linear fitted curve is assumed to be the accurate value, the linearity of sensor's output can be calculated. The

result is shown in [Figure 8-5](#). It is easy to find the linearity of the sensor's output at position 1, as it is within +/-1%.

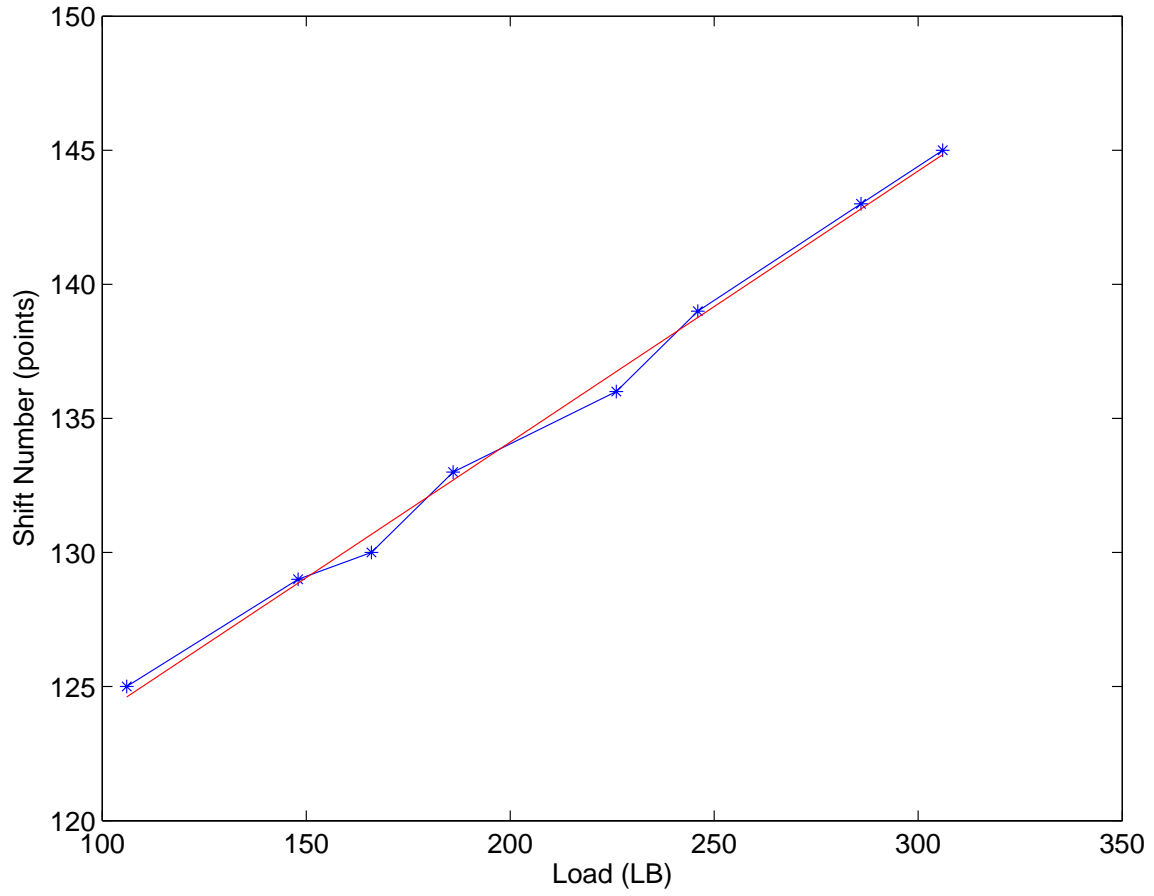


Figure 8-4: Measured Data at Position 1.

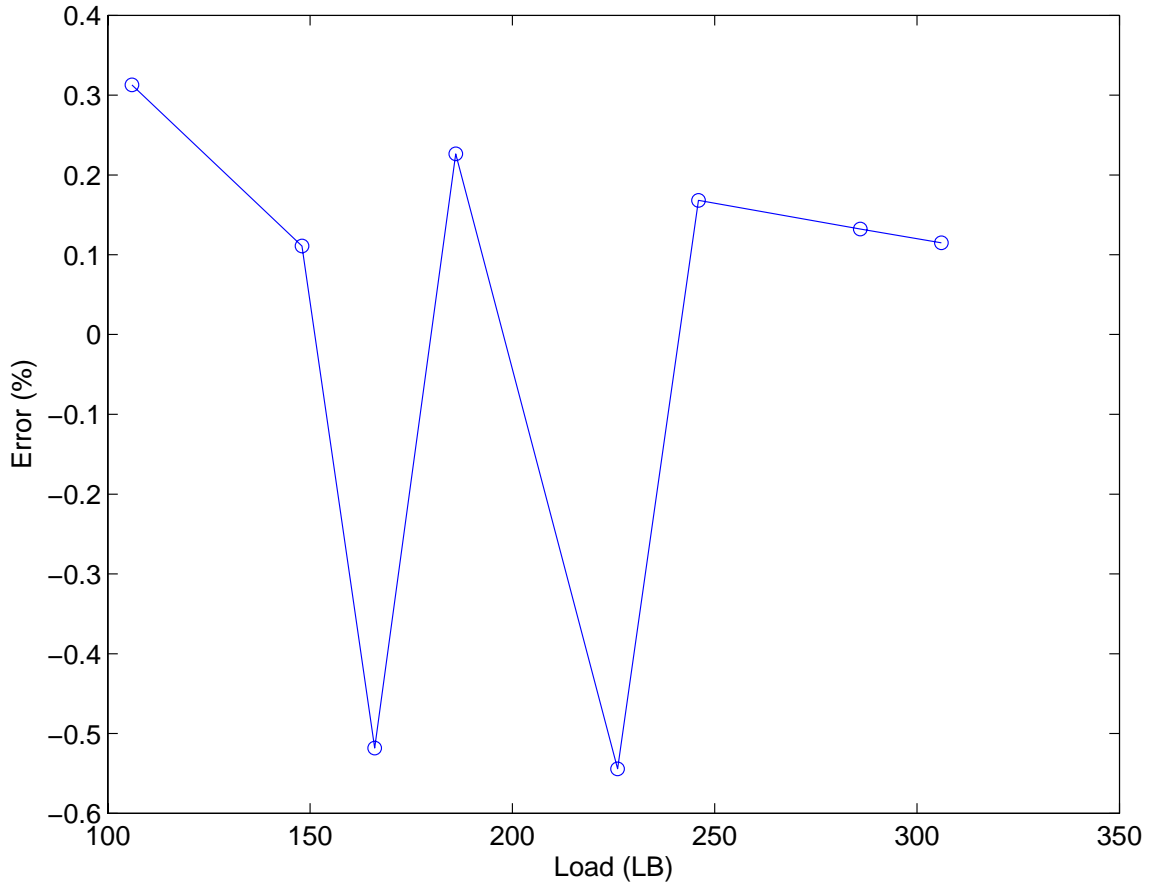


Figure 8-5: Linearity of Sensor's Output at Position 1.

To compare the data from these 11 test points, the same processing method is used, and the results are put together. The linear fitting curves are plotted in [Figure 8-6](#), and the linearity at all 11 positions separately are shown together in [Figure 8-7](#). The results show that the linearity for these 11 positions is within $\pm 3\%$. If we use the averaged linear fitting curve to test the sensor's uniformity, we are going to have the average curve shown in [Figure 8-6](#), and all of the 11 fitting curves fall into the range within $\pm 4\%$. Therefore, the uniformity of the output of sensor is within $\pm 4\%$.

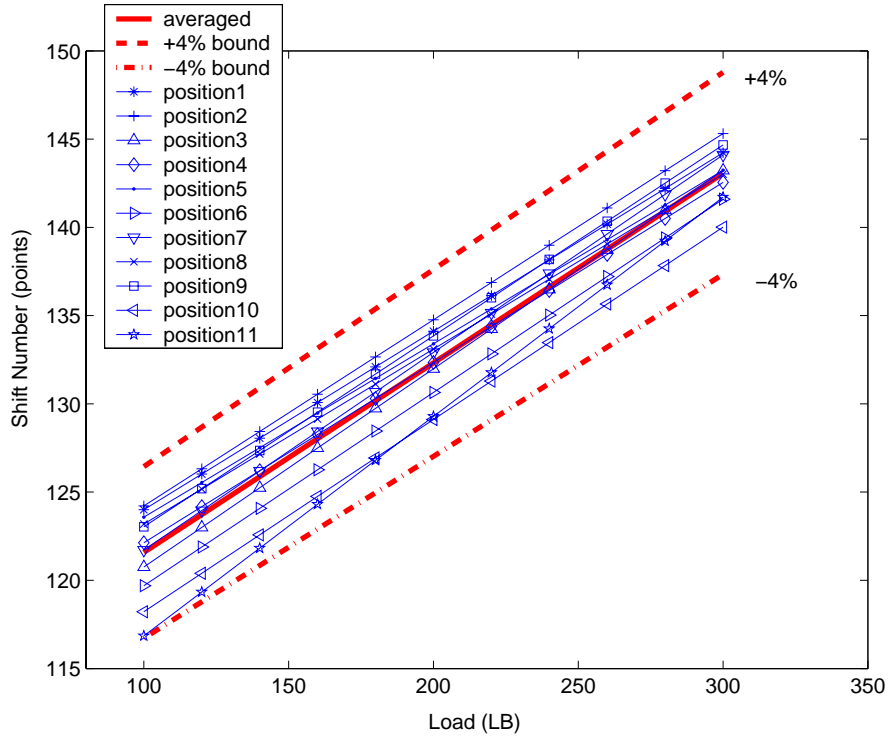


Figure 8-6: Linear Fitting Curves of Sensor's Output for All 11 Positions and the Average of All Curves.

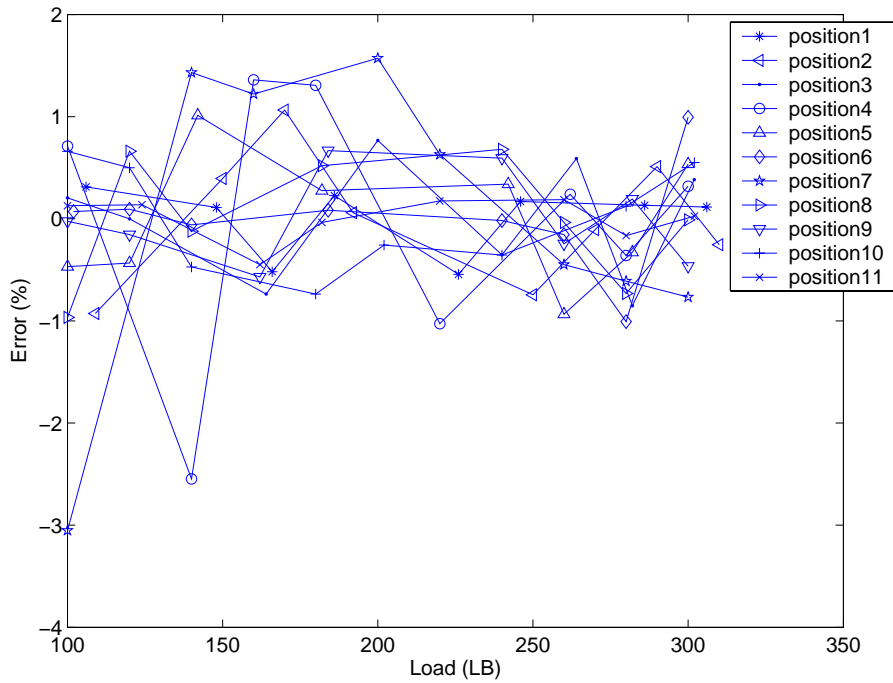


Figure 8-7: Linearity of Sensor's Output at 11 Positions Separately.

8.3 Measurement Error

From the results of uniformity and linearity tests for the sensor's output, we can see that the microwave sensor's output has good linearity and uniformity. We can now use the fitting curves achieved above to make a measurement and find the measurement error from the existing load data. As shown in Figure 8-8, the measurement has a better performance for heavier loads than light ones. The measurement error is almost within $\pm 5\%$ after 200 lb. Measurement position 4 and position 7 have larger errors for loads less than 200 lb. If positions 4 and 7 are ignored, the errors will be within $\pm 10\%$, as shown in Figure 8-9.

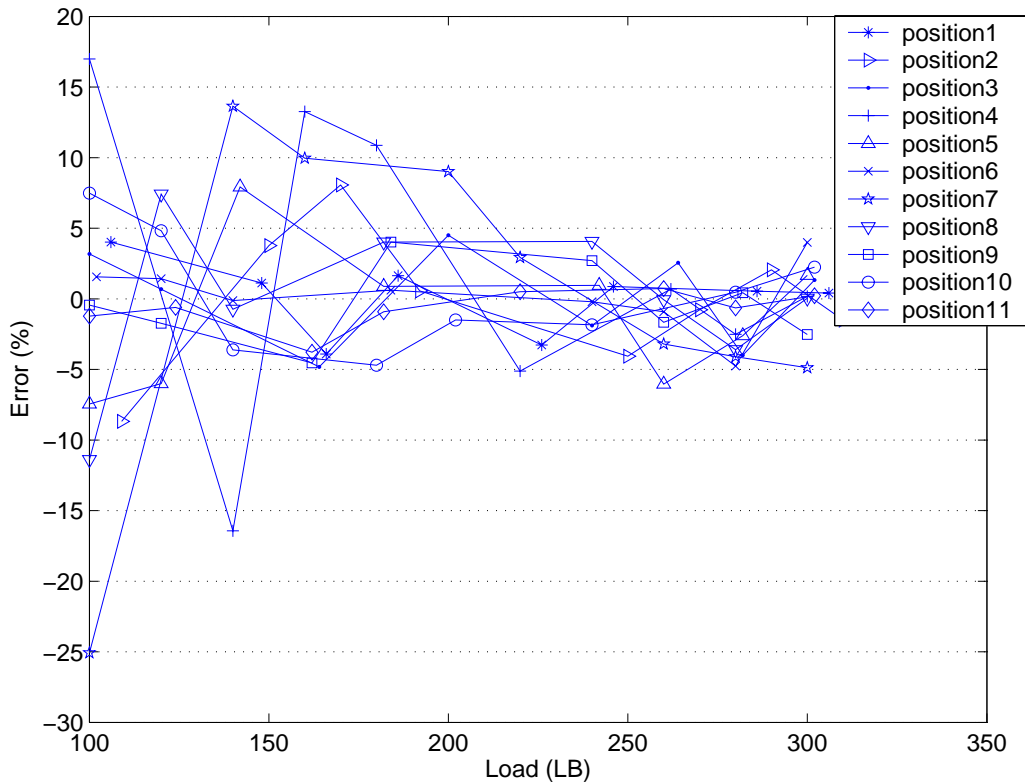


Figure 8-8: Measurement Errors.

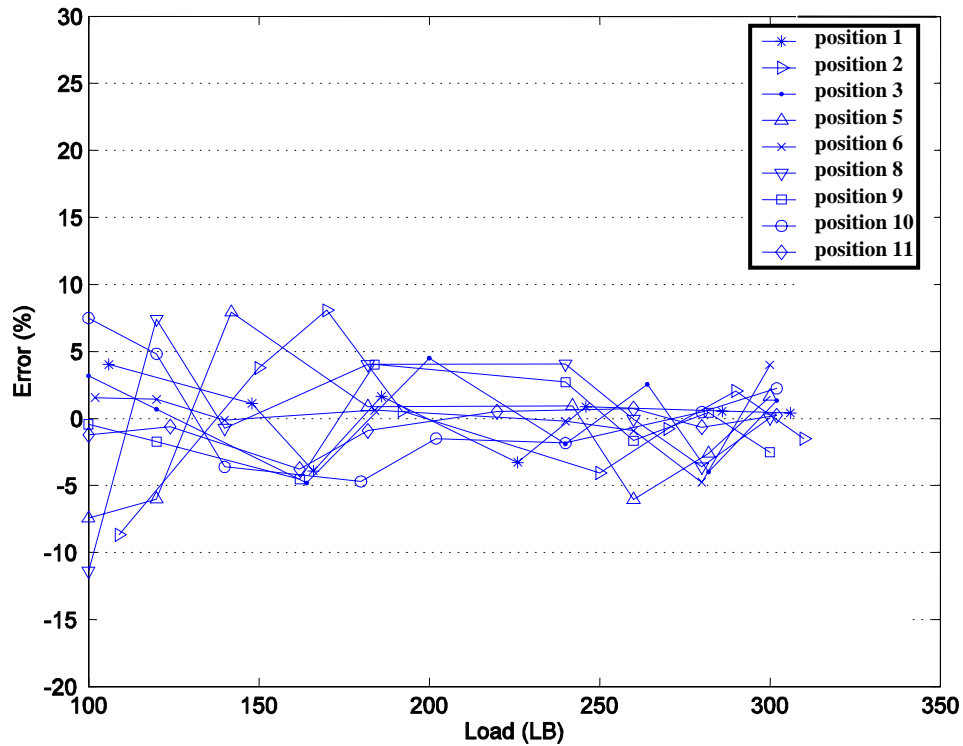


Figure 8-9: Measurement Errors Excluding Positions 4 and 7.

Since the load is not guaranteed to be applied exactly along the y-axis, errors are inevitable. The sampling frequency (5 MHz) is not high enough to make a good detection of the resonant frequency shift, which also introduces errors to the measurement results. From previous analysis, the higher the resonant frequency becomes, the more accurate the measurement. However, due to the limitation of the available components and price, the circuit operating at a higher frequency is hard to build and very expensive.

To demonstrate a more accurate measurement, another sensor head was designed and tested by using the network analyzer. This 6-ft. long sensor head has a diameter as small as 1 inch, and both ends of sensor are sealed with a soldered copper plate. A load was applied ranging from 130–300 lbs. at one test point, and the resonant frequency was measured to be about 7.5112 GHz. The shift of the resonant frequency according to the load is plotted in [Figure 8-10](#). It is obvious that it has good linearity. Furthermore, the measurement error is shown in [Figure 8-11](#), where the error is within 2.5%.

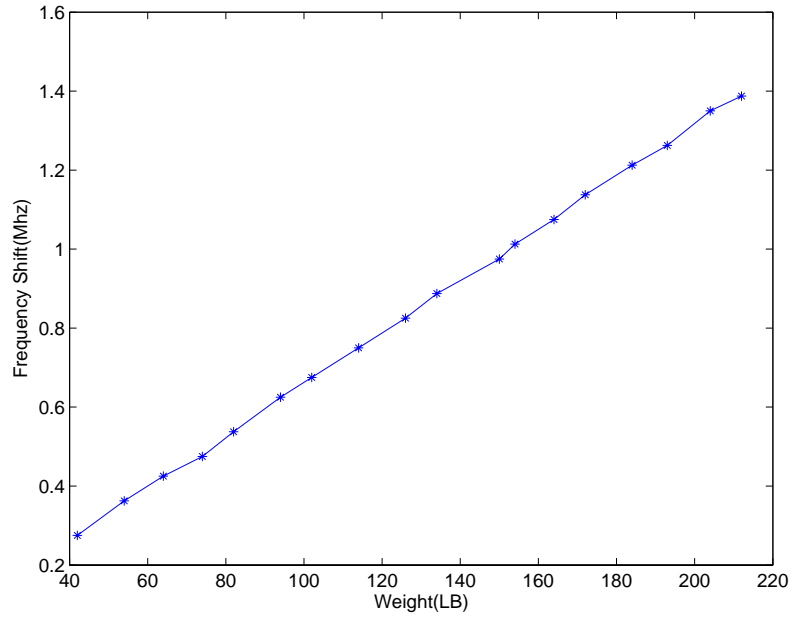


Figure 8-10: Resonant Frequency Shift Measured by Network Analyzer.

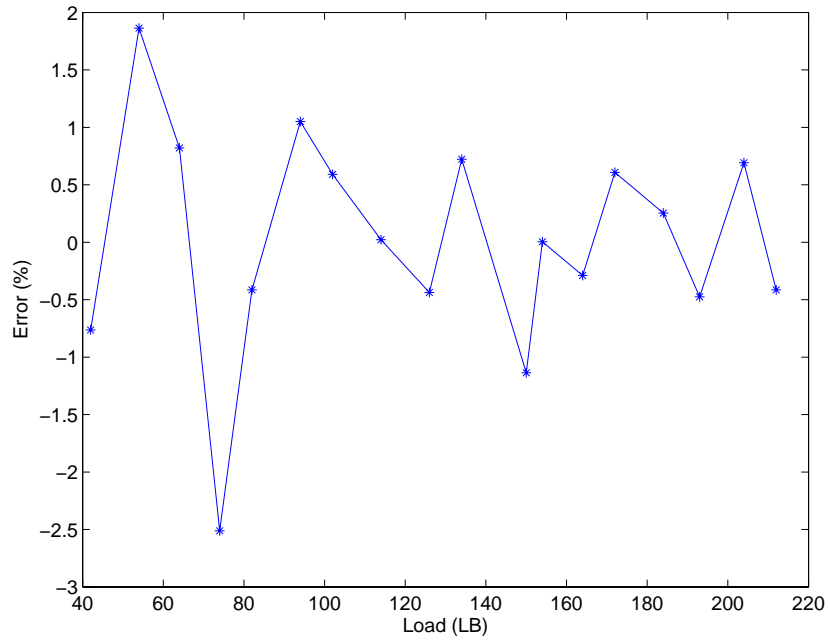


Figure 8-11: Measurement Error Based on Test Data.

CHAPTER 9: CONCLUSION

Although the WIM systems have been studied for a long time due to their importance in the transportation system, no ultimate configuration has been found yet. Since the accurate WIM systems are too expensive and hard to install, the low-cost piezoelectric WIM sensors from Measurement Specialties, Inc. and Thermocoax, Inc. were studied to improve the measurement performance. There are two basic types of piezoelectric sensors: the non-encapsulated and the encapsulated varieties. In this project, both sensor types were chosen for study.

To evaluate WIM sensors, the WIM standard and accuracy definition were given. Then, a remote WIM system was designed and used for data collection and analysis. The system has the ability to enable remote communication between server host and client host by a phone line and to monitor the WIM measurement. The sensors under study are installed in a WIM zone within a DPS weigh station where the corresponding static weight can also be achieved along with the WIM measurement.

Two kinds of load determination algorithms for piezoelectric sensors were developed; one was the integration algorithm, and the other was the pavement deflection algorithm. In the integration algorithm, the signal of the sensor's response to the vehicle's axle load right above the sensor is the positive pulse, which is used for load determination. The derivative method is used to detect the range of integration. In the pavement deflection algorithm, pavement vibration introduced by vehicle dynamics is analyzed and proved to be consistent with the results of some previous research. In the pavement deflection algorithm, signal is extracted after removing the pavement vibration signal from the original signals by the curve fitting method. Then, the signal of the sensor's response to pavement deflection, the dropdown signal before the positive pulse, is used for load determination. According to the measurement results, the sensor from ECM shows the best performance with accuracy of about 12–14% under the 95% confidence requirements by the integration algorithm. It shows good accuracy when using the pavement deflection algorithm. The results demonstrate that the pavement deflection algorithm can be used for WIM application. The results can be useful for new WIM sensor design based on the pavement deflection.

The FBG sensor is a very good candidate for the WIM system. Compared to piezoelectric sensors, FBG sensors offer a simpler and more explicit load determination algorithm, and the life span of the sensor is longer. However, it is necessary to build a sensor holder for a FBG sensor.

For the FBG WIM system evaluated in this study, the vehicle has to contact the same position of the sensor area to obtain accurate results. This is a limitation in the current FBG sensor holder used in this study. Meanwhile, the bandwidth of the laser source used in the developed detector is not wide enough, which limits the measurement range.

Considering the limitations of piezoelectric sensors, a microwave WIM sensor was designed and tested in this project. The innovative sensor is based on the perturbation theory of microwave resonant cavity. To drive the sensor, a fast frequency sweeping circuit was designed. In this circuitry, one DDS with a 2-GHz reference input clock was used to implement the fast frequency sweeping. One voltage controlled oscillator (VCO) and phase lock loop (PLL) were used to offer an output fed to the sensor head. With the designed circuit and sensor head, a lab test was conducted by using a loading machine. The linearity, uniformity, and measurement accuracy were tested. The sensor was found to have a satisfactory linearity and uniformity. With a heavy load applied on the sensor, the measurement error was within 10%. Further study can be done to design a higher-frequency circuit to improve the measurement accuracy, and the microwave device should be evaluated further under highway traffic loads.

REFERENCES

- [1] American Society for Testing and Materials, "Standard specification for highway Weigh-in-Motion (WIM) systems with user requirements and test method," ASTM Committee E-17 on Vehicle-Pavement Systems, ASTM Designation E 1318-02, 2002.

- [2] Benekohal, Rahim F., El-Zohairy, Yoassry M., and Wang, Stanley, "Truck travel time around weigh stations: Effects of weigh in motion and automatic vehicle identification systems," Transportation Research Record 1716, pp.135-143, 2000.

- [3] COST323, "European WIM Specification," Aug. 1999.

- [4] Strathman, James G., "The Oregon DOT slow-speed Weigh-in-Motion (SWIM) project: Final Report," State Research #152, Portland State University, Dec. 1998.

- [5] "States' Successful Practices Weigh-in-Motion Handbook," U.S. Department of Transportation Federal Highway Administration, Dec. 1997.

- [6] Scheuter, F., "Evaluation of factors affecting WIM system accuracy," presented in the second COST 323 WIM conference, Lisbon, Sept. 1998.

- [7] Bushman, Rob and Pratt, Andrew J., "Weigh in Motion technology - economics and performance," NATMEC '98 Charlotte, North Carolina, 1998.

- [8] Slavik, M. M. and Visser, A. T., "Development of weigh-in-motion network in South Africa," Transp. Res. Rec. 1272, Transportation Research Board, Washington DC., 1990.

- [9] Mamlouk, Michael S., "General outlook of pavement and vehicle dynamics," Journal of Transportation Engineering, Vol. 123, No. 6, pp. 515-517, Nov./Dec. 1997.

- [10] Ghosh, M. K. and Dinavahi, R, “Vibration analysis of a vehicle system supported on a damper-controlled variable-spring-stiffness suspension,” Proc. IMechE. vol. 219 part D: J. Automobile Engineering, pp. 607-619, 2005.
- [11] “States’ Successful Practices Weigh-in-Motion Handbook,” U.S. Department of Transportation Federal Highway Administration, Dec.1997.
- [12] Deakin, T., “WIM Systems for high speed overloaded vehicle pre-selection and low speed enforcement weighing,” the 1st European Conference on Weigh-in-Motion of Road Vehicles, Switzerland, 1995.
- [13] Martin, Peter T., Feng, Yuqi and Wang, Xiaodong, “Detector Technology Evaluation”, MPC-03-154, the Mountain-Plains Consortium (MPC), Nov. 2003.
- [14] Kistler Instruments Corporation, “Piezoelectric force transducers, design & use,” Amherst, NY, 2000.
- [15] Yannis, George and Antoniou, Constantinos, “Integration of Weigh-in-Motion technologies in road infrastructure management,” ITE Journal, Jan. 2005.
- [16] “Truck Weight Monitoring”, Federal Highway Administration, May 1, 2001, <http://www.fhwa.dot.gov/ohim/tmguid/tmg5.htm>.
- [17] Livingston, R. A., “FHWA Fiber-Optics Research Program: Critical Knowledge for Infrastructure Improvement”, <http://www.tfsrc.gov/pubrds/julaug99/fibrbrg.htm>.
- [18] Othonos, A., Kalli, K., “Fiber Bragg Gratings: Fundamentals and Applications in Telecommunications and Sensing”, Artech House, pp. 301, 1999.

- [19] Yu, J., Cullen College of Engineering, Dept. of Electrical and Computer Engineering, "An application of a fiber optic sensor in weigh-in-motion systems," University of Houston, p. xiv, 85 leaves, 2004.
- [20] "Ceramic piezoelectric sensor," Electronic Control Measurement Inc. (ECM).
- [21] "RoadTrax BL traffic sensors," Measurement Specialties Inc., Oct. 2001.
- [23] Brown, R. H., "Principles of Weigh-in-Motion using piezoelectric axle sensors," Measurement Specialties, Inc., Feb. 2001.
- [24] Christian Helg, "Kistler signal processing requirements for WIM LINEAS Type 9195," Kistler Instrument Corp., Amherst, NY, USA.
- [25] "Assessment, calibration and performance evaluations of LTPP SPS Weigh-in-Motion (WIM) Sites," MACTEC Proposal N., PROP03PCSL.211, volume I, pp. 20, May 2003.
- [26] Cosentino, Paul J., Wulf von Eckroth and Grossman, Barry G., "Analysis of fiber optic traffic sensors in flexible pavements," Journal of Transportation Engineering, Sept./Oct. 2003.

